UC Berkeley
UC Berkeley Electronic Theses and Dissertations

Title

A study on the development and application of optically polarized materials: Spin hyperpolarization from the nitrogen vacancy center in diamond and hyperpolarized 129Xe NMR biosensors

Permalink

https://escholarship.org/uc/item/3j2540w1

Author

Jeong, Keunhong

Publication Date

2016

Peer reviewed|Thesis/dissertation

eScholarship.org Powered by the California Digital Library
University of California

A study on the development and application of optically polarized materials: Spin hyperpolarization from the nitrogen vacancy center in diamond and hyperpolarized ^{129}Xe NMR biosensors

by

Keunhong Jeong

A dissertation submitted in partial satisfaction of the

requirements for the degree of

Doctor of Philosophy

in

Chemistry

in the

Graduate Division

of the

University of California, Berkeley

Committee in charge:

Professor Alexander Pines, Chair
Professor David E. Wemmer
Professor Michael Lustig

Fall 2016

Abstract

A study on the development and application of optically polarized materials:
Spin hyperpolarization from the nitrogen vacancy center in diamond
and hyperpolarized ^{129}Xe NMR biosensors

by

Keunhong Jeong

Doctor of Philosophy in Chemistry

University of California, Berkeley

Professor Alexander Pines, Chair

Optically hyperpolarized electrons can be harnessed to transfer polarization to interacting nuclei. One example of this is the optically hyperpolarized spin state of nitrogen vacancy centers (NV^- center) in diamond, which can act as sources of polarization for neighboring ^{13}C nuclei. Spin-exchange optical pumping (SEOP) using circularly polarized light has been used for ^{129}Xe hyperpolarization. Both hyperpolarization techniques provide a means of overcoming the fundamentally low sensitivity that has been a long-existing problem of NMR/MRI. Here, physical properties on polarization transfer from optically hyperpolarized NV^- centers to ^{13}C nuclei in diamond are studied as well as the development of several hyperpolarized ^{129}Xe NMR/MRI biosensors.

On the subject of NV^- centers in diamond, I studied polarization transfer to nearby ^{13}C in natural abundance ^{13}C diamond. The bulk ^{13}C spin polarization was estimated to be ~6 % at room temperature. Dynamic nuclear polarization and its mechanism were investigated for various diamonds with different ^{13}C concentrations (10, 25, 100%). The diamond with 10% ^{13}C enrichment showed similar polarization enhancement as the natural abundance sample and spin diffusion was considered to be the limiting factor in the polarization transfer mechanism. Optically detected magnetic resonance (ODMR) studies were also carried out on NV^- centers in nanodiamond powders. Interestingly, we observed not only broad powder patterns stemming from $\Delta m = 1$ transitions, but also sharp powder patterns from orientation independent overtone transitions ($\Delta m = 2$) that were supported by simulation.

On the subject of hyperpolarized ^{129}Xe biosensors, I synthesized a multi-metal ion sensor using hyperpolarized ^{129}Xe NMR, whose chemical shifts in a cryptophane cage gave distinct signals with regard to different metal ions. Also the metal ion concentration dependent signal intensity was found to have potential for quantification applications. A ^{129}Xe NMR/MRI biosensor targeting a folate receptor was developed and its binding on the Hela cell, which overexpresses folate receptors, was investigated by confocal laser scanning microscopy, flow cytometry, and ^{129}Xe hyper-CEST NMR/MRI technique. Furthermore, an estradiol-based biosensor was developed for ^{129}Xe Hyper-CEST detection of the estrogen receptor in breast cancer and a new methodology to detect endocrine distruptors in environmental samples by using ^{129}Xe hyper-CEST NMR was proposed. Lastly, I successfully synthesized a targeted, selective, and highly sensitive ^{129}Xe NMR nanoscale biosensor using a spherical MS2 viral capsid, cryptophane cage, and DNA aptamer.

For my family especially, Hyejin Chi and Jihyun Jeong

Table of Contents

Preface vi

Chapter 1

Room-Temperature in situ Nuclear Spin Hyperpolarization from Optically-Pumped Nitrogen Vacancy Centres in Diamond 1

1.1 Abstract 1

1.2 Introduction 1

1.3 Results 2

1.4 Discussion 6

1.5 Methods 7

1.6 Acknowledgements 8

1.7 Supporting information 8

Chapter 2

Nuclear spin hyperpolarization from nitrogen vacancy centers in ^{13}C enriched diamonds 13

2.1 Abstract 13

2.2 Introduction 13

2.3 Methods 14

2.4 Results and discussion 14

2.5 Conclusion 18

2.6 Supporting Information 18

Chapter 3

Two-dimensional optically-detected magnetic resonance of nitrogen vacancy centers in nanocrystalline diamond powder 22

3.1 Abstract 22

3.2 Introduction 22

3.3 Experiments and results 23

3.4 Discussion 27

3.5 Conclusion 29

3.6 Methods 29
3.7 Supporting information 30

Chapter 4

Investigation of DOTA-Metal Chelation Effects on ^{129}Xe Chemical Shift 35
4.1 Abstract 35
4.2 Introduction 35
4.3 Methods 37
4.4 Results and discussion 39
4.5 Conclusion 43
4.6 Acknowledgements 43
4.7 Supporting Information 43

Chapter 5

^{129}Xe-CEST NMR/MRI Biosensor Targeting Folate Receptor 47
5.1 Abstract 47
5.2 Introduction 47
5.3 Methods and Experiments 48
5.4 Results and discussion 51
5.5 Conclusion 53
5.6 Supporting information 54

Chapter 6

Hyperpolarized ^{129}Xe NMR Biosensor Targeting the Estrogen Receptor 59
6.1 Abstract 59
6.2 Introduction 59
6.3 Experiemtal section 60
6.4 Conclusion 64
6.5 Supporting information 65

Chapter 7

Targeted Molecular Imaging of Cancer Cells using MS2-Based ^{129}Xe NMR 70

7.1 Abstract 70

7.2 Introduction 70

7.3 Results and discussion 71

7.4 Conclusion 75

7.5 Materials and methods 76

7.6 Supporting information 77

Biblography 82

Acknowledgement

I would like to thank all my collaborators of the projects. I thank my admirable PI, Alexander Pines who gave me a huge inspiration on the science. I thank Prof. David E. Wemmer. He is a great advisor for all Xenon projects. I will not forget his kindness. I thank Prof. Matthew B. Francis. By courtesy of him, I did all synthesis in his lab.

I thank Dr. Jonathan King. He has been working with me on diamond project. His advice was invaluable. I should thank all other Pines lab memebers (Pinenuts) for being kind to me. It is my great honor to a Pinenut and I will live up to its reputation. Also, I should thank all Wemmer lab and Francis lab members who were very kind and helped me a lot.

I was very lucky to know all those three lab people thanks to Chemical Biology Graduate Program in Berkeley. In the beginning, rotation was a hard time for me to adapt to each new lab circumstance, however, those experiences gave me much insight on science.

I also thank Republic of Korea Army and Korea Military Academy for supporting me. I will return the favor by dedicating my lifetime to education and research for Republic of Korea.

Lastly, I could take a firm stand thinking of my dad and my brother who are in heaven together. Thank you.

Preface

Nuclear magnetic resonance (NMR) and Magnetic resonance imaging (MRI) have been an essential technology in many scientific fields. Despite its usefulness, its low signal to noise, explained well by the Boltzmann distribution, has been the biggest limitation to technological development. Therefore, to overcome these limitations, low temperatures (4–70 K, when possible) and high magnetic field (7-21 T) are normally used. Many methods which drive polarizaition beyond its allowed Boltzmann distribution have been widely studied: spin exchange optical pumping of noble gases, parahydrogen induced polarization, optical pumping in semiconductors, chemically induced dynamic polarization, photo-excited triplet states of organic solids. Most polarization transfer pathways in use exploit electron polarization as a source for neighboring nuclei, methods that are known as dynamic nuclear polarization (DNP). Recently refined high field DNP has been optimized at cryogenic temperatures to polarize the electron spin and transfer to the nuclei, but it has a problem of losing its polarization during thawing the sample to room temperature. Therefore, room temperature DNP would be a huge breakthrough in technology development of magnetic resonance techniques. One promising method for nuclear hyperpolarization is using nitrogen vacancy centers (NV^- center) which can have up to ~90 % electron spin polarization at room temperature. I have been employing DNP methodology using the optically polarized NV^- center to obtain strong NMR signal enhancements. In chapter 1, the highest *in situ* ^{13}C hyperpolarization obtained (~6 %) for diamond in 420 mT at room temperature is introduced. High polarization transfer from the optically polarized NV^- center to bulk nuclei in diamond showed the possibility of using this platform with interacting spins on the high surface area outside of the diamond as a hyperpolarization transfer source at room temperature. The concept of driving polarization transfer to the outside of the diamond will be made possible by spin interactions like spin diffusion or cross relaxation between hyperpolarized nuclei in the diamond and outside solid/liquid nuclei. Therefore, I studied hyperpolarization with ^{13}C enriched diamonds (10 %, 25 %, 100 % ^{13}C enriched samples) which may increase polarization transfer efficiency at the surface. Understanding the polarization mechanism in detail is essential for the further research (Chapter 2). In order to provide more surface area of hyperpolarized diamond, it is advantageous to use nanocrystalline diamond. This leads to an orientation problem, however, due to the dependence of the NV^- spin states on the orientation of the NV^- axis relative to the magnetic field. This results in a broad range of transitions that form powder patterns familiar in solid state NMR. However, I found a sharp overtone ODMR transition whose properties are insensitive to orientation (Chapter 3). This series of studies may open a new way to do room temperature DNP, which can polarize any spin active material beyond thermal polarization by using laser and microwave radiation, and NV^- centers in nanodiamond.

Magnetic Resonance Imaging (MRI) is an excellent medical imaging modality, which is minimally perturbing. This well-established technique generally detects protons from water and fat in the body. Even with the modest polarization, the high abundance of water and fat allow sensitive anatomical imaging. However for imaging dilute molecules of interest both sensitivity due to low polarization, and dynamic range problems limit detection to the most abundant metabolites. To overcome this problem various techniques have been developed to enhance signal intensity and sensitivity, and these have been combined with molecular sensors to generate contrast with high specificity. DNP and hyperpolarization by SEOP have been highlighted as methods to increase sensitivity significantly. ^{129}Xe is an ideal reporter for NMR because it is inert and hyperpolarizable, biocompatible, and has no natural background signal in living systems. The use of hyperpolarized ^{129}Xe as an imaging agent has been demonstrated in the MRI imaging of lung tissue, brain, and kidney. For molecular imaging, Cryptophane A (CryA) based xenon sensors have been developed with chemical exchange saturation transfer (CEST) to increase the detection sensitivity by 1,000 fold relative to direct observation of the caged xenon. Molecular sensors carrying large numbers of CryA coupled to targeting elements provide a further increase in sensitivity, and have been applied to detection of cancer cells. Hyper-CEST NMR imaging with these high density CryA sensors may thus provide a powerful tool for detection of molecular targets especially those on cancer cells for which early stage detection is highly critical for survival of patients. Based on these concepts, in chapter 5, overexpressed folate receptor was targeted for hyper-CEST ^{129}Xe NMR imaging with a newly designed CryA biosensor. Furthermore, estrogen receptor could be a target biomarker for early detection of breast cancers. A biosensor targeting estrogen receptor was studied in chapter 6 along with endocrine disruptor detection using hyper-CEST ^{129}Xe NMR. In chapter 7, a highly sensitive ^{129}Xe NMR nanoscale biosensor using a spherical MS2 viral capsid was introduced and its high binding specificity toward targeted lymphoma cells was shown. Those studies provide strong basis for the continuing development of targeted cancer cell imaging agents for xenon NMR/MRI. In addition, in chapter 4, we demonstrate a technique for multi-metal ion sensing of transition metals using hyperpolarized ^{129}Xe associated with a cryptophane cage modified with DOTA. This sensor may be used to detect metal ions important for different cell functions and to determine the amounts present. Also, resolved metal ion peaks from mixtures provide great potential as a hyperpolarized ^{129}Xe NMR/MRI tag for *in vivo* detection. If this metal ion sensor is attached to interesting biological molecules, its position and movement could be visualized by ^{129}Xe NMR/MRI. The target's concentration could be estimated, and two or more biomolecules could be detected simultaneously.

Chapter 1

Room-Temperature in situ Nuclear Spin Hyperpolarization from Optically-Pumped Nitrogen Vacancy Centres in Diamond

(This is reprint from Nature Communications, 2015, 6, 8965: "Room temperature *in situ* nuclear spin hyperpolarization from optically pumped nitrogen vacancy centers in diamond.", Jonathan P. King, **Keunhong Jeong**, Christophoros C. Vassiliou, Chang S. Shin, Ralph H. Page, Claudia E. Avalos, Hai-Jing Wang & Alexander Pines. My main contribution to this work is constructing the experimental apparatus, collecting the DNP data and optical characterization of the samples.)

1.1 Abstract

Low detection sensitivity stemming from the weak polarization of nuclear spins is a primary limitation of magnetic resonance spectroscopy and imaging. Methods have been developed to enhance nuclear spin polarization but they typically require high magnetic fields, cryogenic temperatures or sample transfer between magnets. Here we report bulk, room-temperature hyperpolarization of ^{13}C nuclear spins observed via high-field magnetic resonance. The technique harnesses the high optically induced spin polarization of diamond nitrogen vacancy centres at room temperature in combination with dynamic nuclear polarization. We observe bulk nuclear spin polarization of 6%, an enhancement of ~170,000 over thermal equilibrium. The signal of the hyperpolarized spins was detected *in situ* with a standard nuclear magnetic resonance probe without the need for sample shuttling or precise crystal orientation. Hyperpolarization via optical pumping/dynamic nuclear polarization should function at arbitrary magnetic fields enabling orders of magnitude sensitivity enhancement for nuclear magnetic resonance of solids and liquids under ambient conditions.

1.2 Introduction

Nuclear magnetic resonance spectroscopy (NMR) and magnetic resonance imaging (MRI) are indispensable techniques in fields reaching from chemistry and materials to biology and medicine. Despite their non-destructive nature and broad range of applications they are subject to limited sensitivity. The sensitivity is primarily limited by the weak magnetization of nuclear spins, which is dependent on the population differences between nuclear spin states. At room temperature, the fractional excess of spin state population, or polarization, can be <1 p.p.m., motivating the development of methods to enhance NMR signals by generating polarization greater than prevails in thermal equilibrium. Such methods include: optical pumping applied to noble gases (1–4) and semiconductors (5, 6); parahydrogen-induced polarization (7–9); low

temperature dynamic nuclear polarization (DNP) (10–13); chemically induced DNP (14); and optical pumping with DNP of excited triplet states in organic solids (15). Despite the success of each of these techniques, they are limited to either low temperatures or specific molecules. Particularly desirable would be a general method to produce hyperpolarization at similar magnetic fields and temperatures as the NMR or MRI experiment. This enhancement would enable, for example, the observation of small quantities of biomolecules under biologically relevant conditions. Recently, it has been recognized that nuclear spin hyperpolarization generated from nitrogen vacancy (NV) centres in diamond could provide a platform for polarization transfer to NMR/MRI samples (16–19). NV^- centres, with their optically polarized electron spin states and optical spin readout, have been the subject-of-interest for applications in quantum information, photonics and high-resolution sensing (20), but here we are interested in their application to the polarization of nuclear spins. Nuclear spins hosted within the diamond lattice have been hyperpolarized using level anti-crossings that occur at specific crystal orientations and magnetic field strengths (17, 18). Evidence of nuclear spin hyperpolarization of proximate ^{13}C spins was deduced from optically detected magnetic resonance (ODMR) spectra at the level anti-crossing fields and subsequently confirmed at a value of $\sim$ 0.5% in bulk by shuttling the diamond sample to a higher magnetic field for NMR detection (19). These techniques were then extended to low fields away from the anti-crossing and to arbitrarily oriented NV^- centres using microwave irradiation (21). Bulk ^{13}C polarization has been generated at high field and low temperature and attributed to the coupling of the nuclear spins to the dipolar energy reservoir of the NV^- ensemble (16), but the precise mechanism remains unclear. Furthermore, a recent proposal has suggested the use of shallow NV^- centres as a source for direct polarization transfer to a surrounding liquid (22). In contrast, our method uses optical pumping of diamonds coupled with DNP under ambient conditions to obviate the need for cryogenic temperatures, sample shuttling, and precise crystal orientation and magnetic field strengths. Here we show the generation of ^{13}C nuclear spin polarization in diamond using microwave-driven DNP from the optically polarized electrons of NV^- defects. We demonstrate bulk nuclear spin polarization of 6%, an enhancement of $\sim$170,000 over thermal equilibrium. This is an order of magnitude greater than previous methods using NV^- centres (19,21) and is achieved without precise control over magnetic field and crystal alignment. Room-temperature, hyperpolarized diamonds open the possibility of polarization transfer to arbitrary samples from an inert, non-toxic and easily separated source, a long sought-after goal of contemporary magnetic resonance.

1.3 Results

Optically pumped DNP. The NV^- centre in diamond comprises a substitutional nitrogen atom adjacent to a vacancy. Each NV^- centre has C_{3v} symmetry with the C_3 axis aligned along one of the four equivalent [111] crystal axes. The electronic ground state of the negatively charged NV^- centre is a spin-1 triplet with a zerofield splitting D = 2.87 GHz between the $m_s = \pm 1$ and $m_s = 0$ states (Fig. 1). The $m_s = 0$ state is preferentially populated via optical pumping with a 532nm laser and spin-dependent nonradiative decay rates. Applying a magnetic field along the defect symmetry axis lifts the degeneracy of the $m_s = \pm 1$ states and gives rise to two distinct magnetic

resonance transitions observable by ODMR. ODMR relies on a reduction in the fluorescence intensity induced by depopulation of the $m_s = 0$ state (Fig. 1a). In our experiment, ^{13}C spins in a 4.5 mg diamond are hyperpolarized by DNP using an optically polarized microwave transition (red and blue arrows in Fig. 1b, spectra shown in Fig. 1c, d). DNP in diamond is known to occur via a combination of thermal mixing, where the dipolar energy reservoir of the interacting paramagnetic centres couples to the nuclei, and solid effect, where electron/nuclear spin flips are driven by microwave irradiation (23) (See Supplementary Note 1 for a discussion of DNP mechanisms). The result of each of these mechanisms is the transfer of electron spin polarization to the nuclei. Owing to the optically polarized NV^- centres used for DNP, a strong, hyperpolarized NMR signal was observed from this natural isotopic abundance sample after accumulating 60 scans with a repetition time of 60 s (Fig. 2a).

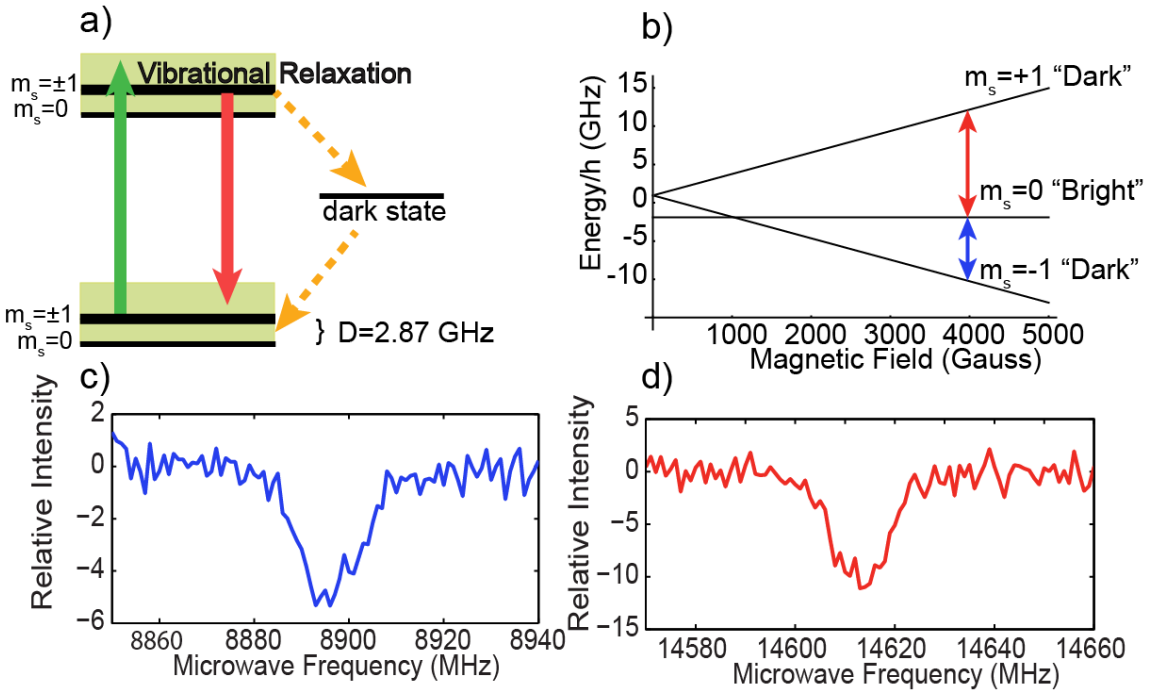

Figure 1. Optical pumping and optically detected magnetic resonance of nitrogen vacancy centres. (a) Energy levels and transitions for an NV^- centre in diamond. Optical pumping with green light at 532nm induces transitions from the ground state spin-1 triplet to the excited triplet state. Subsequent to vibrational relaxation, fluorescence is detected in the red and near-IR. Spin conserving optical transitions and spin-dependent, non-radiative intersystem crossings lead to a preferential population of the $m_s = 0$ ground state, producing electron spin hyperpolarization of the NV^- centre. (b) Application of a magnetic field aligned along the NV^- axis lifts the degeneracy of the $m_s = \pm1$ states, giving rise to two transitions that can be driven with microwave irradiation. The two transitions, (c) between $m_s = 0$ and $m_s = -1$, and (d) between $m_s = 0$ and $m_s = +1$, are observed by optically detected magnetic resonance (ODMR) through a reduction in the fluorescence intensity caused by a depletion of the ground $m_s = 0$ state. h=Planck's constant.

These parameters were chosen to achieve sufficient signal-to-noise in a reasonable experimental time and result in a polarization slightly lower than the maximum steady-state value relevant to a single scan. For comparison and calibration, after accumulating 12,676 scans with a repetition time of 10 ms, a 10 ml sample of liquid dimethyl sulfoxide (DMSO), enriched to 99% ^{13}C and doped with Gd(III), produced an NMR signal of lower amplitude than the

diamond by a factor of ~12 (Fig. 2b). From the ratio of the numbers of ^{13}C nuclei in the diamond and DMSO samples (0.015), the number of scans needed for each and the ratio of signal amplitudes, the maximum bulk ^{13}C polarization in the diamond is estimated to be 6%. The odd function of polarization with respect to applied microwave frequency (Fig. 2c,d) is characteristic of DNP in solids, and the opposite signs of the signals in Fig. 2c,d are consistent with population of the $m_s = 0$ state of the NV^- centre. Since the width of the EPR transition is similar to the NMR frequency (~4.5 MHz), it is expected that both solid effect and thermal mixing DNP mechanisms may be present (23), and the frequency span between the maximum (occurring at 8,903 and 14,606 MHz) and minimum (8,894 and 14,615 MHz) polarizations is similar to, but not exactly, twice the NMR frequency. We attribute the dynamics to the coupled processes of DNP of nuclear spins proximate to the NV^- centres, nuclear spin diffusion to the bulk material (23, 24) and spin-lattice relaxation. This process is shown schematically in Fig. 3a and leads to a build-up of nuclear spin polarization over several minutes (Fig. 3b).

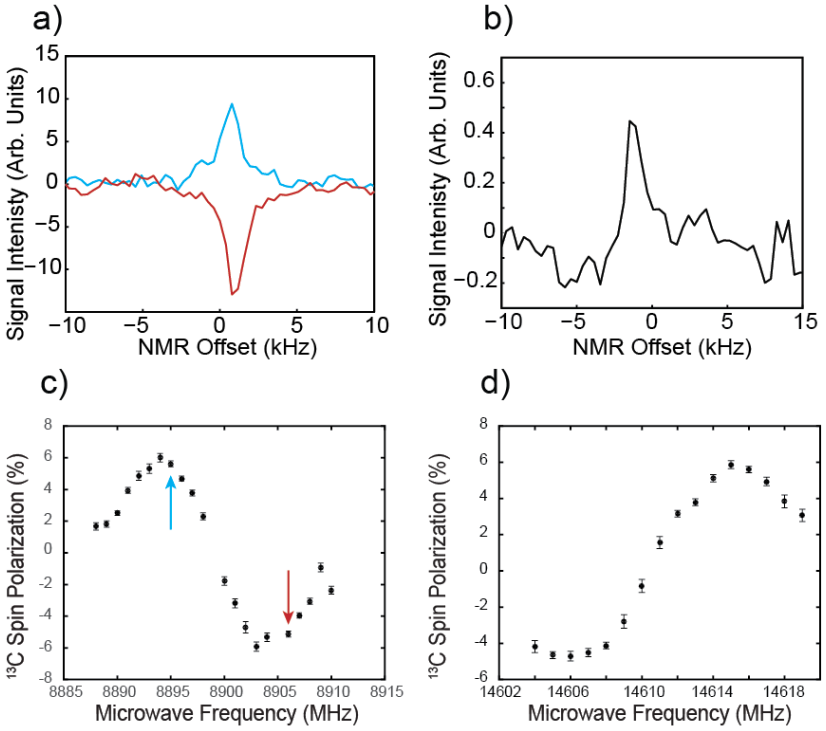

Figure 2. Hyperpolarization of nuclear spins. (a) ^{13}C NMR spectra of natural abundance diamond after the accumulation of 60 scans under DNP for 60 s at 8,895MHz (blue) and 8,907MHz (red). (b) NMR spectrum of thermal equilibrium reference sample (99% ^{13}C-enriched DMSO) after accumulating 12,676 scans. The diamond DNP signal corresponds to a polarization of 6%, an enhancement of ~170,000 over thermal equilibrium. Consistent with known mechanisms of dynamic nuclear polarization, ^{13}C nuclear polarization is an odd function of applied microwave frequency at the (c) $m_s = 0$ to $m_s = -1$ and (d) $m_s = 0$ to $m_s = +1$ NV^- transitions. The opposite signs of these two curves are consistent with the opposite electron spin polarizations of the two NV^- transitions. Data were acquired with a laser intensity of 16Wcm^{-2} and microwave power of 1.3W. Error represents 95% confidence intervals for the amplitude of a Lorentzian fit to the frequency-domain data.

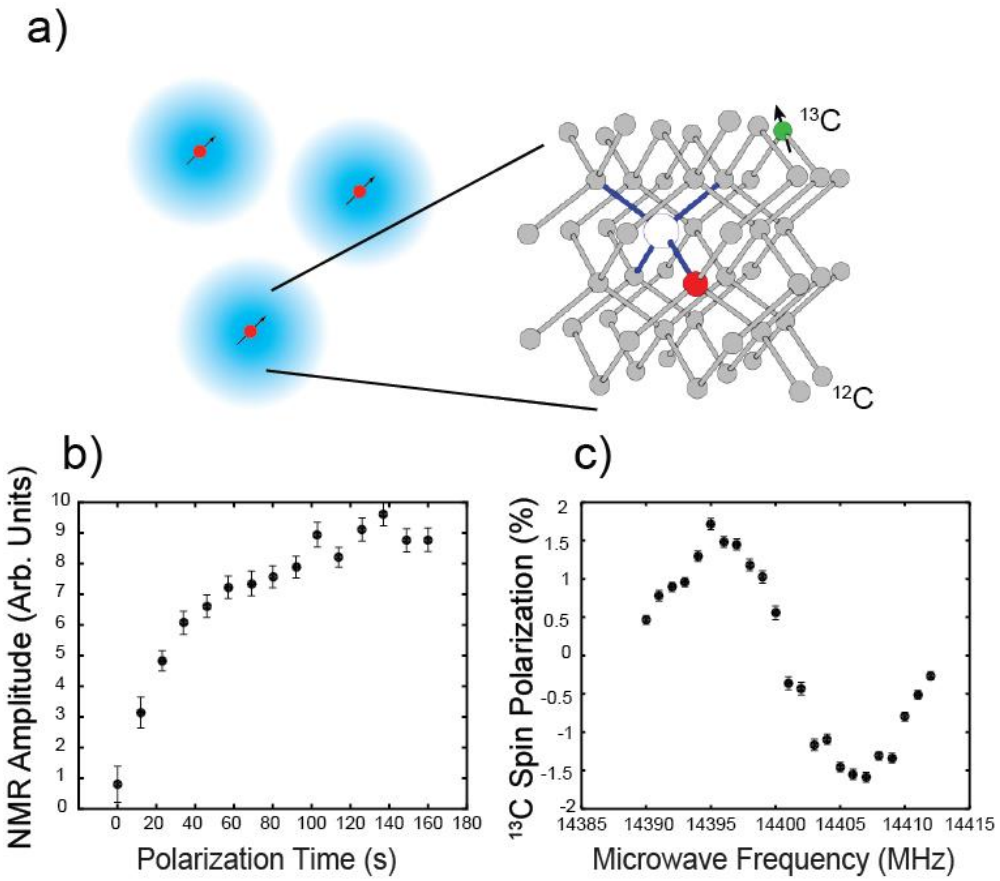

Figure 3. Dynamics and orientation dependence of hyperpolarization. (a) Schematic representation of the DNP process. Direct polarization near NV^- centres (red/white spheres in inset) gives rise to ^{13}C (green spheres in inset) spin hyperpolarization. Spin diffusion carries the polarization (blue regions) from the NV^- centres (red circles) to the bulk material until a steady state is reached. (b) Time dependence of ^{13}C spin polarization obtained by ^{13}C NMR at 4.5 MHz. Beyond ~100 s, the spin polarization has reached a steady state that represents a balance between the hyperpolarization/spin diffusion process and the spin-lattice relaxation of the nuclear spins. (c) Hyperpolarization achieved with NV^- centres misaligned 14° from the magnetic field. Error represents 95% confidence intervals for the amplitude of a Lorentzian fit to the frequency-domain data.

Orientation dependence. The OP/DNP process is expected to be effective at arbitrary orientations of the NV^- defects, since the process depends on matching of the microwave frequency to a given transition, rather than a precise field strength and orientation. To test this idea, the sample was rotated 90° around the axis perpendicular to the laser and magnetic field. This ensured that no NV^- centres were aligned with the magnetic field. An ODMR signal was found at 14,402 MHz, which corresponds to an NV^- misalignment of 14° from the field. DNP data were collected at this frequency (Fig. 3c) showing ^{13}C spin polarization approaching 2%. The reduction in DNP efficiency is attributed to the mixing of NV^- spin states and the corresponding reduction of polarization between the NV^- energy levels. However, high

polarization should be present for all orientations except near the magic angle ($\cos^{-1}\frac{1}{\sqrt{3}}$), where the states are an equal admixture of $m_s = \pm 1$ and $m_s = 0$. The effectiveness of the DNP for misaligned NV^- centres will be critical for the extension of this technique to randomly oriented powders, where polarization may be extracted from any crystal orientation via the integrated solid effect (15). We further note that our technique should be general for a large range of magnetic fields. As long as the NV^- Zeeman interaction is significantly greater than the zero-field splitting, the physics presented here should be valid, including the robustness to orientation. Near to and below the level anti-crossing, the quantization axis will no longer be solely defined by the external field and this mechanism will no longer be valid, although other polarization mechanisms may exist (21).

1.4 Discussion

These results introduce a methodology for nuclear spin hyperpolarization in diamond that is robust to magnetic field strength and orientation. They demonstrate a bulk polarization of 6%, but with optimization of magnetic field, orientation and diamond samples the polarization could in theory approach the NV^- spin polarization, which is of order unity (20). Hyperpolarized diamonds, which can be efficiently integrated into existing fabrication techniques to create high surface area diamond devices, including nanocrystal powders, will provide a general platform for polarization transfer. We envision highly enhanced NMR of liquids and solids using existing polarization transfer techniques, such as cross-polarization in solids (25) and cross-relaxation in liquids (26), or direct DNP to outside nuclei from shallow NV^- centres. Cross-relaxation has already been demonstrated as a method for polarization transfer between phases such as hyperpolarized ^{129}Xe gas to solid (27) and liquid (28). These transfer techniques should be applicable to any sample that can be brought into intimate contact with the diamond surface, with the efficiency of polarization transfer determined by the relative rates of polarization transfer and spin-lattice relaxation. The efficiency of polarization transfer would approach 100% for long-T_1 samples. Possible samples include liquids, solids and mildly frozen liquids (for example, glassy aqueous solutions) for solid-state OP/DNP with solid-state spin diffusion followed by thawing and observation of hyperpolarized liquid-state NMR. Hyperpolarization techniques based on optically polarized NV^- centres could enable enhanced sensitivity of magnetic resonance experiments, resulting in decreased experimental time and lower detection limits comparable to those of contemporary techniques such as dissolution DNP and chemical-specific, parahydrogen induced polarization. NV^- centres as a polarization source could, however, be used at room temperature or under mild (near 0 °C) freeze/thaw conditions, which obviates the need for cryogenic instrumentation, shuttling between two high magnetic fields, and exogenous polarizing agents. The technique should be applicable to arbitrary target molecules, including biological systems that must be maintained at near ambient conditions.

1.5 Methods

Optically pumped DNP apparatus. To investigate DNP effects with NV^- centres, we constructed a combined DNP/optically detected magnetic resonance / NMR instrument, shown schematically in Supplementary Fig. 1. The magnetic field is supplied by a custom-built electromagnet (Tel-Atomic) and is set to 420mT. A Coherent Verdi G15 laser delivers 532 nm illumination to the sample through a Gaussian beam with a waist of 1.5 mm, essentially illuminating the entire surface of the diamond with an intensity up to $16 W cm^{-2}$. The laser intensity was chosen to maximize polarization without excessive sample heating (see Supplementary Note 2 and Supplementary Fig. 2 for laser power dependence). Fluorescence is separated from excitation light by a dichroic mirror and detected by an avalanche photodiode. ODMR is performed by monitoring the diamond fluorescence while varying the applied microwave frequency. Microwave irradiation is delivered to the sample by a microwave loop of diameter 9.6 mm (See Supplementary Note 2 and Supplementary Fig. 3 for microwave power dependence). NMR was performed using a Magritek Kea 2 spectrometer with a homebuilt 50-turn planar coil probe tuned to ~4.5MHz.

Diamond sample preparation. A commercially-available 2mm x 2mm x 0.32 mm, <100> surface-orientation single crystal of synthetic high-pressure, high-temperature diamond (Sumitomo) was acquired. Electron irradiation at 1 MeV with a fluence of 10^{18} cm^{-2} followed by annealing at 800 °C for 4 h in a mixture of 9% H^2 and 91% He yielded an ensemble of NV^- centres. NV^- concentration is expected to be on the order of $10^{18} cm^{-3}$ under these conditions (29). The crystal was mounted on a goniometer inside the electromagnet, and one of the <111> axes was aligned with the magnetic field by monitoring the ODMR spectrum. In this orientation, there are three equivalent ODMR spectra of the NV^- centres along <111> axes at an angle of 109.5° with respect to the magnetic field and a single ODMR spectrum corresponding to the aligned NV^- centres. With the field set to 420 mT, ODMR and DNP were performed using microwave fields at 8,900 and 14,600 MHz. For the misaligned NV^- data, the sample holder/NMR probe was rotated 90° around the vertical axis, which is perpendicular to both the magnetic field and the laser. A separate reference measurement (described later) was performed for this configuration in case of unintended variations of the NMR sensitivity.

Experimental procedure. DNP data were acquired by polarizing for 60 s unless otherwise noted. Then, a $\pi/2$ NMR pulse of duration 10 ms (calibrated via a nutation experiment) generated transverse magnetization that was inductively detected. Time-domain NMR data were apodized by exponential multiplication with a decay constant of 1 ms. After application of phase correction and a fast Fourier transform algorithm, frequency-domain spectra were fitted to single Lorentzian functions. The nuclear polarization was taken to be proportional to the amplitude of the fitted peak; error bars represent the 95% confidence intervals for the amplitude. The bulk polarization was calibrated relative to the thermal equilibrium signal of a 99% ^{13}C-enriched sample of dimethyl sulfoxide, doped with gadolinium (III). The doping resulted in a spin-lattice relaxation time < 2ms, which allowed acquisition of ~10,000 scans necessary for sufficient signal-to-noise ratio. See Supplementary Note 3 and Supplementary Fig. 4 for a discussion of the validity of the calibration. The polarization build-up was monitored with a saturation-recovery pulse sequence, in which the polarization was initially destroyed

with a series of π/2 pulses followed by a variable polarization time and NMR detection. The build-up data were processed separately by exponential apodization and Fourier transform with Magritek Prospa software, followed by phase correction and fitting to Lorentzian functions to extract the amplitude.

1.6 Acknowledgements

This work was supported by the Director, Office of Science, Office of Basic Energy Sciences, Materials Sciences and Engineering Division, of the US Department of Energy under Contract No. DE-AC02-05CH11231. K.J. acknowledges fellowship support from the Republic of Korea Army. We thank Eric Scott and Melanie Drake for providing the diamond sample used in this study. We also thank Jeffrey Reimer, Birgit Hausmann and Carlos Meriles for helpful discussions.

1.7 Supporting information

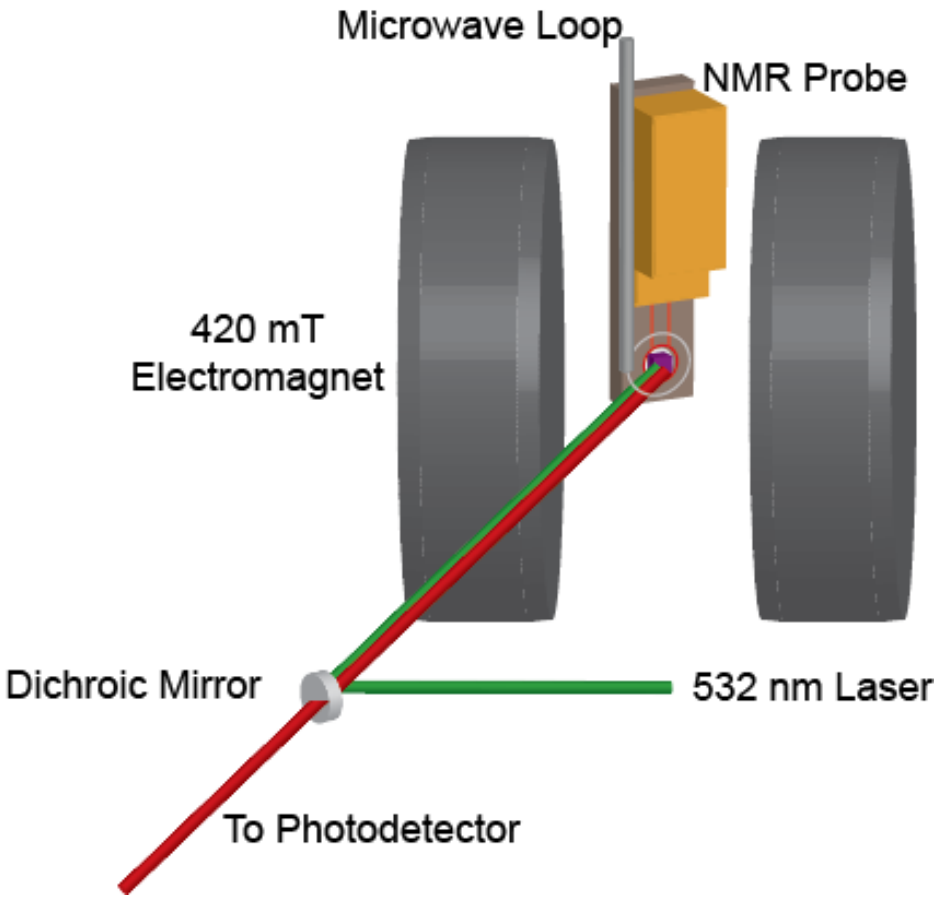

Supplementary Figure 1: Experimental Setup for Optically Detected Magnetic Resonance, Dynamic Nuclear Polarization, and Nuclear Magnetic Resonance: An unfocused 532 nm laser beam provides optical pumping and induces red/NIR sample fluorescence which is read out using a photodetector. A tuned NMR probe provides RF irradiation and detection while a microwave loop provides microwave irradiation.

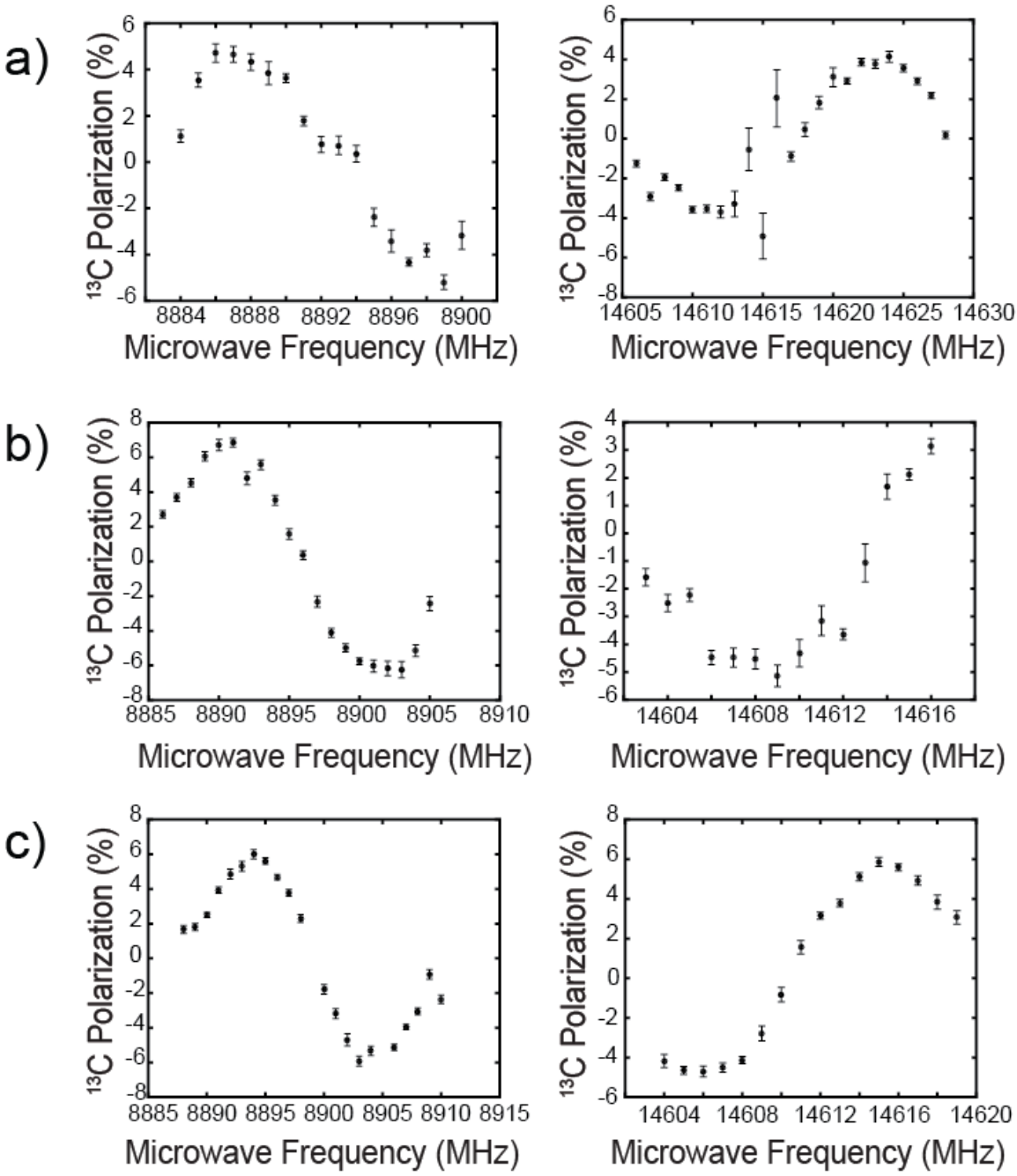

Supplementary Figure 2: Hyperpolarization as a Function of 532 nm Laser Intensity: a) 11 Wcm^{-2} , b) 16 Wcm^{-2} , c) 45 Wcm^{-2} . Increased laser intensity results in a slight increase in nuclear polarization. The frequency shifts are attributed to the temperature dependence of the zero-field splitting.

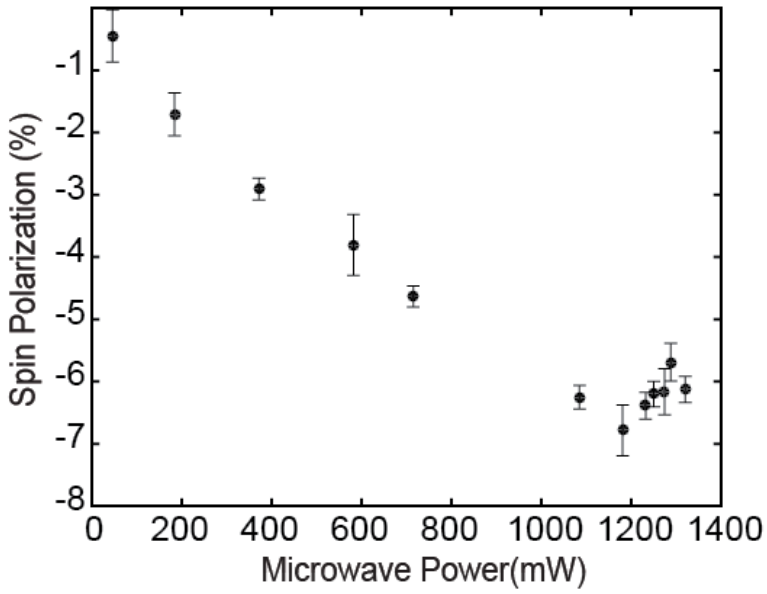

Supplementary Figure 3: Hyperpolarization as a Function of Microwave Power: Nuclear spin polarization as a function of microwave power after 60 s of DNP at 8896 MHz and 16 Wcm^{-2} illumination.

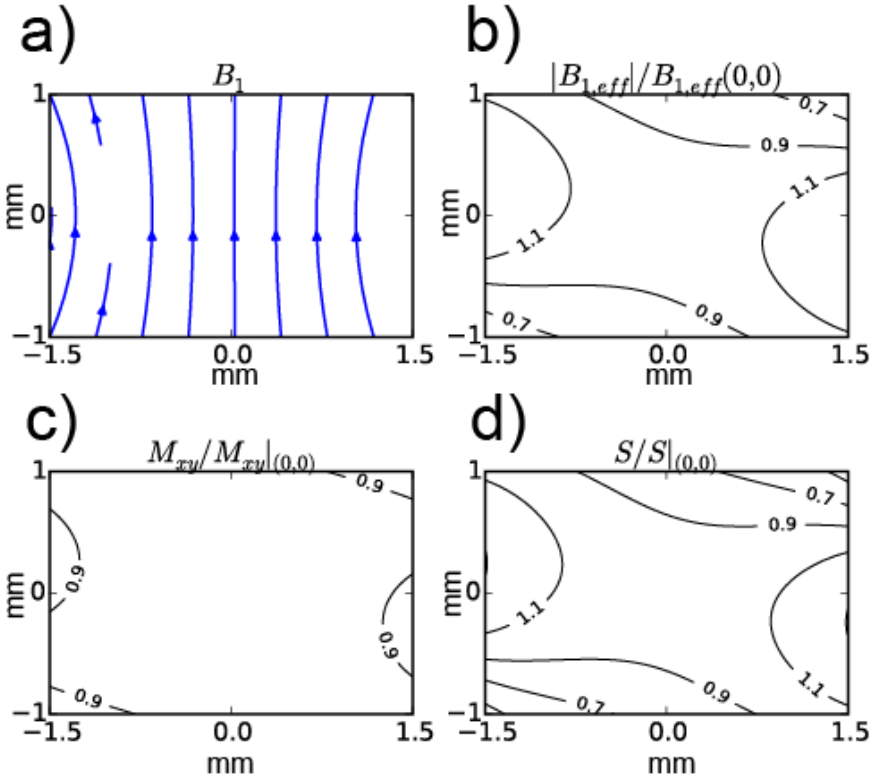

Supplementary Figure 4: B1 Field Homogeneity: a) Cross-section of field lines for RF pulses from planar NMR coil. b) Effective RF field perpendicular to the static magnetic field oriented 54.74◦ to the coil axis. c) Normalized nuclear magnetization generated by a nominal π/2 pulse. d) Overall NMR sensitivity as a function of position, accounting for generation of transverse nuclear magnetization and inductive sensitivity of the coil.

Supplementary Note 1. The mechanisms for DNP via fixed paramagnets in insulating solids are well known and described elsewhere (30-32). We briefly review the relevant mechanisms here. For a diamond containing ^{13}C and NV^- spins, there exist transitions at frequencies $\omega_{NV} \pm \omega^{13}_{C}$ involving simultaneous nuclear and electron spin flips that are nominally forbidden in the absence of electron-nuclear coupling. Dipolar coupling of these spins creates a non-zero transition probability, and a sufficiently strong microwave field may then drive the transition. These transitions are either zero quantum (induced by coupling terms of the form $S\pm I\mp$) or double quantum ($S \pm I \pm$) and may be selected by frequency. Since optical pumping of the NV^- center populates the $m_s = 0$ states, each of these transitions is polarized and the effect of driving the forbidden transitions is to preferentially induce nuclear spin flips of a particular sign. Thus, the net result of the combined optical pumping and microwave irradiation is to preferentially populate one of the nuclear spin states. This is known as the the solid effect method of DNP, since it relies on the dipolar interaction of fixed spins in solids (30-32). If, however, the NV^- spin transitions are homogeneously broadened by their mutual dipole dipole interactions, as is the case with high NV^- concentrations, then there exist energy-conserving transitions that involve a nuclear spin flip accompanied by multiple NV^- spin flips. In this case the dipolar energy reservoir of the NV^- centers is in thermal contact with the nuclear spins. This coupling can provide a relaxation pathway for the nuclear spins or, if the dipolar spin temperature is perturbed by optical pumping or microwave saturation, it can provide a second method of DNP known as thermal mixing (31, 33, 34). Application of microwave irradiation connects the dipolar energy reservoir to the electron Zeeman energy in the rotating frame (35), and thus provides a pathway for electron spin polarization transfer to nuclei. The solid effect and thermal mixing DNP have similar dependencies on microwave frequency, where the maximum polarization occurs offset on either side of the ODMR transition. The results presented here likely contain contributions from both solid-state effect and thermal mixing effects. We expect the relative magnitudes of these effects to be sample dependent, owing to differing NV^- concentration.

Supplementary Note 2. The effectiveness of the OP/DNP process was found to increase slightly with laser intensity. While the exact relationship between laser intensity and NV^- spin polarization under these conditions is unknown, it is clear that optical absorption is significant over the depth of the diamond. The optical absorption coefficient in the diamond is approximately 9 mm^{-1}, and at thickness of 0.32 mm, only 6% of the light is transmitted. Increasing the laser light then effectively increases the volume of the sample that is highly polarized as well as possibly increasing the degree of polarization near the surface of the sample. Supplementary Figure 2 shows DNP data as a function of laser intensity. We also note the frequency shifts in the DNP data as a function of laser power; we attribute this to the temperature-dependence of the zero-field splitting (36). The effectiveness of OP/DNP also increases with applied microwave power (Supplementary Figure 3). This is consistent with DNP mechanisms in diamond, where the solid effect or thermal mixing mechanisms of DNP are expected to contribute. In the case of the solid-effect, the increased microwave power will more effectively drive the forbidden transitions involving mutual spin flips of ^{13}C and NV^- spins. For thermal mixing, the microwaves drive the NV^- dipole energy reservoir into equilibrium with rotating frame spin temperature of the NV^- centers. In each case, stronger microwave irradiation can result in more efficient transfer of polarization.

Supplementary Note 3. Typically, when performing quantitative NMR studies a reference sample of known quantity is mixed with the sample and observed under identical conditions. However, observing ^{13}C NMR at 420 mT is inherently difficult due to the low sensitivity, and without hyperpolarization it is impossible to observe an NMR signal with the same number of scans as the DNP experiments. We therefore used a 99% ^{13}C enriched sample of dimethyl sulfoxide, doped with gadolinium (III) to achieve a spin-lattice relaxation time less than 2 ms. This allowed accumulation of the more than 10,000 scans needed to achieve a sufficient signal-to-noise ratio for the thermally-polarized liquid whose polarization was 3.5×10^{-7}. In order for the calibration to be accurate, several conditions must be met. First, all the parameters of the NMR experiment must remain constant, including pulse parameters and the quality factor of the resonant probe. Additionally, the reference sample should match the diamond in shape and be positioned identically with respect to the NMR coil to avoid miscalibration from the inhomogeneous sensitivity of the NMR coil. Care was taken to maintain all experimental parameters, but the problem of inhomogeneous sensitivity requires additional consideration. As it was impractical to use a liquid sample with identical dimensions as the diamond (2 mm × 2 mm × 0.32 mm), a cylindrical liquid sample of diameter 3.7 mm and approximate depth 2 mm was used. Assuming the pulse parameters are calibrated to give a $\pi/2$ rotation at the center of the coil, the rotation angle was estimated as a function of position by numerically simulating the magnetic field (B1) of the RF coil. Sensitivity to sample magnetization is also proportional to B1, and these values were combined to create a map of sensitivity as function of position (Supplementary Figure 4). From these simulations it was estimated that the NMR sensitivity for the DMSO liquid reference sample was approximately 99% that of the diamond sample, and we conclude that RF field inhomogeneities do not cause significant error in the calibration. There are a variety of other possible sources of error in the calibration of the diamond ^{13}C polarization, including the measurement of the number of spins in the diamond and DMSO sample, the deviation of the coil sensitivity from the numerical simulations, and possible drifts in the quality factor of the probe. However, the primary source of error is expected to be the noise relative to the weak calibration signal. This noise was characterized by fitting the DMSO spectrum with a Lorentzian function as described earlier and obtaining an error estimate of 6.7%. This error applies uniformly to the calibration of all DNP data and is thus not represented as individual error bars. This possible error does not affect the conclusions of this study.

Chapter 2

Nuclear spin hyperpolarization from nitrogen vacancy centers in ^{13}C enriched diamonds

2.1 Abstract

We report high field hyperpolarization of ^{13}C-enriched diamonds (10%, 25%, 100%) at room temperature by using combined optical pumping of nitrogen vacancy (NV^-) defects and microwave irradiation. Compared with previous results from a natural abundance diamond, we observed a similar hyperpolarization from a 10% ^{13}C enriched sample, with decreasing polarization for higher ^{13}C concentrations. It is shown that increasing ^{13}C concentration broadens the optically detected magnetic resonance spectrum via hyperfine interactions and also enhances nuclear spin diffusion, which is the rate-limiting step in the polarization process. In this hyperpolarization mechanism, NV^- centers and their nearest ^{13}C spins may be considered as a hyperpolarized composite spin system that gives rise to dynamic nuclear polarization of weakly-coupled ^{13}C spins. These results suggest that ^{13}C enriched diamond may be superior to natural abundance for proposed polarization transfer and contrast agent applications, with an optimum ^{13}C concentration between 10% and 25%

2.2 Introduction

Nuclear magnetic resonance (NMR) and magnetic resonance imaging (MRI) are indispensable techniques in chemistry, engineering, and medicine. Despite their utility, these techniques suffer from low sensitivity, which is due in large part to the low magnetization of the sample. The magnetization of a sample stems from the low average polarization and thus low magnetization of the nuclear spins in the sample. This polarization is typically generated by allowing spins to thermally equilibrate in a large magnetic field. Unfortunately, even in the highest fields available (~20 Tesla) the polarization of ^{13}C nuclear spins at room temperature is less than 0.004 %. As a result, there is much interest in methods to generate non-equilibrium nuclear spin polarization. Perhaps foremost among these methods is the transfer of spin polarization to nuclei from electron spins, which possess a higher equilibrium polarization (1-4). This process, known as dynamic nuclear polarization (DNP) has been very successful, but still requires high fields and low temperatures to approach percent-level nuclear polarization (5,6). Therefore, it would be desirable to harness an electron spin that may be hyperpolarized at room temperature in order to perform hyperpolarized DNP. One promising candidate is the nitrogen vacancy (NV^-) center in diamond, which can have near complete polarization under optical pumping at room temperature (7-11). Recently, our group reported optically-pumped

DNP of natural abundance ^{13}C spins in diamond at room temperature (12). Hyperpolarized ^{13}C nuclei in diamond have been suggested for use as MRI contrast agents (13-15), as well as a platform for polarization transfer to external nuclei (8-16). In either case, it would be desirable to increase the concentration of ^{13}C nuclear spins. In this paper, we report NV^- DNP hyperpolarization of ^{13}C-enriched diamonds. In addition to enhancing the total nuclear magnetization of the sample, increasing the ^{13}C influences the DNP mechanism through enhanced nuclear spin diffusion and hyperfine splitting of the electron spin resonance spectrum. We show that the NV^- and its nearest neighbor ^{13}C spins may be considered as a hyperpolarized composite spin system that gives rise to DNP of more weakly-coupled nuclear spins.

2.3 Methods

DNP experiments were performed using a setup described previously (12). Diamonds with varying ^{13}C enrichment ($\sim$ 3 x 3 x 0.43 mm, 10 %, 25 %, 100 %) were purchased from Applied Diamond Inc. which used chemical vapor deposition methodology (CVD) for synthesizing diamonds with various ^{13}C concentrations, determined by the feed gas mixture. Three (100) oriented single crystal diamond wafers were grown by CVD with different ^{13}C concentrations (10 %, 25 %, 100 %) by changing the ^{13}C-methane feed gas concentration. The concentration of substitutional nitrogen in the diamond, which is typically < 1 p.p.m. for standard grade CVD diamond, was augmented by increasing [N] of the feed gas to 600 ppm. Electron irradiation at 1 MeV (Prism Gem) followed by annealing at 800 °C for 2 h formed NV^- centers. Each sample was mounted on a goniometer inside an electromagnet and a [1 1 1] axis was aligned with the magnetic field by monitoring the ODMR spectrum. With the field set to $\sim$ 420 mT, microwave excitation for optically detected magnetic resonance (ODMR) and DNP experiments was performed using a simple wire loop near the sample. The nuclear polarization was monitored via the magnitude of the NMR signal acquired using a Magritek Kea 2 with a homebuilt 50-turn planar coil probe tuned to $\sim$ 4.5 MHz. The nuclear polarization was taken to be proportional to the integrated area of the frequency domain NMR signal. NMR signal was observed from the different ^{13}C concentration samples after accumulating 20 $\sim$ 60 scans with a repetition time of 60 seconds (Fig. 2). For comparison and calibration, reference data from previous literature (12) was used, which is reasonable since we used the exact same parameters for DNP and NMR signal acquisition with same set up except sample size, and the amount of polarization was estimated. To measure polarization buildup curves, a series of saturation pulses was applied followed by a variable polarization time and a 90° pulse to acquire the bulk ^{13}C signal.

2.4 Results and discussion

The electronic ground state of the NV^- center is a spin-1 triplet with a zero-field splitting D = 2.87 GHz between the $m_s = \pm1$ and $m_s = 0$ states. First-shell ^{13}C spins experience a hyperfine coupling to the NV^- center of approximately 130 MHz (17, 18). Applying a magnetic field along the defect symmetry axis lifts the degeneracy of the $m_s = \pm1$ states (Fig. 1a) which gives rise to the main magnetic resonance transitions (with additional hyperfine splittings). ODMR is

observed through a reduction in the fluorescence intensity induced by depopulation of the m_s = 0 state (Fig. 2, signals are reversed to compare with DNP signals. The first shell of nuclei may contain 0 to 3 ^{13}C spins which split each resonance into 1 to 4 peaks. Interactions with second and third shell ^{13}C spins (10 ~ 20 MHz) contributes to each peak's broadness (17, 19). All of these nuclear spins may be considered as strongly hyperfine coupled since the hyperfine interaction exceeds the nuclear Zeeman interaction. ^{13}C nuclei further from the NV$^-$ centers are weakly coupled and give the dominant contribution to the bulk NMR signal. (Fig. 1b)

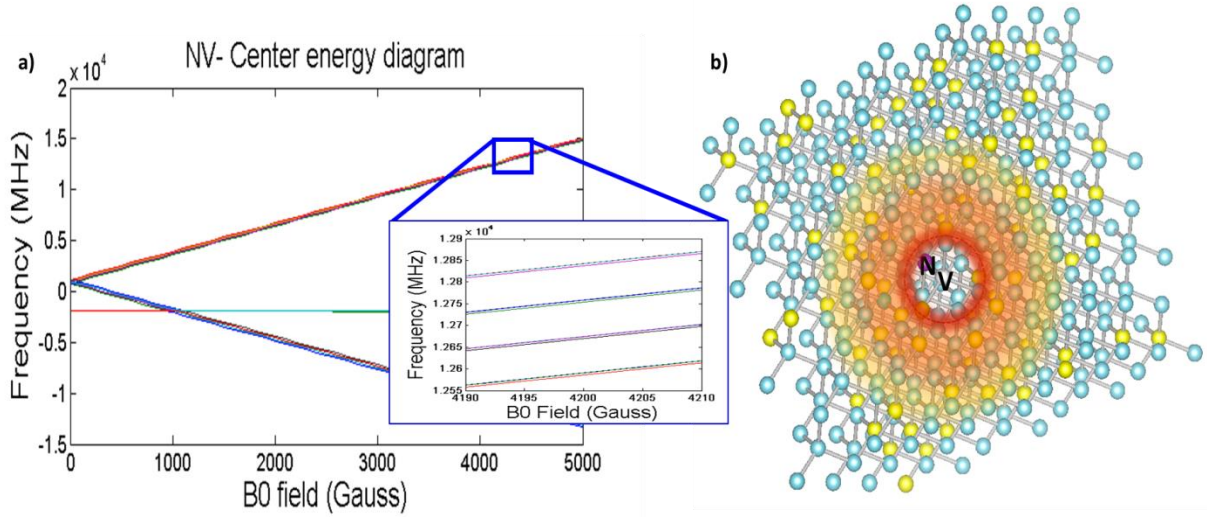

Figure 1. Energy level structure for the NV$^-$ center and 3 nearest-neighbor ^{13}C spins with a magnetic field aligned along the defect symmetry axis. a) For this spin system, NV$^-$ spin state energy levels are split into a quartet structure: four resonances with intensity ratios of approximately 1:3:3:1. Each quartet corresponds to 8 electron-nuclear spin states resulting from the different possible combinations of ^{13}C nuclear spins. (b) Bulk ^{13}C spins (yellow ball) are hyperpolarized through DNP by pumping of an electron-nuclear spin transition.

For each sample, the intensity of the DNP-enhanced signal at each frequency was roughly proportional to the derivative of the ODMR spectrum, as expected for DNP mechanisms where the EPR line width is greater than ω_I (Fig. 2) (1). This trend holds true even for transitions corresponding to hyperfine splittings of the NV$^-$ spectrum induced by first-shell ^{13}C nuclei, indicating that the composite spin system comprising the NV$^-$ and proximate nuclei acts to polarize weakly-coupled nuclear spins. This mechanism is distinct from the situation where first-shell nuclei are directly polarized (9-11, 20) with subsequent transport of polarization to the bulk (8). For each sample, the ^{13}C polarization was measured as a function of microwave frequency. The 10% ^{13}C sample showed a similar polarization to previous studies of a natural abundance diamond in the same experimental setup. The 25% and 100% samples yielded lower polarizations compared to the 10% sample. The 100% ^{13}C sample yielded a doublet NMR spectrum as expected for a fully enriched sample (see Supporting Information for detailed simulation). (Fig. 3)

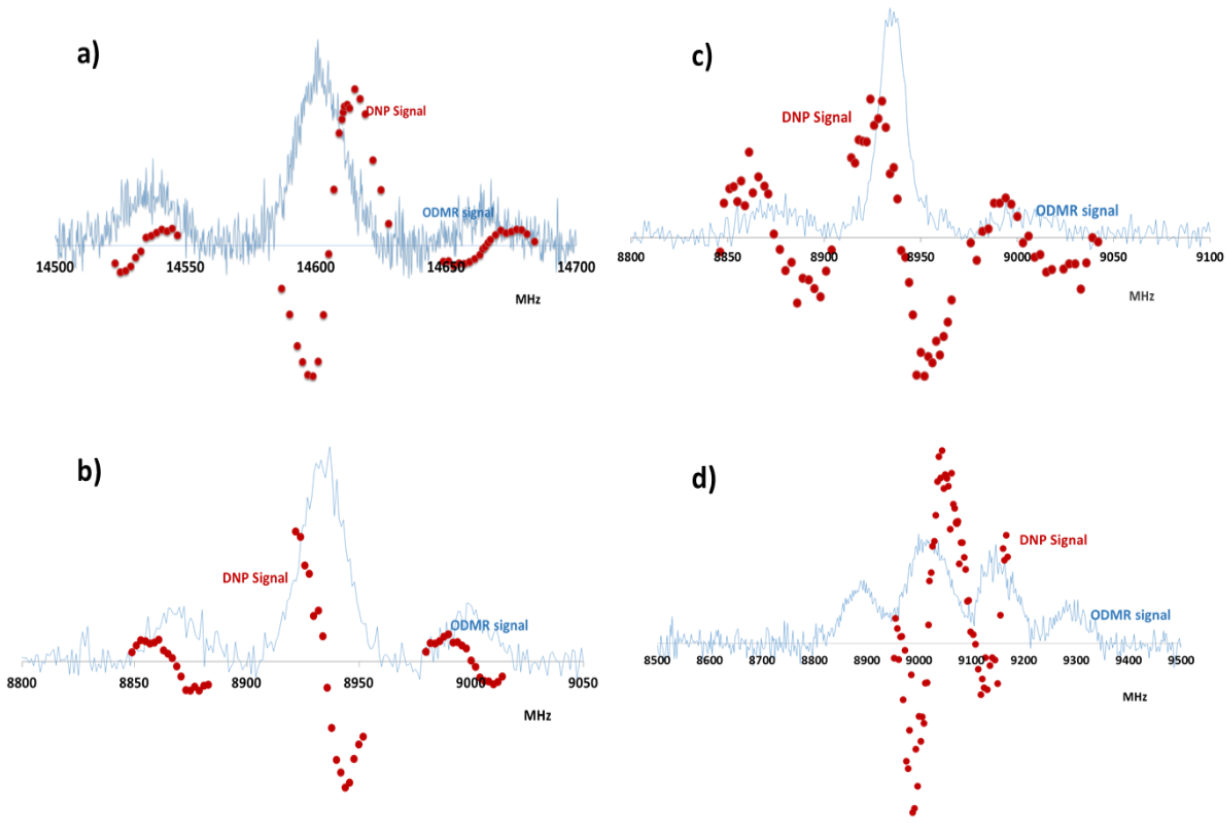

Figure 2. ODMR of NV^- centers in diamond with varying levels of ^{13}C enrichment compared to the ^{13}C NMR signal upon DNP enhancement as a function of applied MW frequency. The ODMR spectra, normally displayed as a decrease in fluorescence intensity, are inverted for better comparison with the NMR signal. Each ODMR spectrum was acquired with 4000 averages. a) 10% ^{13}C enriched sample, ODMR of the |0> ↔ |+1> NV^- spin transition with the ^{13}C NMR signal accumulated over 60 scans. The two minor ODMR signals correspond to hyperfine coupling to one first-shell ^{13}C spin. b) 10% ^{13}C enriched sample, ODMR of the |0> ↔ |-1> NV^- spin transition with the ^{13}C NMR signal accumulated over 20 scans. c) 25% ^{13}C enriched sample, ODMR of the |0> ↔ |-1> NV^- spin transition with the ^{13}C NMR signal accumulated over 60 scans. d) 100% ^{13}C enriched sample, ODMR of the |0> ↔ |-1> NV^- spin transition ODMR with the ^{13}C NMR signal accumulated over 60 scans. The quartet ODMR spectrum corresponds to hyperfine coupling to 3 first-shell ^{13}C spins.

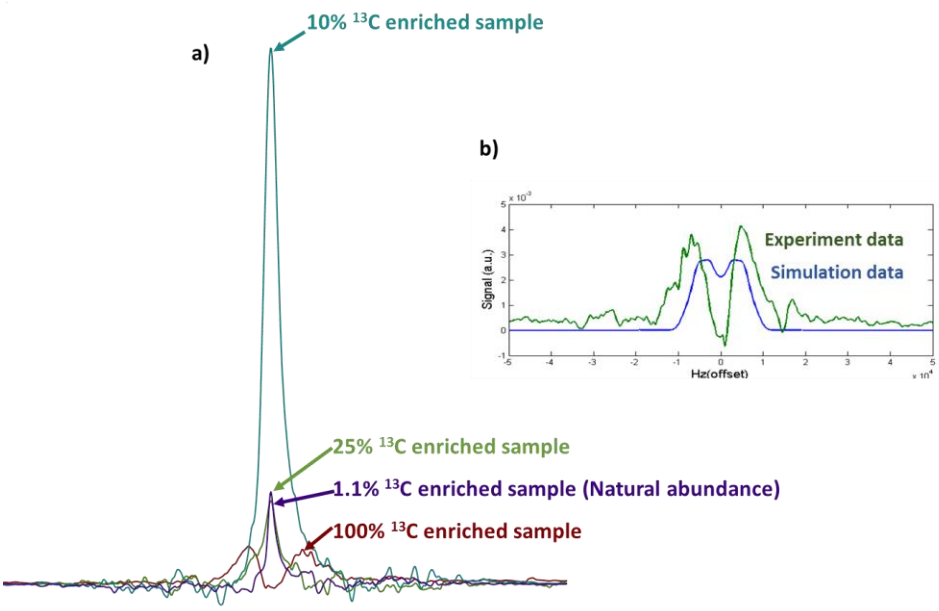

Figure 3. Signal intensity comparison for various ^{13}C enriched samples using 60 seconds as a polarization buildup time for each scan. a) 10 % ^{13}C enriched sample signal is obtained with 20 scans. 1.1 %, 25 % ^{13}C enriched samples' signals were obtained with 60 scans and 100 % ^{13}C enriched sample signal was obtained with 600 scans. b) The doublet in the ^{13}C NMR signal intensity of 100 % ^{13}C enriched sample may be described as a Pake doublet, where the splitting is dominated by nearby dipolar interactions (21). (Simulated signal : blue line, 8 kHz split, experiment signal : green line, 11 kHz, See Supporting Information for detailed simulation code)

The polarization buildup for each sample is plotted in Fig. 4a. Each sample's data was fitted with exponential function (1-exp (-t/τ)), where τ is the buildup time. The increasing polarization rate with ^{13}C concentration suggests that nuclear spin-diffusion is the the rate-limiting step.

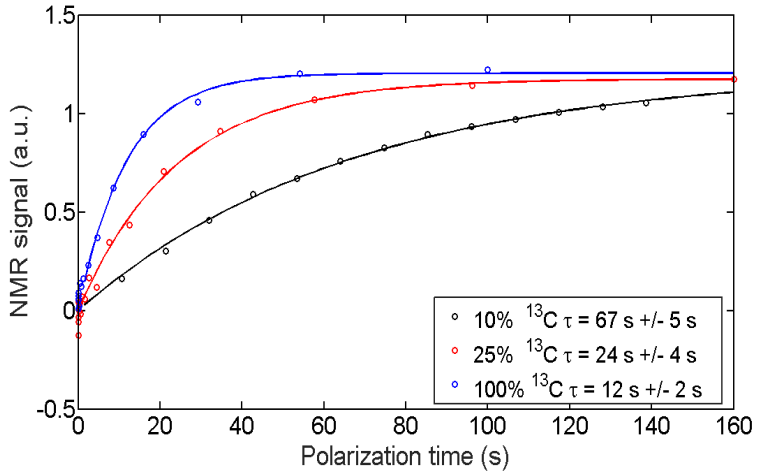

Figure 4. ^{13}C polarization buildup time as a function of ^{13}C enrichment of the diamond samples. After series of initial saturation pulses, variable polarization time was used to measure the nuclear spin polarization buildup time. Each DNP build up data was normalized and fitted with exponential function (1-exp (-t/τ)). DNP build up times are different in different ^{13}C concentration.

2.5 Conclusion

These results demonstrate that composite spin systems of NV^- centers and strongly coupled nuclei are effective sources of hyperpolarization for weakly coupled nuclear spins. However as the electron spin spectrum is broadened by ^{13}C coupling the efficiency is decreased. The natural abundance and 10% enriched ^{13}C diamond yielded the largest hyperpolarization while higher ^{13}C concentration resulted in lower polarization, suggesting an optimum ^{13}C concentration. The relationship between the DNP and ODMR spectra is consistent with thermal mixing or cross effect DNP mechanisms where the derivative of the electron spin resonance spectrum is proportional to the DNP efficiency. Furthermore, the dependence of the DNP buildup time on ^{13}C concentration suggests nuclear spin diffusion is the rate-limiting step in the process. Understanding the mechanism of optically pumped DNP in ^{13}C enriched diamonds is critical for both polarization transfer applications and use of hyperpolarized diamonds as MRI contrast agents. In each case, a high ^{13}C concentration is desirable. We anticipate the extension of this work to ^{13}C enriched diamond nanocrystals with high-surface area.

2.6 Supporting Information

Pake doublet simulation (matlab code)

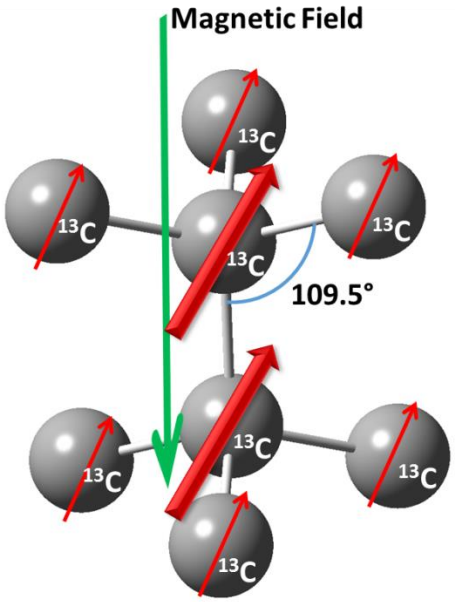

Figure S1. 100% ^{13}C enriched diamond lattice for the simulation. Two aligned spins' dipolar interaction (big red arrows) contributes the Pake doublet.

1) Dipole energy splitting calculation function

```
function dipoleinteraction_output=dipole(theta,r)
%calculation carbon dipole energy splitting (Hz), theta=degree, r= nm between 13C
u= 1.2566370614*10^-6;
hbar=1.054571*10^-34;
gyro=67.262*10^6; %13 carbon gyromagnetic ratio
dipoleinteraction_output=3*u*gyro*gyro*hbar*(3*(cos(theta/(180/pi)))^2-
1)/(4*pi*2*2*pi*(r*10^(-9))^3)
end
```

2) Dipole energy splitting calculation

```
dipole(0,0.153); % 111 direction dipole coupling
main_d=ans; % splitting between two signal
dipole(109.5,0.153); % 3 different orientation dipole coupling
minor_d1=1/2*ans; % splitting between 1/2 spin angular moment
minor_d2=3/2*ans; % splitting between 3/2 spin angular moment
sigma=1350; % change with line width (empirical number)
int = 5 % change intensity (empirical number)
a=xlsread('100% signal data'); % 100% 13C sample doublet experimental data
x=a(:,1);
y=a(:,2);
y2=1*y; % change intensity for second plot (empirical number for comparision)
fright1=int*1/2*1/sqrt(2*pi)/sigma*exp(-(x-(main_d/2-minor_d2)).^2/2/sigma/sigma);
fright2=int*3/2*1/sqrt(2*pi)/sigma*exp(-(x-(main_d/2-minor_d1)).^2/2/sigma/sigma);
fright3=int*3/2*1/sqrt(2*pi)/sigma*exp(-(x-(main_d/2+minor_d1)).^2/2/sigma/sigma);
fright4=int*1/2*1/sqrt(2*pi)/sigma*exp(-(x-(main_d/2+minor_d2)).^2/2/sigma/sigma);
fleft1=int*1/2*1/sqrt(2*pi)/sigma*exp(-(x-(-main_d/2-minor_d2)).^2/2/sigma/sigma);
fleft2=int*3/2*1/sqrt(2*pi)/sigma*exp(-(x-(-main_d/2-minor_d1)).^2/2/sigma/sigma);
fleft3=int*3/2*1/sqrt(2*pi)/sigma*exp(-(x-(-main_d/2+minor_d1)).^2/2/sigma/sigma);
fleft4=int*1/2*1/sqrt(2*pi)/sigma*exp(-(x-(-main_d/2+minor_d2)).^2/2/sigma/sigma);
f=(fright1+fright2+fright3+fright4+fleft1+fleft2+fleft3+fleft4);
figure;
subplot(3,1,1);
plot(x,f)
subplot(3,1,2);
plot(x,y2)
subplot(3,1,3);
plot(x,f,x,y2)
```

3) Simulation data

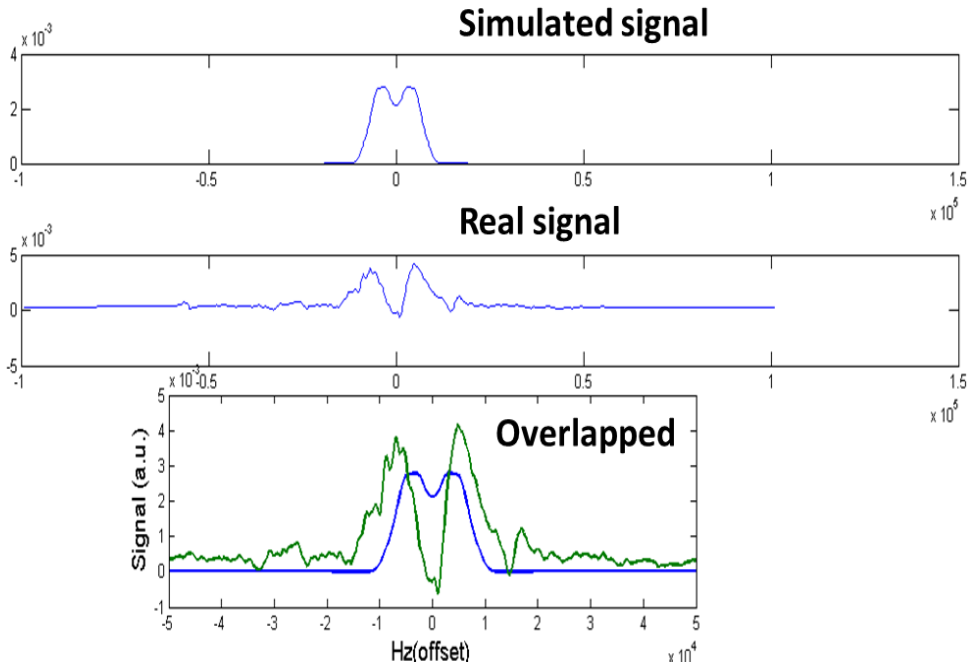

Figure S2. Simulation output for doublet

(111) oriented NV$^-$ center energy state simulation (matlab code)

```
%calculation energy state with 13C and 14N
load paulispin1.mat %Pauli spin matrix of S=1
Bi=4190;
Bstep=0.1;
Bf=4210;
n=size(Bi:Bstep:Bf,2); %Bi starting magnetic field, Bstep increment, Bf final field
for k=1:n
B=Bi+(k-1)*Bstep;
H = +2.8*B*Siz+2870*(Siz*Siz-(Six*Six+Siy*Siy+Siz*Siz)/3)...
 +3.25*(Six*Six-Siy*Siy); %Hamiltonian only for electron
       [Efuc(:,:,k), Eval(:,:,k)]=eig(H);
        a(:,:,k)=max(Eval(:,:,k)); %l+1>state choose
    end
    aa=[];
    for k=1:n
    aa=[aa,a(1,3,k)]; %aa is the energy l+1> state
    end
     i = -3:2:3;
      i=i';
```

```
    b=[];
for k=1:n
b =[b aa(k)+129*(+1)*(1/2*i)-0.010705*B*i/2]; %1st shell hyperfine interaction + 13C larmor
end
%Q =quadruple coupling 5MHz, hyperfine =2.2MHz M0=0, M+1=-5MHz, M-1 =-0.6MHz
bbb=[];
for i=1:n
   bb=[];
   for k=1:4;
bb= [bb ; b(k,i);b(k,i)-0.6;b(k,i)-5]; %adding nitrogen hyperfine interaction
  end
 bbb=[bbb,bb];
end
figure;
plot(Bi:Bstep:Bf,bbb)
```

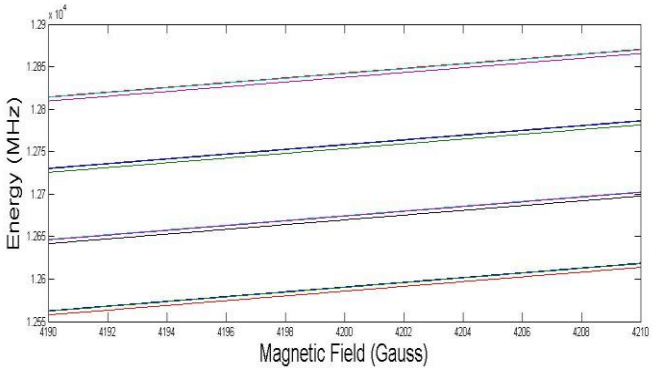

Figure S3. Short magnetic field range, l+1> state only

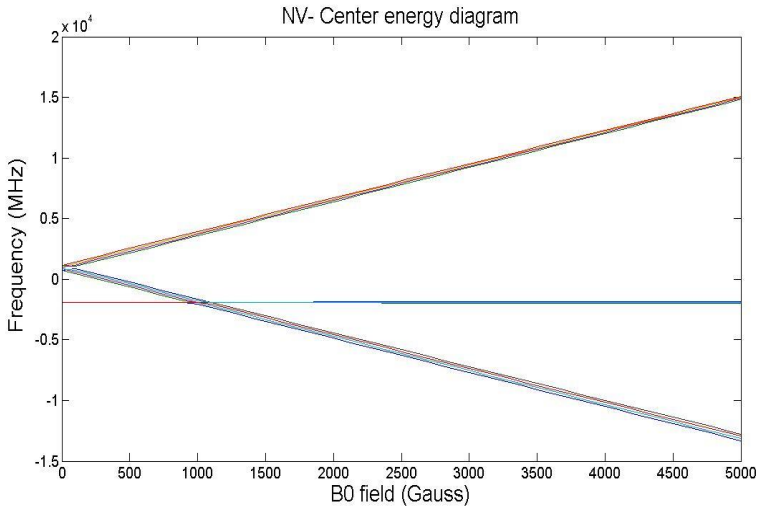

Figure S4. Long magnetic field range, l0>, l-1>, l+1> states

Chapter 3

Two-dimensional optically-detected magnetic resonance of nitrogen vacancy centers in nanocrystalline diamond powder

3.1 Abstract

We present 2-dimensional optically-detected magnetic resonance spectra of nitrogen vacancy defects in single crystals and diamond powders. This allows, for the first time, the observation of the powder pattern generated by the random distribution of crystal orientations in a magnetic field. The data are well described by numerical simulations from the zero- to high-field regimes, including the intermediate regime of maximum complexity. We identify overtone transitions that are inherently less sensitive to crystal alignment. These results are important in the rapidly expanding field of dynamic nuclear polarization with NV^- diamond, where the use of high surface area nanodiamonds will be used for polarization transfer to external materials.

3.2 Introduction

The negatively-charged nitrogen vacancy center (NV^- center) diamond with its spin-1 ground state, optical spin polarization and readout enables many emerging applications such as high spatial resolution magnetometry (1), solid state qubits, MRI contrast agents (2), and nuclear spin hyperpolarization (3). Nuclear spin hyperpolarization may be accomplished through a number of techniques including energy matching via a choice of magnetic fields to create a hyperfine-mediated avoided crossing, application of microwaves to drive polarization to strongly-coupled nuclei, and microwave-induced dynamic nuclear polarization (DNP) to directly polarize bulk nuclear spins (4-8). However, in order for NV^- hyperpolarization to become a useful technique, it will be necessary to transfer polarization from diamonds to external samples of interest, either through one of the direct processes mentioned above or indirectly through the diamond ^{13}C nuclei. In either case, the process necessarily takes place at the diamond surface. As such, high-surface area powders of diamond nanocrystals are a system of great interest (9, 10). However, since the NV^- spin properties depend strongly on orientation with respect to the external magnetic field, powders of randomly oriented crystals pose additional challenges.

In this study, we observe 2-dimensional optically detected magnetic resonance (ODMR) of NV^- diamond single crystals and powders. We observe, for the first time, the full powder pattern of the NV^- center spectrum from the zero- to high-field regimes. Furthermore, we identified sharp

$\Delta m \cong 2$ overtone transitions that are independent of orientation in the high-field regime. All aspects of the data were well-matched by numerical simulations taking into account the energy level structure and distribution of spin population as a function of crystallite orientation.

3.3 Experiments and results

2D ODMR in a single diamond. A 2 x 2 x 0.2 mm [1 0 0] surface oriented single crystal of synthetic HPHT diamond containing 7.8 ppm NV^- centers was mounted in our ODMR apparatus with a [1 1 1] or [1 0 0] axis aligned along the magnetic field (7). 2-dimensional ODMR were obtained by collecting spectra over a range of magnetic field values (Figure 1).

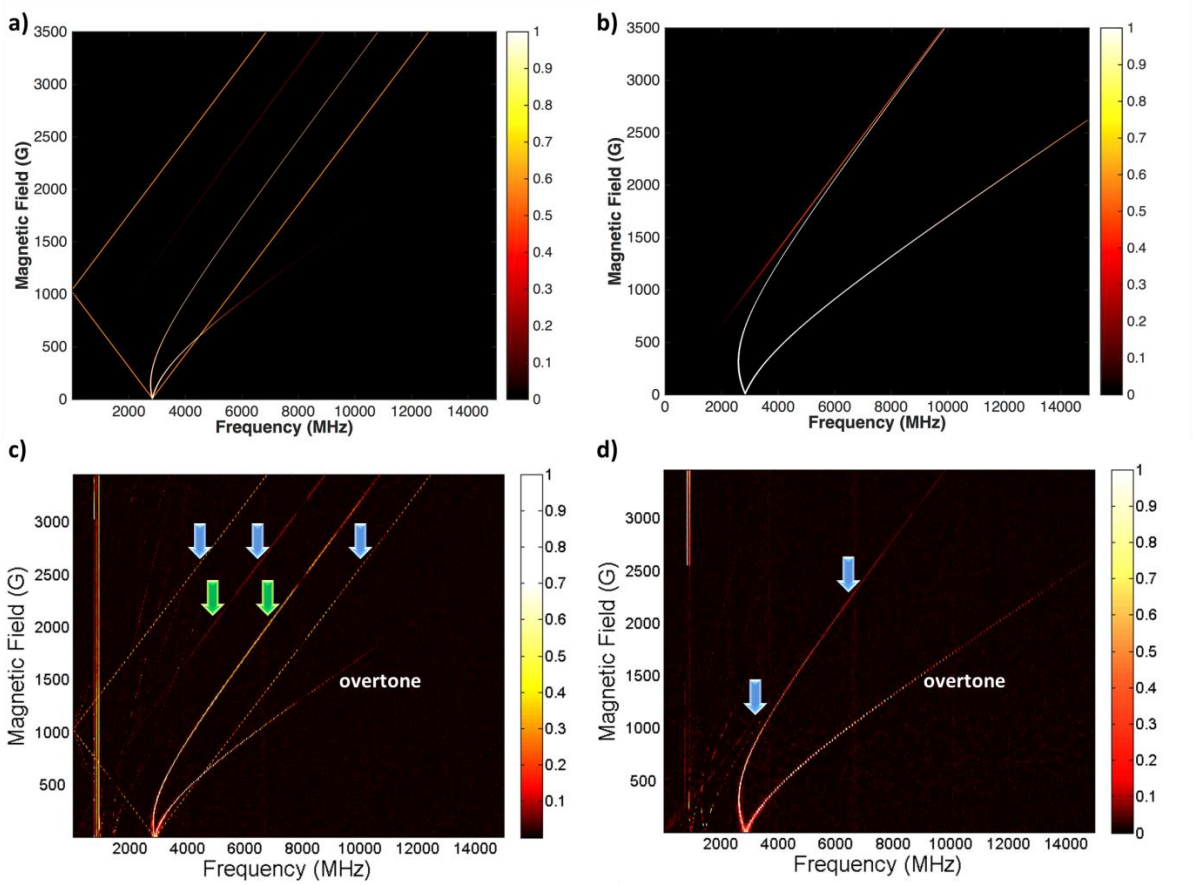

Figure 1. Single crystal 2D ODMR experimental and simulated spectra. a) Simulated 2D ODMR when the magnetic field is aligned along the [1 1 1] axis, which includes 0° and 109.5° oriented NV^- centers b) Simulated 2D ODMR when the magnetic field is aligned along the [1 0 0] axis (54.74° oriented NV^- centers) c) Observed 2D ODMR when the magnetic field is aligned along the [1 1 1] axis. Blue arrows indicate 0° oriented spectra which exhibit an avoided crossing around 1000 G. Green arrows indicate 109.5° oriented spectra which includes an overtone transition. The vertical bands are instrument artifacts resulting from radiofrequency interference between the microwave loop and the APD. Other apparent signals are generated by harmonics of the microwave amplifier as explained in the SI. d) Observed 2D ODMR when the magnetic field is aligned along the [1 0 0] axis, exhibiting single-quantum and overtone transitions.

2D ODMR observation in diamond powder. In order to investigate 2D ODMR from NV^- in diamond powder, we loaded 10 mg of nano-diamond powder with 100 nm size into an NMR tube. 2D ODMR was measured using the same method as for single crystalite, except crystal orientation is irrelevant to the powder (Figure 2d, e). For intermediate- and high-fields, the ODMR spectrum exhibited a width up to twice the zero-field splitting, or 5.74 GHz, with corresponding reduction in ODMR contrast. Previous ODMR techniques do not have sufficient signal to noise to acquire such spectra, in our case the acquisition was enabled by lock in detection. Simulated 2D ODMR provide a good fit to the observed spectra (Figure 2a-c). We also observed a sharp transition with an apparent gyromagnetic ratio twice that of the NV^- center, and another transition that approaches zero frequency at zero-field. As we will show later, these are the $\Delta m \cong 2$ overtone transitions of the NV^- center and the high-field overtone is insenstivie to crystal orientation.

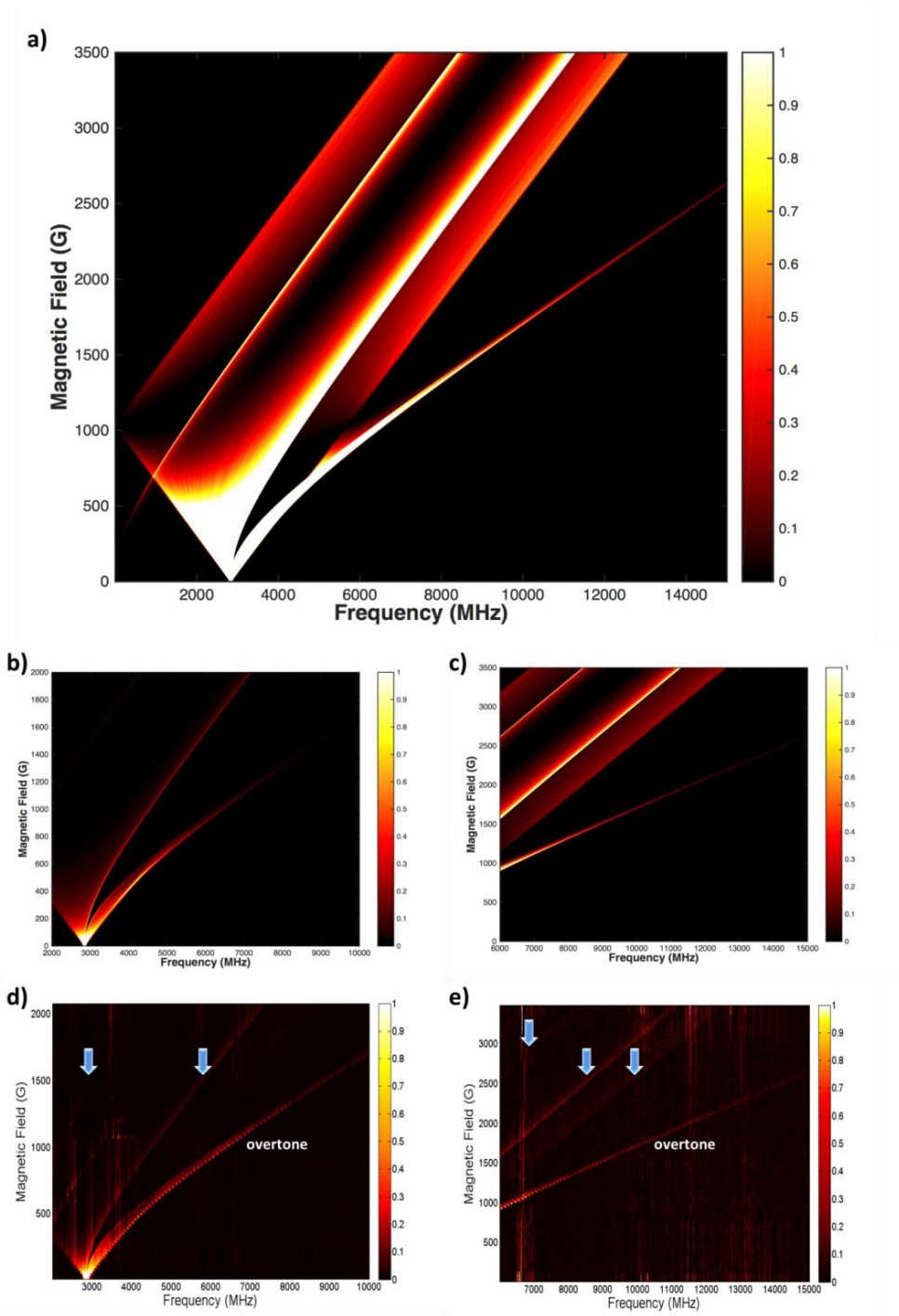

Figure 2. Simulated and experimental 2D ODMR of diamond powders. a) Predicted 2D ODMR spectrum from diamond powder. b) Simulation of NV^- diamond powder 2D ODMR ranging from 2 GHz to 10 GHz in various magnetic fields from 0 to ~2020 G, corresponding to the data in (d). c) Simulation NV^- diamond powder 2D ODMR ranging from 6 GHz to 15 GHz in various magnetic fields from 0 to 3500 G, corresponding to the data in (e). Simulations provide a good fit to experimental 2D ODMR data including overtone transitions (d, e). Overtone transitions are indicated in (d) and (e) and blue arrows indicate the single transition powder pattern (compared with simulation (b) and (c)). The vertical bands are instrument artifacts resulting from radiofrequency interference between the microwave loop and the APD. d) 2D ODMR of NV^- center in diamond powder, ranging from 2 GHz to 10 GHz in various magnetic fields from 0 to ~2020 G. e) 2D ODMR of NV^- center in diamond powder, ranging from 6 GHz to 15 GHz in various magnetic fields from 0 to ~3300 G. Noise from 2D ODMR data was filtered by subtracting with averaged data (original figures are shown in Supporting Information)

To investigate more about the overtone transitions, we obtained high SNR ODMR spectra at specific magnetic fields (985 G and 1314 G) (Figure 3). Those transitions showed powder pattern-like spectra, which are much narrower than the main NV^- powder pattern and become narrower as the field is increased.

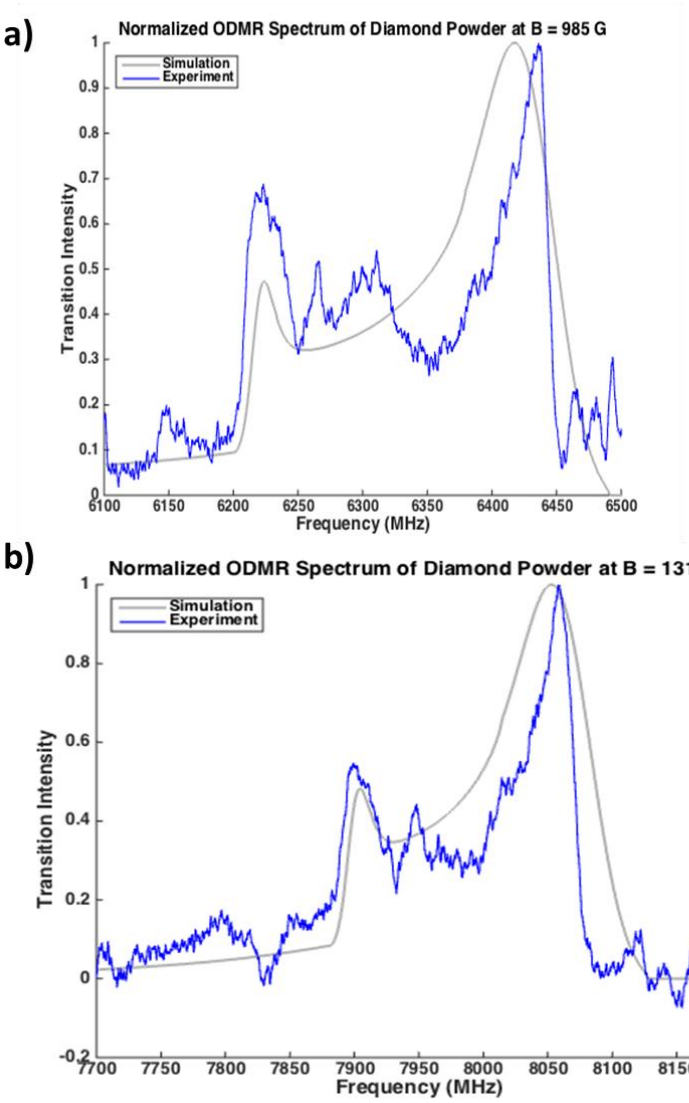

Figure 3. Simulated and experimental 1-dimensional ODMR spectra of overtone transitions. a) ODMR spectrum of the overtone transition at 985 G b) ODMR spectrum of the overtone transition at 1314 G. The powder patterns may be explained by a higher-order perturbation treatment of zero field splitting and are well fit by numerical simulations.

3.4 Discussion

Simulating NV$^-$ center spin transitions at variable field orientation for single-crystal diamond and diamond powders. Neglecting the weak hyperfine interaction with nearby ^{14}N and the rare ^{13}C nuclei, the electron spin Hamiltonian of NV$^-$ center is:

$$H = D\left(S_z^2 - \frac{1}{3}S^2\right) + \gamma_e B_z(S_x \sin\theta + S_z \cos\theta),$$

Where **D** = 2,870 MHz is zero field splitting, γ_e = 2.8 MHz/G is the electron gyromagnetic ratio, and θ is the angle between the magnetic field and the NV$^-$ axis, which lies along a [1 1 1] axis of the diamond (Figure 4).

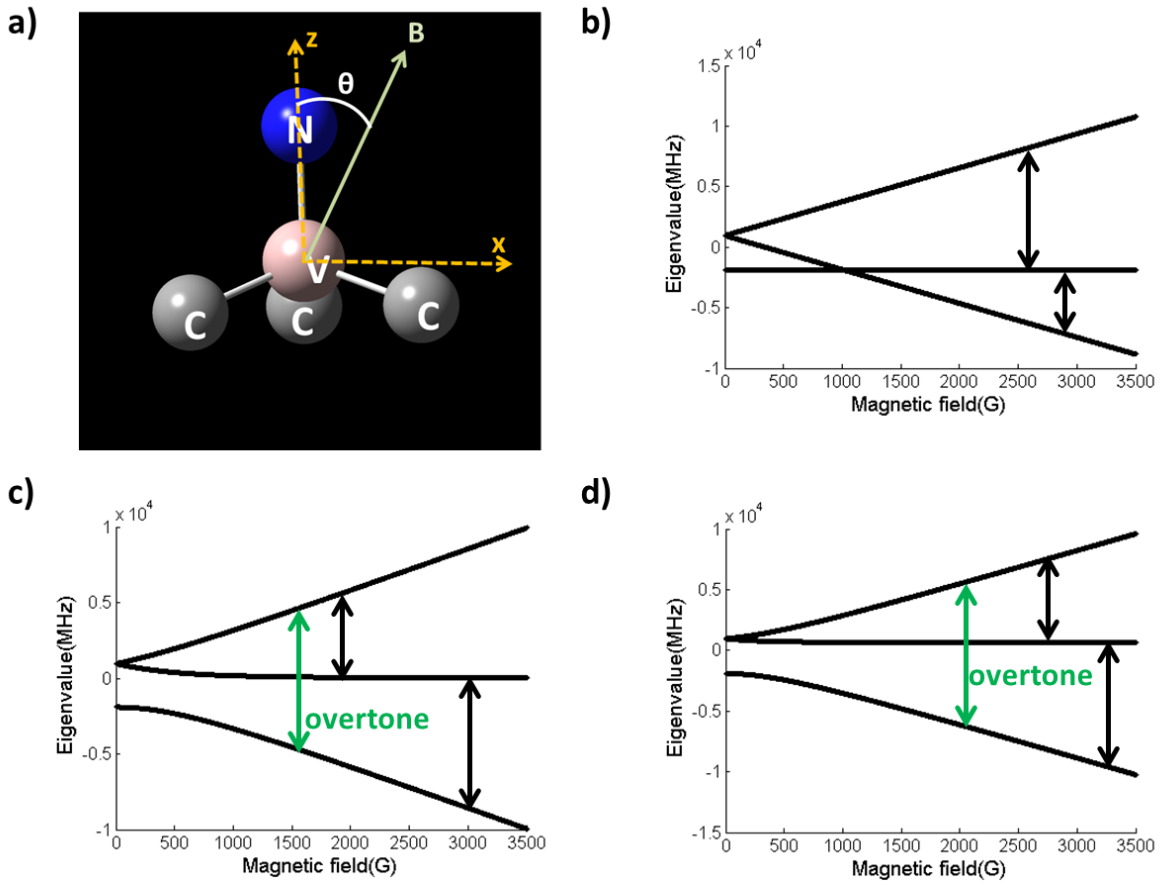

Figure 4. NV$^-$ center structure and energy states for several orientations. a) Single NV$^-$ center structure with orientation (θ). b) Eigenvalue versus magnetic field plot of 0 degree oriented NV$^-$ center. Single quantum transition is allowed (black arrow) However, overtone transition from mixed states is not allowed. c) Eigenvalue versus magnetic field plot of 54.75 degree oriented NV$^-$ center. Overtone transition is allowed. d) Eigenvalue versus magnetic field plot of 109.5 degree oriented NV$^-$ center. Overtone transition is allowed.

2D ODMR spectra of ensembles of NV^- centers in single crystal diamond and diamond powders were simulated by numerically solving for the eigenvalues and transition frequencies. The relative intensity of each transition was characterized by an ODMR intensity factor (κ) as defined in the recent study (12), which is the product of the following factors:

$$\kappa = \left(\langle\varphi_f|\gamma_e S_x|\varphi_i\rangle\right)^2 (\Delta\langle\rho\rangle)(\Delta\langle S_z^2\rangle)$$

$$\Delta\langle\rho\rangle = \langle\varphi_f|\rho|\varphi_f\rangle - \langle\varphi_i|\rho|\varphi_i\rangle$$

$$\Delta\langle S_z^2\rangle = \langle\varphi_f|S_z^2|\varphi_f\rangle - \langle\varphi_i|S_z^2|\varphi_i\rangle$$

where $\langle\varphi_f|\gamma_e S_x|\varphi_i\rangle$ is the transition matrix element of the final and initial eigenstates involved in the transition, $\Delta\langle\rho\rangle$ describes the predicted population difference of the two eigenstates involved in the transition, and $\Delta\langle S_z^2\rangle$ is used to estimate the optical contrast of the transition, which depends solely on the electron spin state. For calculations of κ, the density operator ρ was taken to be $\rho = E - S_z^2$, which assumes only the m_s = 0 state is populated by optical pumping.

Each transition *n* was represented as a Gaussian function with amplitude κ and width $\Delta\upsilon_n$. We make the first-order assumption that the linewidth and thus the spin dephasing time T_2^* of these transitions are determined only by a distribution of fluctuating magnetic fields which, on the time scale of continuous-wave experiments, average to a small static magnetic field from other electronic and nuclear spin defects in the diamond host. The linewidth may therefore be calculated using the following relation

$$\Delta\upsilon_n = \Delta\upsilon_0 \Delta m_{s,n}$$

where $\Delta\upsilon_0$ is an empirically-determined linewidth and $\Delta m_{s,n}$ is the change in the z component of the electron spin angular momentum for transition n, given by:

$$\Delta m_{s,n} = \langle\varphi_{f,n}|S_z|\varphi_{f,n}\rangle - \langle\varphi_{i,n}|S_z|\varphi_{i,n}\rangle$$

For a resonance of NV^- centers in single-crystal diamond, this value is found to be 30 MHz and is estimated to be 50 MHz from fitting the spectra of NV^- centers in diamond powders.

Simulation of the spectra of NV^- centers in diamond powders requires the summation of spectra over a range of angles as well as magnetic fields. The probability density of finding a crystal axis forming an angle θ with the external field is $\frac{1}{2}\sin\theta$ assuming the crystal axes are randomly distributed. Sampling variable orientations in a manner that is proportional to angular distribution therefore requires the transformation $dz = \sin\theta\, d\theta$ or $z = \cos\theta$ (13). A uniform sampling of z then approximates the random distribution of NV^- orientations in a nanodiamond powder.

Overtone Transitions. Magnetic dipole transitions have rigorous selection rules of $\Delta m = \pm 1$ or $\Delta m = 0$ for transverse and longitudinal irradiation, respectively. However, when the crystal axis and magnetic field are not aligned, m is no longer a good quantum number and all transitions

are allowed. We can roughly consider the overtone transition in 3 regions. Near zero-field, there exists a $\Delta m \cong \pm 2$ transition as defined by the crystal axis. This transition trends towards zero frequency and zero intensity as the magnetic field goes to zero. At intermediate fields, $D \cong \gamma B$, the energy levels are quite mixed and no distinct overtone transition is observed. At high field, the quantization axis becomes the external field and again a $\Delta m \cong \pm 2$ is observed, this time with effective gyromagnetic ratio of 2γ. In both the high-field regime, the transition energy is independent of crystal orientation to a first-order approximation, and the powder pattern observed for these transitions are much narrower than the main $\Delta m \cong \pm 1$ transition. The overtone powder pattern observed in Fig. 3 can be attributed to second- and higher-order corrections to the energy levels and becomes narrower as these terms are suppressed at higher fields.

3.5 Conclusion

Two-dimensional ODMR spectra ranging from zero-field to the high-field regime in single crystals and powders are well described by a model accounting for the angular dependence of transition energies, spin polarization, and optical contrast. In addition to the $\Delta m = \pm 1$ transitions, $\Delta m = \pm 2$ overtone transitions are observed with much narrower width. The presence of intrinsically-narrow transitions in a powder spectrum may provide an opportunity for dynamic nuclear polarization from high surface area nanocrystals, where the main powder pattern is too wide to be accessed by standard DNP techniques. The high-field overtone transition has an enhanced gyromagnetic ratio, approximately twice that of the main transitions, that will be useful for magnetometry and sensing applications, because the overtone transition has double the response to external fields compared to the other single transitions.

3.6 Methods

Materials and experiments In order to investigate 2D ODMR in a single crystal, A 2 x 2 x 0.2 mm [1 0 0] surface oriented single crystal of synthetic HPHT diamond (Sumitomo Electric Carbide Inc.) was used after forming NV^- centers by electron irradiation at 1 MeV and annealing at 800 °C for 2 hours. Instrumental set up is same as our previous NMR research (7) except lock-in detection for singnal amplification. The sample was mounted in a goniometer inside an electromagnet. The electromagnet was designed and tested by the maker (TEL-Atomic Inc.). In each magnetic field, energy state transitions in the single crystal diamond are measured by fluorescence intensity decreases after optical pumping followed by microwave irradiation at each microwave frequency. In detail, 532 nm laser (Coherent 1222934, 1.0 W in indicator) was illuminated for optical pumping. Microwave irradiation was performed with a loop near the sample and fluorescence intensity was collected by avalanche photodiode (ThorLabs Inc). To increase signal to noise, measurement used a lock-in amplifier included in the ODMR setup (SR830 DSP). Using a microwave synthesizer, microwave frequencies from 1 MHz to 15 GHz, with a 1 MHz increment, are transferred to a broadband amplifier (Minicircuits Inc) and amplified microwaves irradiated the sample through a copper loop sited on the oriented

sample in an electromagnet. Each data point was averaged 3 times. For investigating 2D ODMR of diamond powder, we purchased 10 mg of nano-diamond powder with 100 nm size (Adamas Nano Technology Inc.) and loaded into a 3 mm NMR tube. Fluorescence detection was carried out with the same way as for the single crystal case. To increase the sensitivity from randomly oriented diamond powder, we lowered microwave frequency increment by 0.25MHz and used higher power amplifiers. For the acquiring overtone single transition with higher signal to noise, we averaged 100 repeated scans.

Simulation All simulations and data processing were done with custom scripts written in MATLAB (The Mathworks, Inc). For simulations of spectra of single crystal samples, where only one angle defining the NV^- axis orientation is considered, the NV^- spin Hamiltonian is diagonalized for a range of magnetic field values. For each value of magnetic field, the predicted energy (υ), intensity (κ), and linewidth (Δυ) of all possible transitions are calculated and associated with a Gaussian lineshape. To form the 2D plot, the intensity of the predicted lineshape as a function of frequency is binned by frequency unit and assigned to an array element by its corresponding frequency and the value of magnetic field at which the transition occurred. Colorbars defining the intensity range in each figure are given in arbitrary units and scaled to match what is observed experimentally. In order to simulate the 2D spectra of NV^- centers in a nanodiamond powder, we sampled 10^5 values in z for $-1 \leq z \leq 1$ and converted them to values of θ (for $0 \leq \theta \leq \pi$) to simulate a spectrum of 10^5 crystallites (Figure 2a-c). The 2D plot was generated using the same procedure as for simulating a single NV^- orientation, where the 2D spectra for each value of θ are summed to give the total 2D spectrum.

3.7 Supporting information

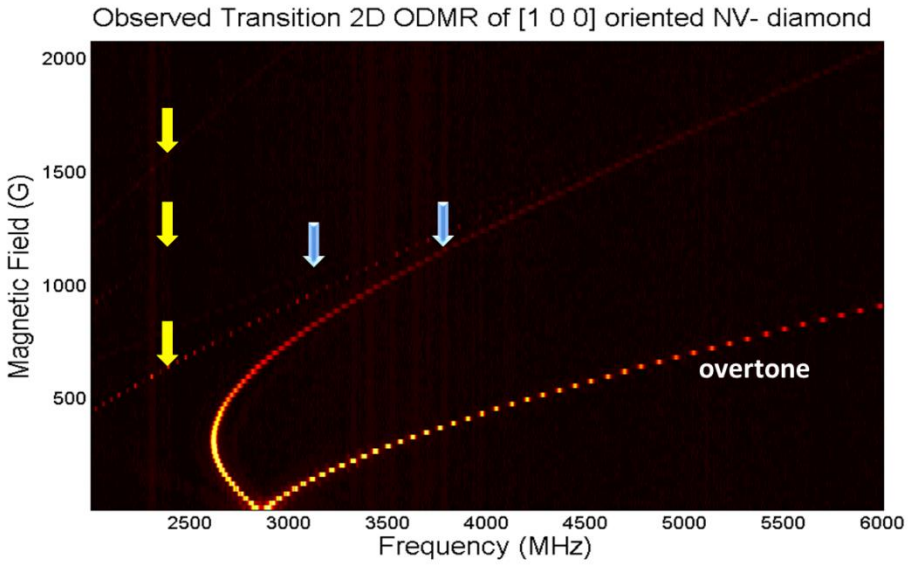

Figure S1. Single crystal 2D ODMR data plots with regard to the magnetic field (Yellow arrows are the second, third harmonic signals which are half / one third of main transition frequency signals) Blue arrows represent single transition which fits with the simulation.

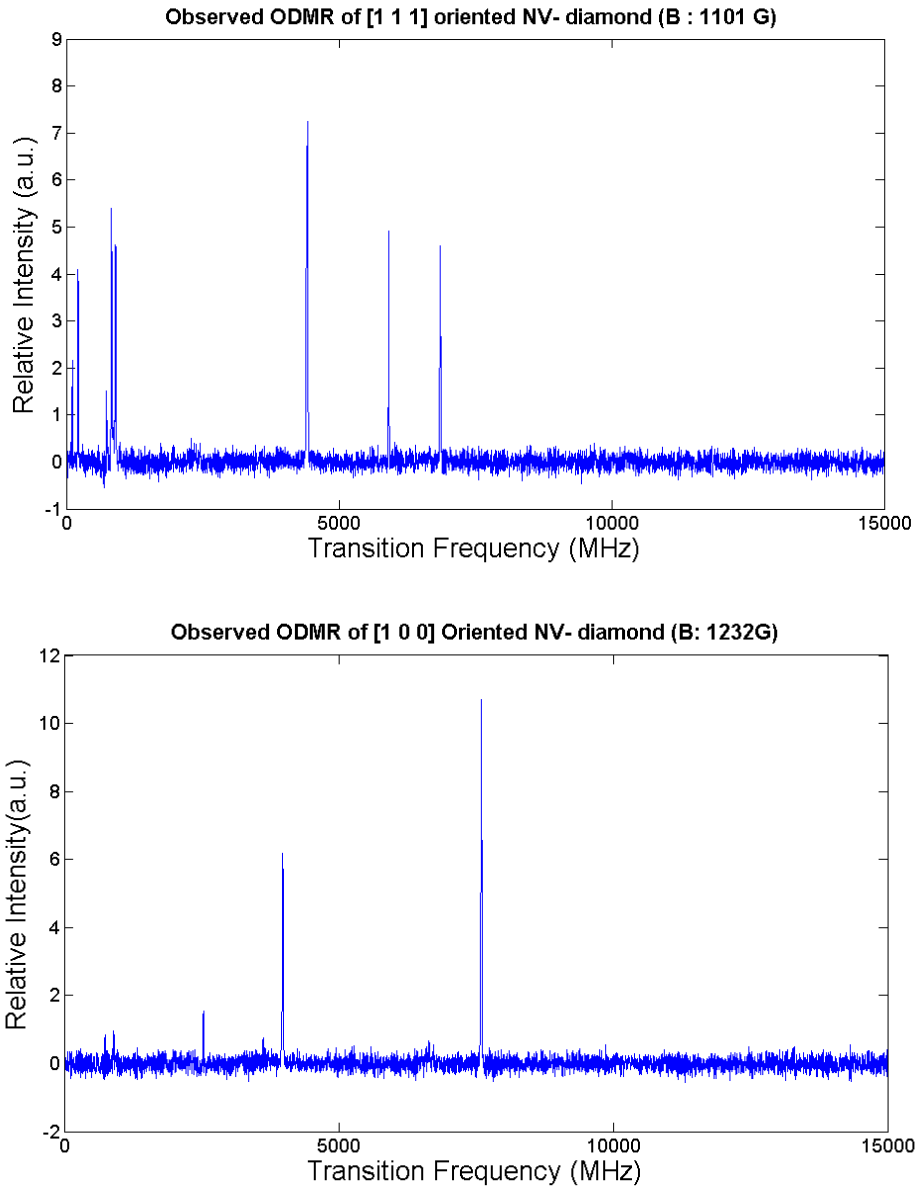

Figure S2. Single ODMR transitions which are extracted from each 2D ODMR of single crystal.

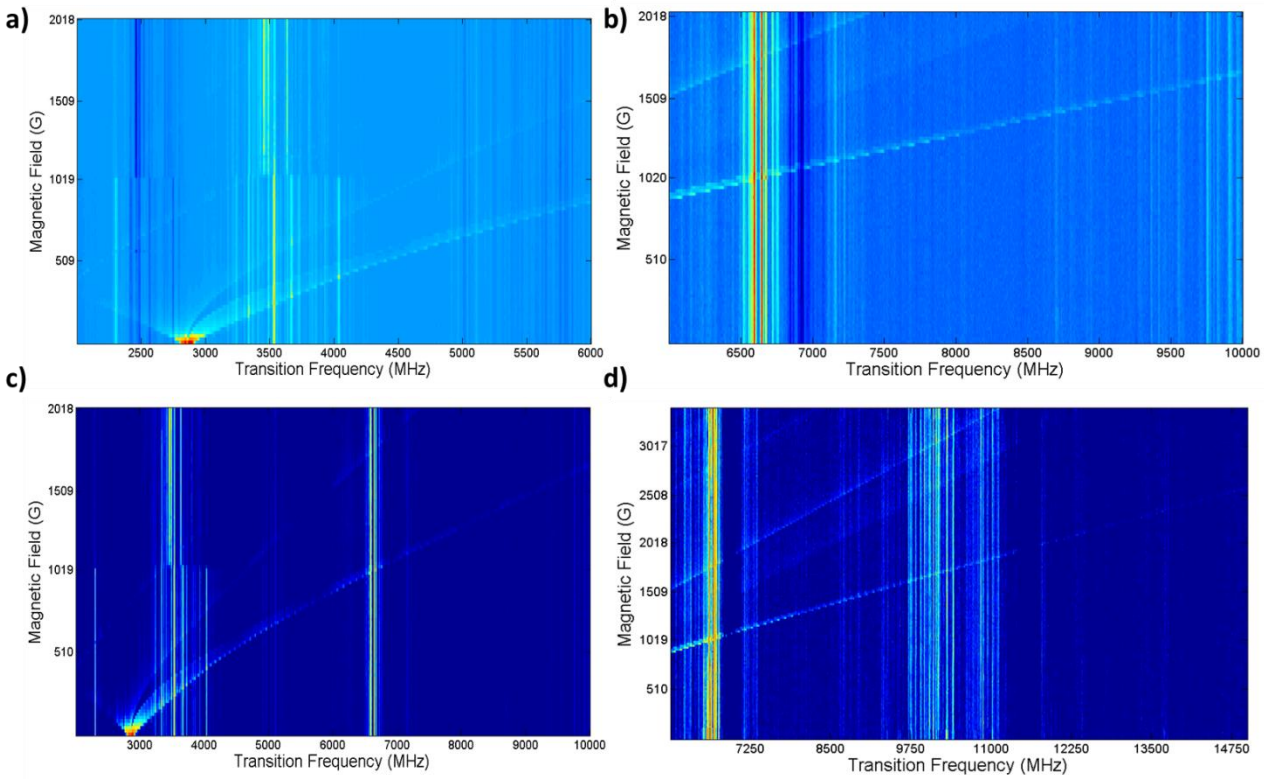

Figure S3. Observed 2D ODMR data without noise filtering. a) 2D ODMR of NV^- center in diamond powder, ranging from 2 GHz to 6 GHz in various magnetic fields from 0 to ~2020 G. b) 2D ODMR of NV^- center in diamond powder, ranging from 6 GHz to 10 GHz in various magnetic fields from 0 to ~2020 G. c) Combined figure of a) and b). d) 2D ODMR of NV^- center in diamond powder, ranging from 6GHz to 15GHz in various magnetic fields from 0 to ~3300 G.

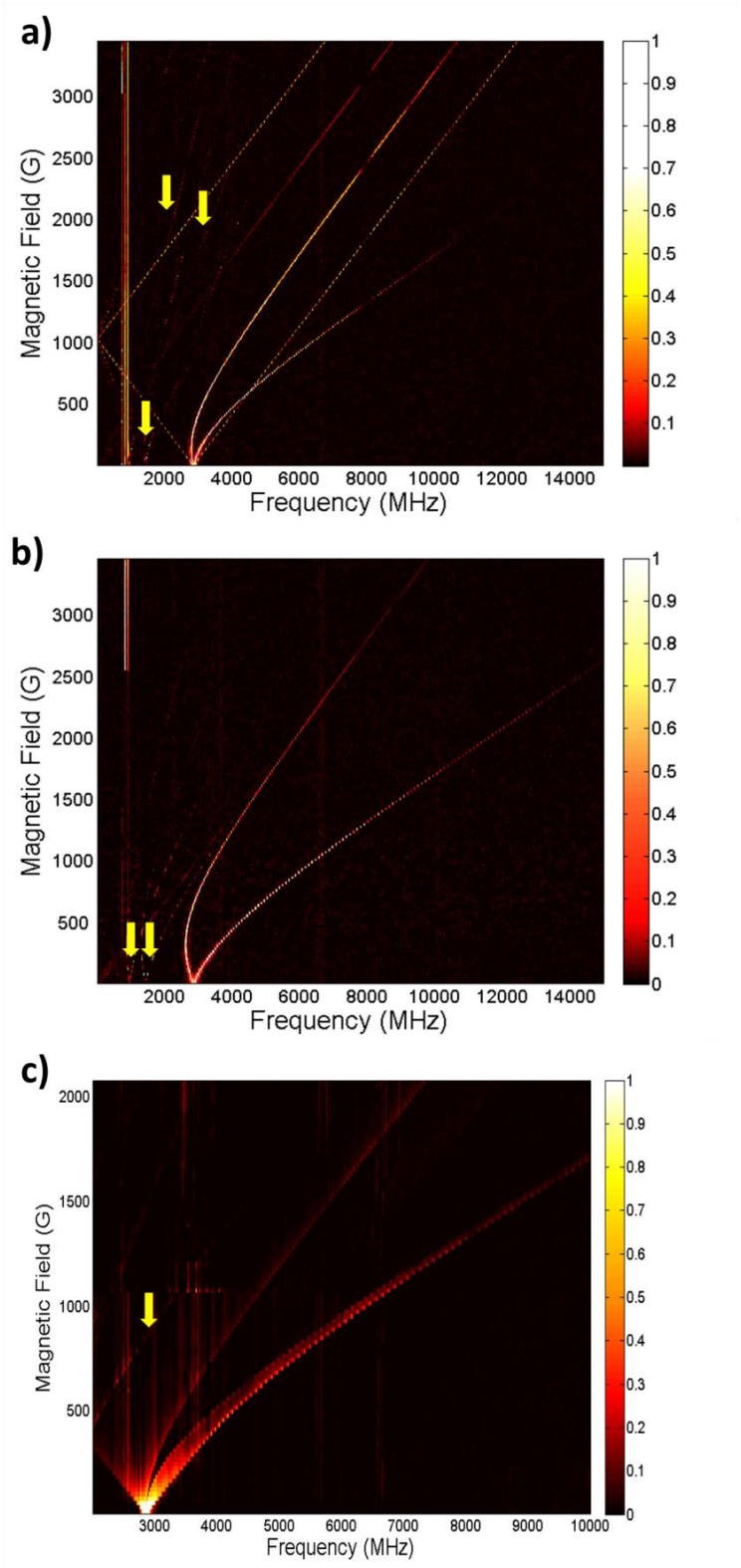

Figure S4. Yellow arrows indicate harmonic signals from observed 2D ODMR data. There are several vertical bands which are instrumental artifacts resulting from radiofrequency interference between the microwave loop and the APD.

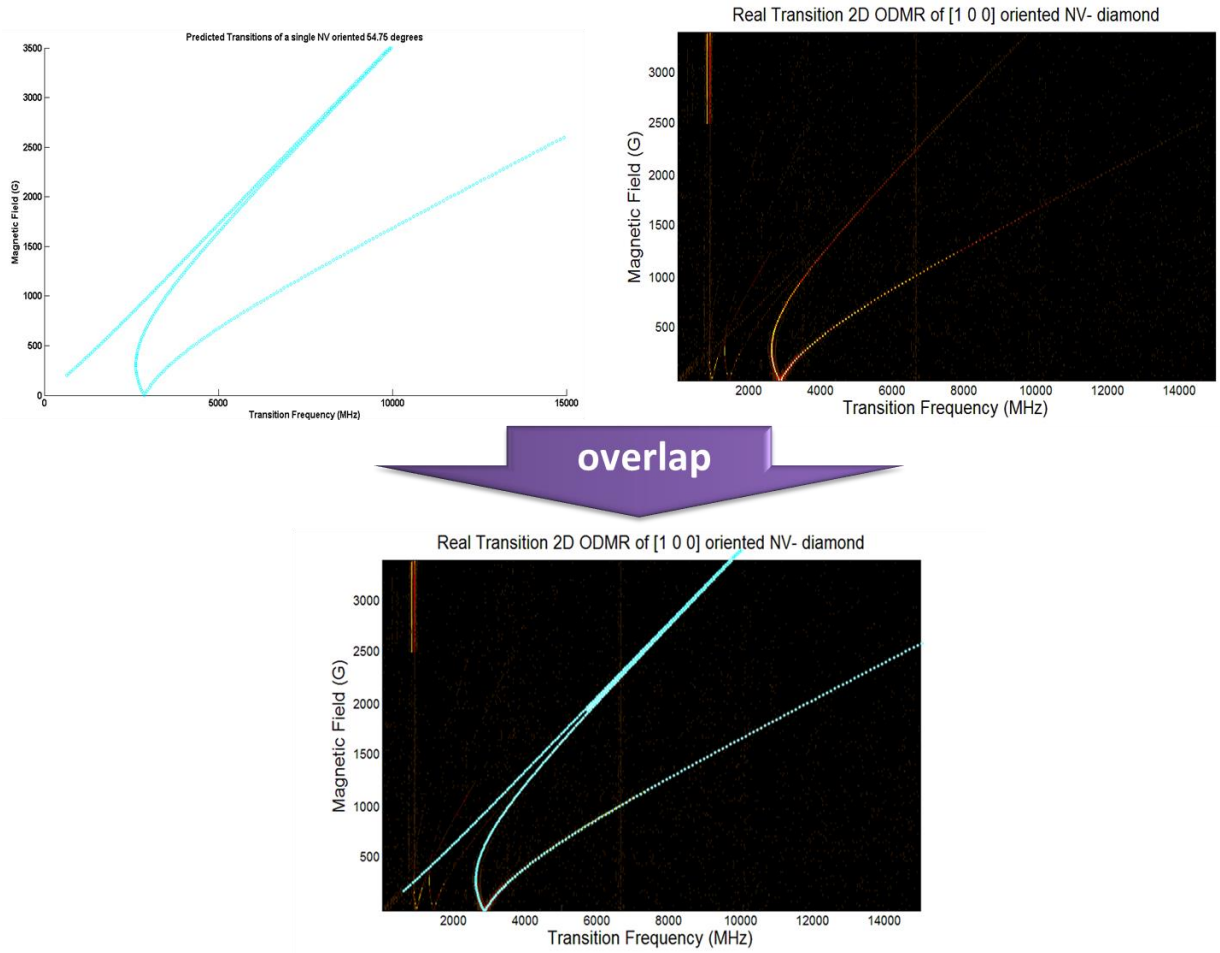

Figure S5. Overlap simulated 2D ODMR for the real 2D ODMR in single crystal case. It shows that the simulation is perfectly matched with observed data.

Chapter 4

Investigation of DOTA-Metal Chelation Effects on ^{129}Xe Chemical Shift

(This is reprint from ChemPhysChem, 2015, 16, 3573-3577: "Investigation of DOTA-Metal Chelation Effects on ^{129}Xe Chemical Shift.", **Keunhong Jeong**, Clancy C. Slack, Christophoros C. Vassiliou, Phuong Dao, Muller D. Gomes, Daniel J. Kennedy, Ashley E. Truxal, Lindsay J. Sperling, Matthew B. Francis, David E. Wemmer, and Alexander Pines.)

4.1 Abstract

Recent work has shown that xenon chemical shifts in cryptophane-cage sensors are affected when tethered chelators bind to metals. Here, we explore the xenon shifts in response to a wide range of metal ions binding to diastereomeric forms of 1,4,7,10-tetraazacyclododecane-1,4,7,10-tetraacetic acid (DOTA) linked to cryptophane-A. The shifts induced by the binding of Ca^{2+}, Cu^{2+}, Ce^{3+}, Zn^{2+}, Cd^{2+}, Ni^{2+}, Co^{2+}, Cr^{2+}, Fe^{3+}, and Hg^{2+} are distinct. In addition, the different responses of the diastereomers for the same metal ion indicate that shifts are affected by partial folding with a correlation between the expected coordination number of the metal in the DOTA complex and the chemical shift of ^{129}Xe. These sensors may be used to detect and quantify many important metal ions, and a better understanding of the basis for the induced shifts could enhance future designs.

4.2 Introduction

Metal ions are very important in biological and environmental systems (1). Some, including $Fe^{2/3+}$, Cu^{2+}, Co^{2+}, Zn^{2+}, and Ni^{2+}, play essential roles in human metabolism (2), whereas others, including Hg^{2+}, Cd^{2+}, and Pb^{2+}, are toxic (3). Although there are well-established methods for the in vitro detection of metals, including atomic absorption spectroscopy and various electrochemical techniques (4), a practical technique that can simultaneously and nondestructively detect multiple metal ions would be a valuable addition to the existing analytical methods. Conventional NMR spectroscopy can distinguish between different chemical species, but is difficult to apply to complex mixtures.

Although many metals have spin-active isotopes that can be detected by NMR spectroscopy, the sensitivity is generally very low. Here, we exploit the strong signals of hyperpolarized xenon, which are associated with a cryptophane cage carrying a metal chelator, to report the presence of metals through binding-induced shifts.

Hyperpolarized ^{129}Xe NMR/MRI has emerged as a promising in vivo imaging tool that is being explored extensively for the imaging of the lungs by using inspired xenon (5) and the study of brown fat and brain tissues by using dissolved xenon (6). Additional work in vitro has established hyperpolarized ^{129}Xe NMR/MRI as a method for the selective, high-sensitivity detection of proteins (7), enzyme activity (8), nucleic acids (9), and cell surface receptors (10). ^{129}Xe is useful as a reporter for a number of reasons: 1) There is no naturally occurring ^{129}Xe in the body, so there are no background signals that must be suppressed. 2) ^{129}Xe displays a large chemical shift in response to its physical and chemical surroundings, making it a sensitive reporter of the surrounding environment. 3) The ^{129}Xe NMR polarization is long-lived. Spin-exchange optical pumping of xenon can achieve almost complete polarization of the ^{129}Xe nuclei and allows the detection of low concentrations of ^{129}Xe dissolved in solution (11).

Recent work by Zhang et al. (12) and Kotera et al. (13) developed cryptophane sensors that respond to Zn^{2+}, inducing a change in the chemical shift of the cryptophane-bound ^{129}Xe NMR peak upon metal binding. Changes in the chemical shifts were also observed upon binding Pb^{2+} and Cd^{2+} ions (14). In the current work, we use the chelator 1,4,7,10-tetraazacyclododecane-1,4,7,10-tetraacetic acid (DOTA), which binds a wide range of metals with very high affinity, coupled to cryptophane-A and a solubilizing Glu_5 peptide (M0; Figure 1). We investigated a larger group of metals compared with previous work, including several that are paramagnetic. A comparison of the shifts induced by the different metals provides insight into the origin of the shifts, which may facilitate the design of improved multi-metal sensors.

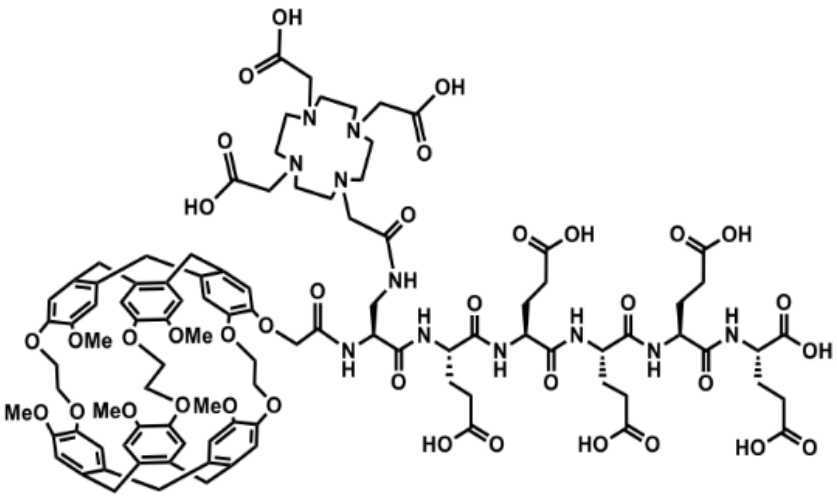

Figure 1. Sensor comprised of a cryptophane cage to bind xenon, a DOTA chelator, and solubilizing Glu_5 peptide (M0).

DOTA interacts strongly with transition-metal ions [log Ka = 22.2 (Cu^{2+}), 21.1 (Zn^{2+}), 21.3 (Cd^{2+}), 20.5 (Ni^{2+}), 20.3 (Co^{2+}), 16.4 (Ca^{2+}), 21.6 (Ce^{3+}), 24.4 (Fe^{3+}), and ≈ 23 (Hg^{2+} ; from cyclam, estimated to have similar affinity with DOTA, due to its similar chemical structure) (15), and essentially bind any free metals in a sample irreversibly. The affinity of metals for DOTA is

stronger than most biological interactions, so, in a biological context, DOTA will act as a sink accumulating metals at a rate determined by their dissociation from the endogenous ligands. DOTA is a flexible chelation agent with eight possible coordination points: four tertiary amines in the central ring and four carboxylate arms. The geometry of metal-bound DOTA is dependent on the specific metal present and its preferred coordination number (CN). Smaller metals prefer lower CN, for example six for Ga^{2+} (16) (Figure 2). Larger metals, for example those in the lanthanide series, favor high CNs using all eight ligand coordination points and incorporating a water molecule to give a CN of nine. The major geometries of interest are octahedral (CN = 6) and square antiprismatic (CN = 8) (15). Metals bound with octahedral geometry (CN= 6) have two carboxylic acid arms unattached, which can interact with the cryptophane cage. Hyperpolarized ^{129}Xe in the cryptophane cage is positioned close to the metal ion, and even weak interact ions between them can result in a distinct chemical shift, which depends upon the metal present. Cryptophane-A is intrinsically chiral, due to the handedness of the connection between the two cyclotriveratrylene units, and its synthesis yields an equal mix of the two enantiomers. When coupled to amino acids of pure chirality an equimolar mix of two diastereomers is created. For the current work, we used the mixture of the two, which turned out to be advantageous, because the metal-induced xenon shifts are different for each diastereomer.

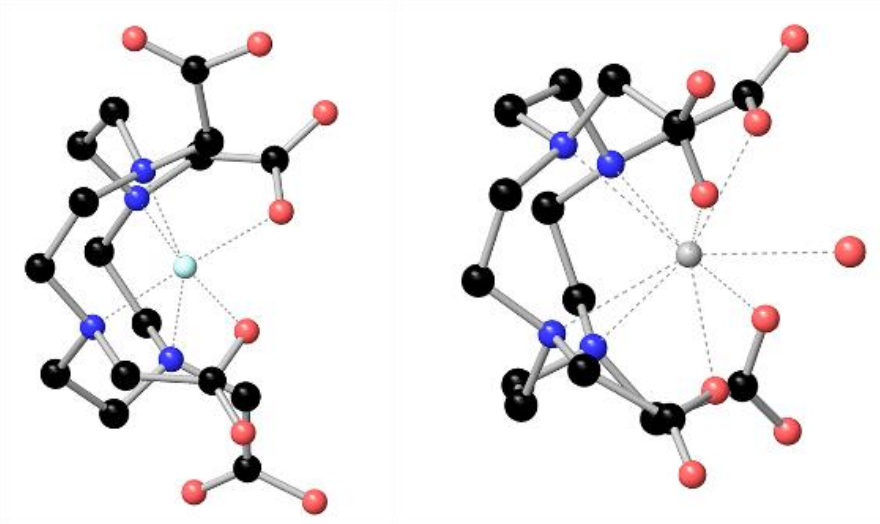

Figure 2. Crystallographically determined structures of DOTA bound to metal ions with coordination numbers of six, Ga^{2+} (left) and nine, Ce^{3+} (right).

4.3 Methods

We synthesized a water-soluble sensor minimizing the distance between DOTA and the cryptophane cage to increase the effect of metal binding on the chemical shift of xenon. The cryptophane cage is hydrophobic, and the solubility of DOTA decreases upon formation of a complex with a metal ion, so five glutamic acid residues were added to enhance solubility. The

sensor was prepared by using solid-phase synthesis methods with a Wang resin. As a small linker between the cryptophane and DOTA, we added diaminopropionic acid in the last coupling before the addition of the cryptophane. The 1,4,7,10-tetraazacyclododecane-1,4,7,10-tetraacetic acid mono-N-hydroxysuccinimide (DOTA–NHS) ester was used to attach DOTA to the primary amine of aminoproprionate in an aqueous solution. The synthesized sensor was cleaved from the resin and purified with reversed-phase high-pressure liquid chromatography (HPLC). The synthesis route and structures are summarized in Figure 3.

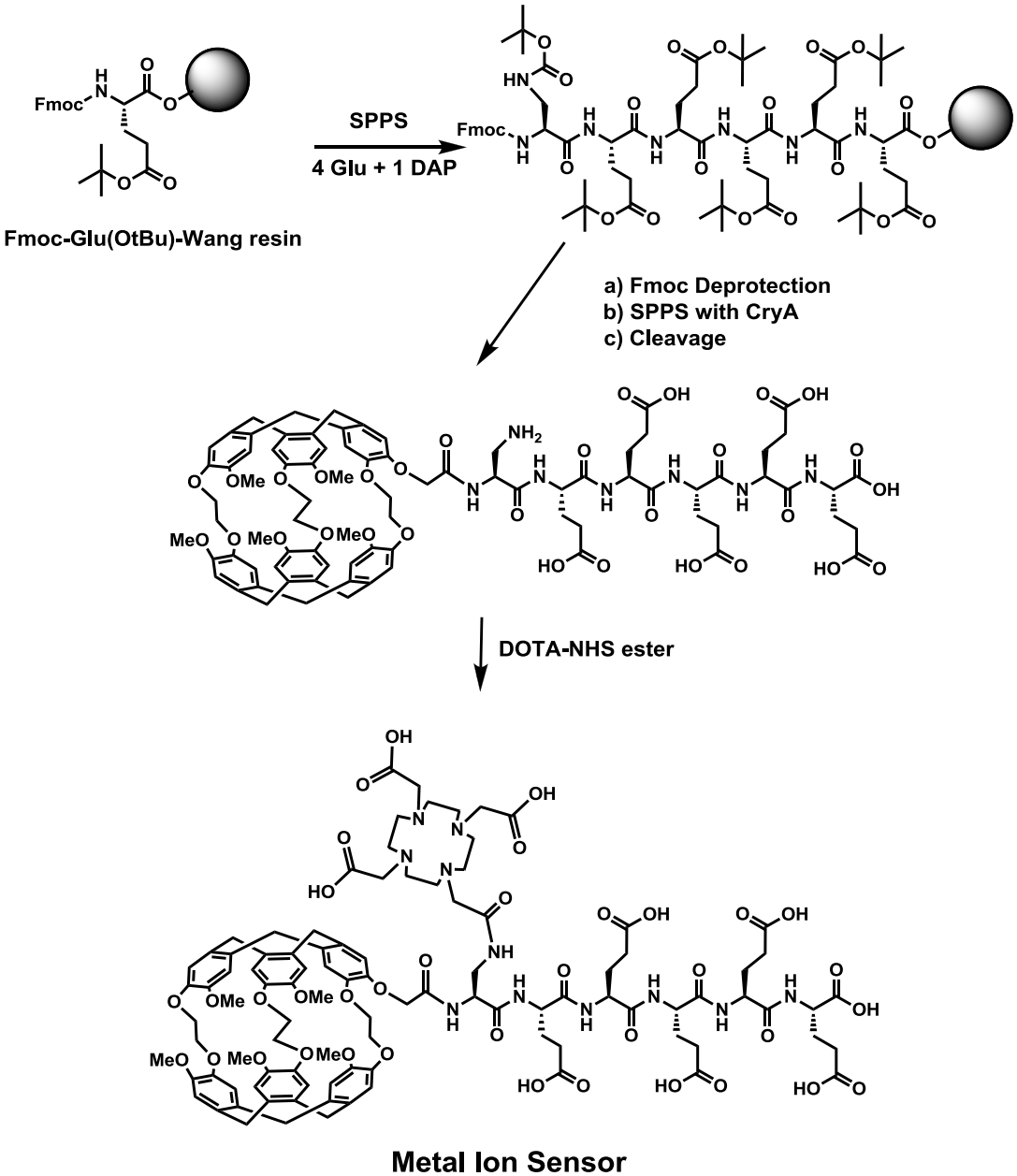

Figure 3. Synthesis of the metal-ion sensor. Five glutamic acid molecules, one diaminopropionic acid, and a cryptophane cage were attached to the Wang resin. They were then cleaved from the resin and DOTA was attached in aqueous solution. Crystallographically determined structures of DOTA bound to metal ions with coordination numbers of six, Ga^{2+} (left) and nine, Ce^{3+} (right).

The sensor was dissolved in phosphate buffer (pH 7.4) to give a solution with a concentration of 50 µM. Upon bubbling a polarized gas mixture containing ^{129}Xe (2% natural isotopic abundance Xe, 10% N_2, 88% He) into the solution, the two distinct peaks corresponding to the diastereomers of the structure were seen, as observed in previous work on diastereomeric sensors (7). Experiments were performed by adding a particular metal ion to a sensor solution in a 1:1 molar ratio. The solutions were then bubbled with the polarized gas mixture, and the dissolved ^{129}Xe NMR spectra were measured on a 9.4 T Varian NMR spectrometer (17). As the chemical shift of ^{129}Xe is sensitive to temperature and pH (18), all spectra were obtained under the same conditions (pH 7.4, 20±0.1 °C). Each chemical shift was referenced to the dissolved ^{129}Xe signal (12).

4.4 Results and discussion

Changes in the chemical shift of xenon were determined upon the binding of the different metal ions, for example Cd^{2+} and Cu^{2+} (Figure 4). The induced changes in shift for a larger range of metals are shown in graphical format in Figure 5.

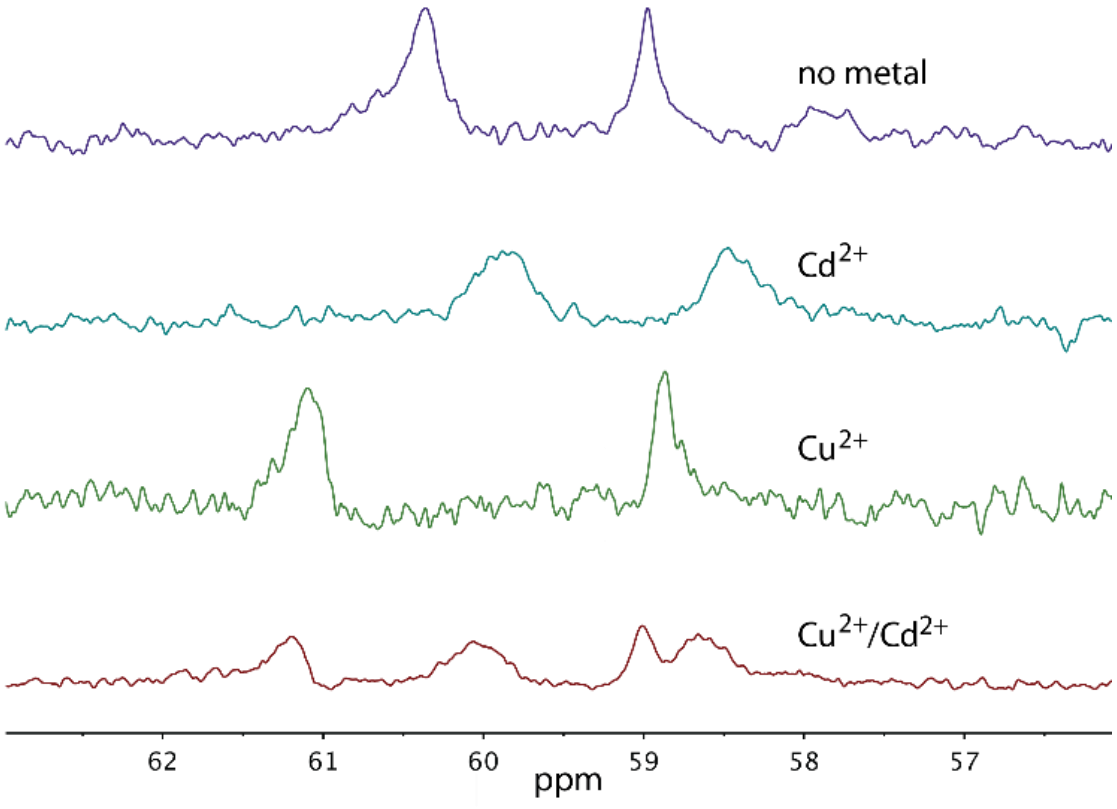

Figure 4. Comparison of ^{129}Xe spectra for 50 µM cryptophane complex with no metal, Cu^{2+}, Cd^{2+}, and a 50:50 mix of Cd^{2+} and Cu^{2+}at 25 µM.

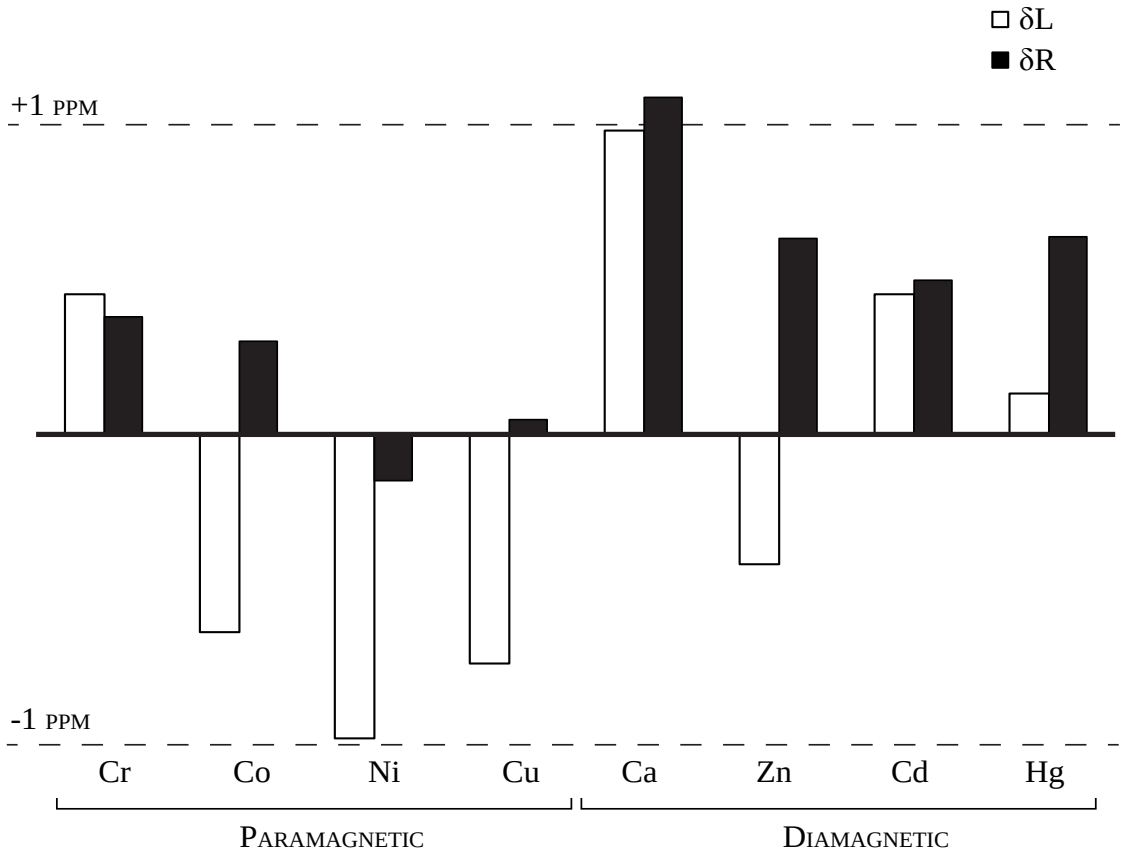

Figure 5. Comparison of the metal-induced xenon shift changes upon changing from the free sensor to the metal-bound sensor for each diastereomer. Metals are arranged from lowest to highest atomic number within each subset.

It is interesting to note that the metal-induced shift changes are different for the two diastereomers and distinct for each metal ion. These differences in shift are presumably associated with the way the peptide chain and DOTA moiety interact with the cryptophane cage through transient contacts. All of the ions featured in Figure 5 have a 2+ charge. There is no systematic pattern of change with atomic number or a consistent difference between paramagnetic and diamagnetic metals. The direction of the shift was most consistent for the diastereomers for which the free ligand is upfield of the bound ligand. The glutamate that resides in the solubilizing peptide can potentially interact with metals, so we also studied the cryptophane– peptide construct without the DOTA-chelating agent.

The cryptophane cage with five glutamic acids attached was mixed with the same metal ions, but no ^{129}Xe NMR shifts were observed, thus supporting our view that the DOTA-bound metals induce the shift in the sensor and not the glutamate residues in the peptide. The distance between the bound metal and the xenon atom is large enough that paramagnetic relaxation does not dominate the xenon linewidth even with strongly relaxing metal ions, such as Ni^{2+}.

The first-row transition metals, Cr, Co, Ni, Cu, and Zn, form hexadentate complexes (CN=6) with DOTA (all have an ionic radius between 0.69 and 0.74 Å). Metals with larger ionic radii, that is, Ca, Cd, and Hg (0.97–1.1 Å), form octadentate structures (CN=8) with DOTA (15). Both diastereomers tend to have more upfield shifts within the CN=8 complexes than the CN = 6 metals. Chemical-shift studies of even larger metals yielded multiple peaks as shown in Figure 6 for the sensor bound to Ce^{3+}.

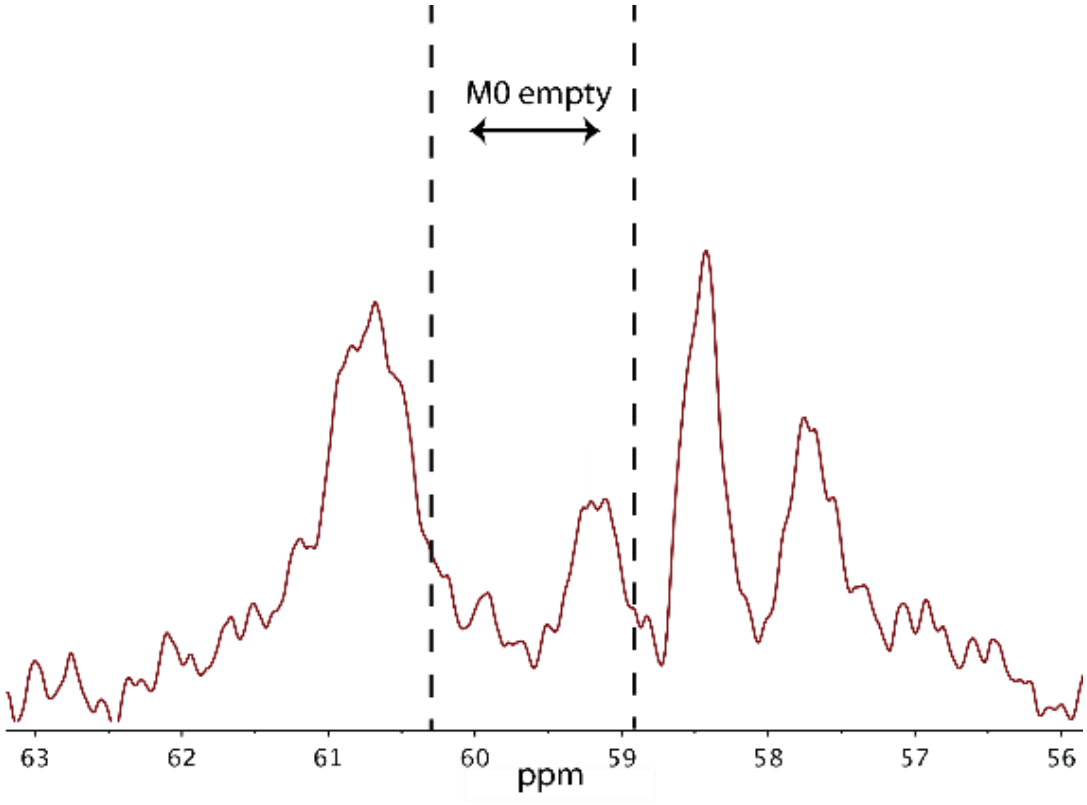

Figure 6. The ^{129}Xe spectrum of the cerium-bound sensor (CN = 9) shows four peaks versus two for the other metals, due to the two helical structures that the DOTA acetate arms form around the lanthanides. These two isomers are in slow exchange with each other giving rise to distinct peaks that are observable by using the sensor.

Previous ^{1}H NMR studies of lanthanides bound to DOTA revealed a similar phenomenon where a slow exchange between different isomers of a capped square antiprismatic geometry (CN=9) resulted in multiple peaks (19). These two isomers represent the two helical structures that the acetate arms of the DOTA complex can take when bound to a metal ion, with an H_2O molecule acting as a cap on the complex. It has been previously shown that xenon detects differences in chirality (7); here this sensitivity can be exploited to observe the difference between isomeric pairs of metal complexes with the same coordination number.

The changes in chemical shift are modest for all metal ions (≤1 ppm), but they are much larger than the observed linewidths making it possible to identify peaks for multiple metals in a single sample (Figure 4). Titrations of the sensor, starting with no metal ions and increasing to a 1:1 ratio with Fe^{3+} in increments of one quarter of the total concentration of M0, show resonances for the free and metal-bound forms in slow exchange (as expected from the high affinity of

DOTA for all of the metals studied). The relative sizes of the resonances show that the intensities reflect the stoichiometry allowing for their potential use in the quantitative determination of metal-ion concentrations (Figure 7).

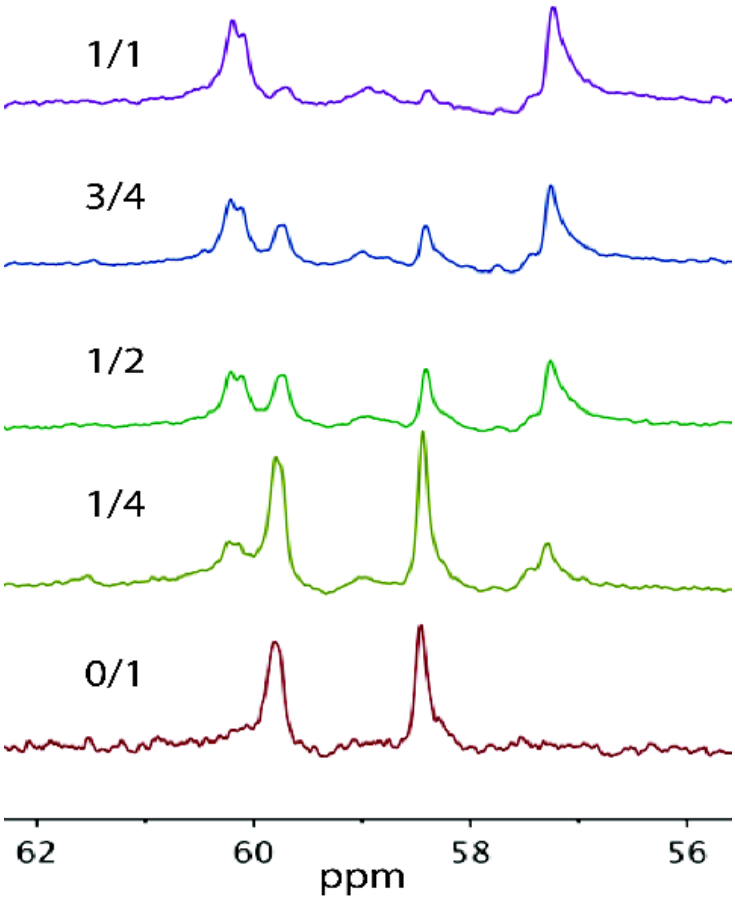

Figure 7. A series of spectra for the titration of Fe^{3+} into the sensor solution shows the simultaneous detection of the metal-bound and unbound sensor. The estimated ion-to-sensor ratio is shown alongside each spectrum, with 1/1 corresponding to approximately 95% bound.

At 1:1 we have an equimolar ratio of Fe^{3+} to M0, which appears to correspond to less 100% bound due to a systematic error in the addition of Fe^{3+} to the sample. The variability of the metal-induced shifts indicates the challenge to optimize xenon-based metal-ion sensors to give maximal shift differences for distinct metals for the analysis of mixtures. Simulations performed by the Jameson group predict that the chemical shifts of a cryptophane-bound xenon atom are a function of the average distance from the methoxy groups on the surface of the cage, and hence, that shifts vary when contact causes a change in the shape of the cryptophane structure (20). The high polarizability of xenon makes it very sensitive to its immediate environment, thus, very small changes owing to transient contacts can be detected. The binding of metal ions to the attached DOTA moiety causes distinct shifts for each diastereomer, which indicates that different interactions of the peptide/DOTA segment with the cage occur in the two diastereomers. A more complete understanding of the details may allow further optimization of the sensor for maximal response and its utility in metal analysis.

4.5 Conclusion

The signal-to-noise ratio in these experiments depends on the degree of polarization of the xenon and the fraction of ^{129}Xe in the gas. Increasing either of these would improve our ability to resolve the chemical-shift differences. Our experiments were performed with approximately 2% polarization of the natural isotope distribution of 26% ^{129}Xe. Using isotopically-enriched xenon and increasing the polarization would greatly increase the observed signal-to-noise ratio. Continuous-flow polarizers generating >60% polarization have been described (21), and near-unity polarization has been achieved in batch processing polarizers (22). In addition, the use of chemical exchange saturation transfer (CEST) (10) would provide further significant enhancement of the sensitivity. To maintain the resolution, optimization of the saturation power to avoid ″power broadening″ will be needed. Applying these approaches should make it possible to detect metal complexes in the low nanomolar concentration range. The ability to detect metals at low concentrations in the presence of more abundant ones will be determined by the separation between the xenon resonances of the particular species of interest. It has been shown that hyperpolarized xenon can be combined with MRI, and this combination makes it possible to image the spatial distribution of metals in a sample (23).

4.6 Acknowledgements

This work was supported by the U.S. Department of Energy, Office of Science, Basic Energy Sciences, Materials Sciences, and Engineering Division, under Contract No. DE-AC02-05CH11231. K.J. acknowledges a fellowship from the Republic of Korea Army. C.C.S. acknowledges a graduate fellowship through the National Science Foundation.

4.7 Supporting Information

General experimental procedures and materials.

Unless otherwise noted, all chemicals and solvents were of analytical grade and used as received from commercial sources. Water (dd-H_2O) used in biological procedures or as the reaction solvent was deionized using a NANOpure purification system (Barnstead, USA). Phosphate buffer was purchased from Sigma Aldrich, and was free of metal ions. ESI high resolution mass spectra were obtained in the QB3 Mass Spectrometry Facility at UC Berkeley using an LTQ orbitrap XL hybrid mass spectrometer.

Synthesis of Metal ion sensor

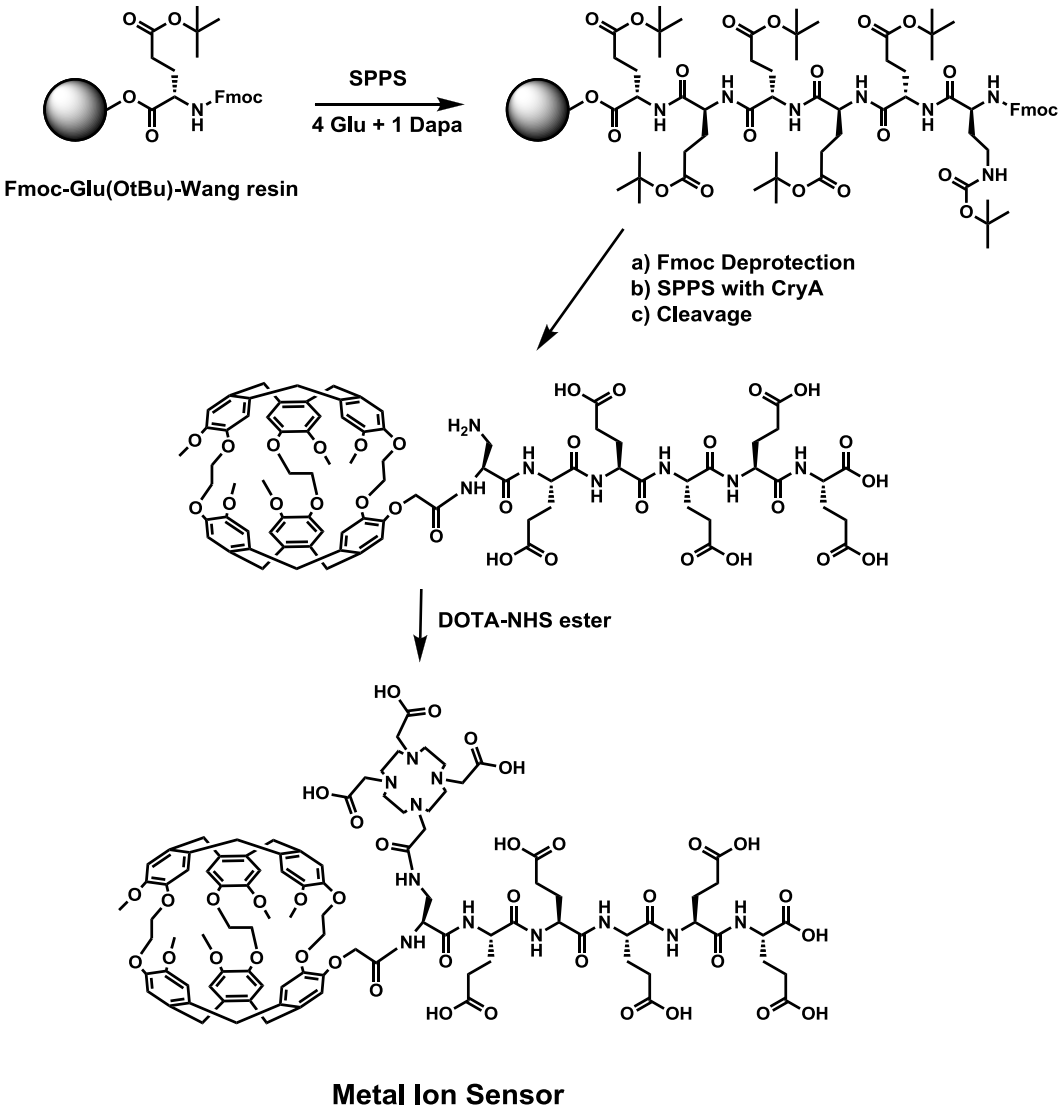

Figure S1. Solid phas synthesis of the Metal Ion Sensor

Fmoc glutamic acid Wang resin was used for solid phase peptide synthesis. After deprotecting fmoc with 20% piperidine (30 min., room temperature), fmoc glutamic acid (5 equiv.) was added with HBTU (5 equiv.) and HOBT (5 equiv.) in DMF (dimethyl formamide) for 5 hours. The completeness of reaction was checked with the Kaiser test. Three additional glutamic acids were attached on the resin in this way. Fmoc-diaminopropionic acid was attached using the same method. After cleaving fmoc, a 2 fold excess of cryptophane cage acid (supplied by Kang Zhao, Tianjin University in China) was attached with the same activating compounds, coupled for 24 hours, followed by cleavage using TFA : water : triisopropylsilane (95:2.5:2.5) for 3 hours. A white salt resulted after two precipitations with diethyl ether. The solid was dissolved in water with addition of sodium hydroxide until dissolution was complete. A two fold excess of DOTA-NHS ester (Macrocycles Company) in water was added, with more sodium hydroxide solution until all of the DOTA-NHS ester was dissolved. The reaction mixture was held at room

temperature overnight and then the metal ion sensor was purified by reverse phase HPLC (~1 mg). ESI-HRMS ($C_{100}H_{119}N_{11}O_{37}$+3$Na^+$+$K^+$) was done to verify the identity, the mass calculated was 2173.7077 and experimental was 2173.5882.

Analyzing Metal ion sensor by ^{129}Xe NMR

Each sensor sample in solution was prepared by adding 1 equivalent of the metal ion under study. Spin-exchange optical pumping hyperpolarization was used for a gas mixture with 2% ^{129}Xe, 10% N_2, 88% He. After polarization, the gas mixture was routed directly to a 5 mm NMR tube. ^{129}Xe was dissolved into the solution via bubbling through a capillary running down to the bottom of the NMR tube, with gas flowing at a rate of 0.2 SLM for 10 seconds. The inlet gas pressure was maintained at 35 psi. The bubbling period was followed by 1 sec wait period to allow bubbles to settle out. All ^{129}Xe NMR data were acquired with a 400 MHz (9.4 T) Varian VNMRS console. Spectra were acquired with 50 kHz spectral width in 0.5 second.

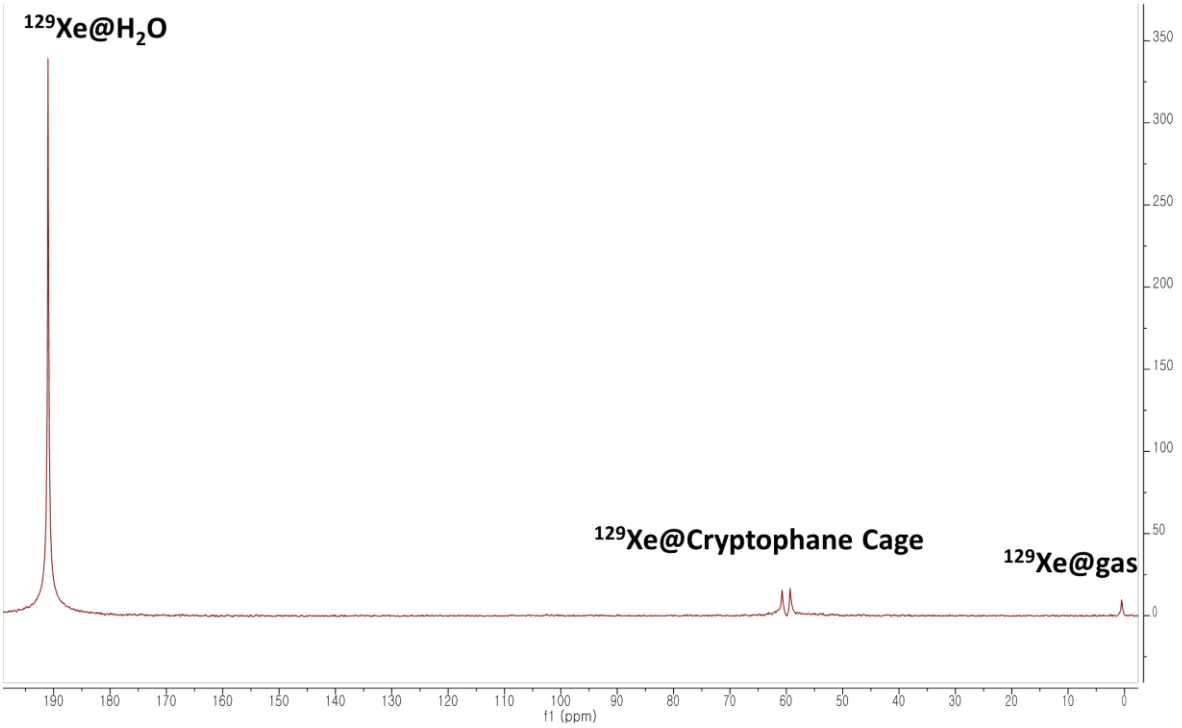

Figure S2. Hyperpolarized ^{129}Xe spectrum of metal free sensor. The ^{129}Xe chemical shift was referenced to the ^{129}Xe in solution signal.

Analyzing Other Metal ions by ^{129}Xe NMR

DOTA can also make stable complexes with lanthanide ions and other heavy metal ions and its hyperfine interaction, including pseudocontact shift, might result in enhanced chemical shifts. We tested our construct with many other heavy metal ions with the same concentrations and conditions (except averaging time) and some complexes were observed with additional shifts. However some spectra contained multiple peaks, which means the complexes with DOTA have various structural isomers, with slow exchange among them. The relaxation by lanthanides is

substantial, and hence we needed to use more signal averaging to obtain spectra of their complexes.

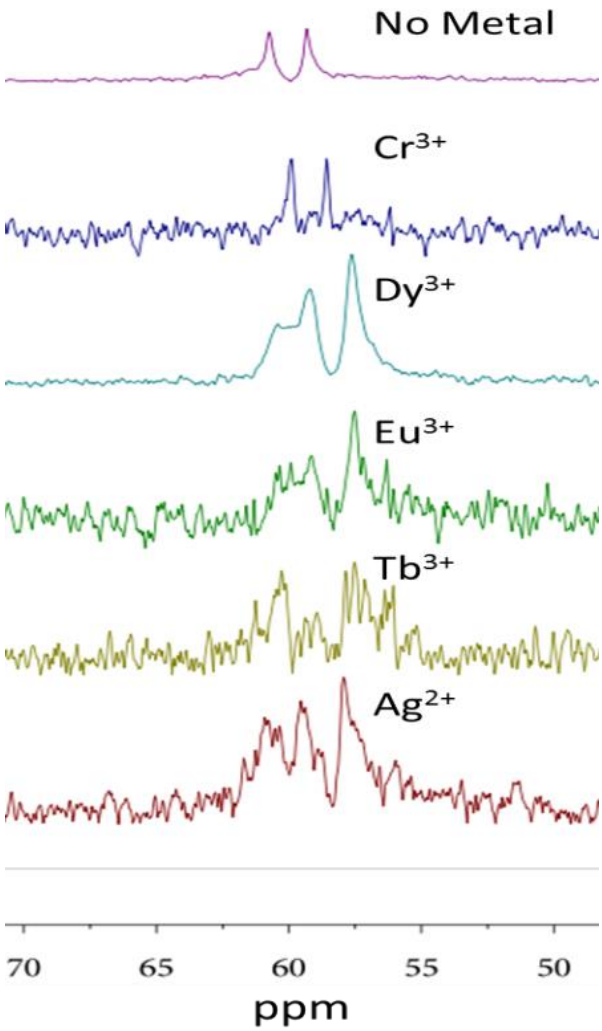

Figure S3. Hyperpolarized ^{129}Xe@Cryptophane cage spectra in complexes with various metals. The presence of multiple peaks, and broadening are apparent.

Chapter 5

^{129}Xe-CEST NMR/MRI Biosensor Targeting Folate Receptor

5.1 Abstract

A new structure for a ^{129}Xe CEST NMR/MRI biosensor targetting overexpressed folate receptors on HeLa cells was synthesized. The binding of this folate-conjugated biosensor on the HeLa cell was confirmed by confocal laser scanning microscopy and flow cytometry. A series of ^{129}Xe hyper-CEST NMR and MRI expeirments with the biosensor was carried out, and resulting signal contrasts supported that the developed biosensor has a sufficiently high affinity for the HeLa cells to be used as a ^{129}Xe MRI contrast agent for early detection of cancer.

5.2 Introduction

The noninvasive interrogation property of NMR and MRI provides excellent performance in medical imaging and research. This well-established technique is mainly based on signals generated by protons in the sample such as a body (i.e. from H_2O on fat). Given the characteristically low sensitivity of the technique, the protons must be abundant for a high-quality signal. To overcome this sensitivity problem for less-concentrated species, molecular sensors with various detection techniques to enhance signal intensity have been widely developed and studied (1-7). ^{129}Xe, which is the only xenon isotope with a half spin angular momentum quantum number, which gives it a high hyperpolarization, is an ideal reporter since it is inert, nontoxic, and has no background signal in natural *in vivo* materials (3, 8). Hyperpolarized ^{129}Xe, which is polarized by hyperfine interaction with hyperpolarized electrons, has been widely used as a promising imaging agent in imaging lung tissues (9-11), brains (12, 13), and kidneys (14).

Cryptophane-A (CryA) is a host for xenon and it is the core structure for use as chemical sensors in part because it induces a large chemical shift change for ^{129}Xe. Biosensors based on chemical shift have been applied in investigating the biotin-streptavidin interaction (15-17), enzyme cleavage (2), DNA hybridization (18), enzyme-ligand interaction (19), protein-protein interactions (20), and cell-specific sensors (21, 22). Indirect detection with chemical exchange saturation transfer (CEST) using CryA and hyperpolarized xenon (hyper-CEST) increased the sensitivity of CrypA-based xenon sensor by more than 1,000 fold (23). Therefore, hyper-CEST NMR/MRI imaging is a promising technique for detecting target molecules, especially for cancer cells, which requires early stage detection for the complete cure (24). Recently, the Schröder group's antibody-based biosensor was detected at lower than 20 nM by using the CryA hyper-CEST method (25).

Folic acid is well-known cancer cell-targeting ligand because it has a high affinity (K_D = approximatley 10 nM) to folate receptor (FR) which is overexpressed on the surface of many types of cancer cells (26-30). Folate-mediated active targetting has been used to increase accumulation of drug in tumors in drug delivery research. Diagnostic development, e.g. having the ability to screen patients for FR-positive cancers, is valuable for providing for treatment. There have been some methods identified such as tissue-based immunohistochemical assay or radiodiagnostic approach using 99mTC-EC20 (31). Along with those, hyper-CEST may be another powerful *in vitro* and *in vivo* diagnostic methods because a hyperpolarized ^{129}Xe MRI has already been used in hospitals and studied extensively. To demonstrate its possibility, we chose human adenocarcinoma HeLa cells as the model cancer cell line because thdy have a high level of folate receptor expression on the cell surface (32).

5.3 Methods and Experiments

Synthesis. Synthesis with a foliate moiety is quite challenging due to solubility problems. Along with our endeavor, Dmochowski's group has recently successfully synthesized a cryptophane-folate biosensor that was functionalized with a folate moiety, solubilizing peptide and the fluorophore. They confirmed the Xe binding to the cryptophane cage of the biosensor and binding to the KB cancer cell surface (30). Our study is focused on a new biosensor structure with a lower molecular weight and its application to advanced NMR/MRI studies. We designed smaller cryptophane-folate biosensors (**V1** and **V2**) with 5 glutamic acids, a cryptophane cage, folate, and 5-carboxyfluorescein (**V1** is without fluorescein, for which the structure is shown in Supporting Information, and **V2** is with fluorescein). Mainly, the synthesis was carried out employing the standard solid phase peptide synthesis. Because of the low CryA and folate solubility, we introduced 5 glutamic acids, which hold negative charges at the neutral pH, preventing random cell uptake of biosensor. In order to add CryA selectively on the lysine residue, we attached 4-methyltrityl (Mtt) protected Fmoc-lysine at the N-terminus. Relatively mild acidic conditions were used to detach only Mtt, and the presence of the free primary amine of lysine residue was checked with Kaiser test. After CryA acid was coupled to the lysine residue using the HCTU (1H-Benzotriazolium 1-[bis(dimethylamino)methylene] -5chloro-,hexafluorophosphate (1-),3-oxide) amide coupling reaction, commerically available Fmoc-lysine derivatized with 5-carboxyfluorescein was coupled. After detaching the Fmoc protecting group, we added active folic acid NHS ester (33). In the case of **V1**, we omitted the addition of the 5-carboxyfluorescein group. The cleavage at the synthesized biosensor from polystyrene resine was done in strong acidic conditions and the product was purified by HPLC. (See the Supporting Information for more detailed procedures and structures.)

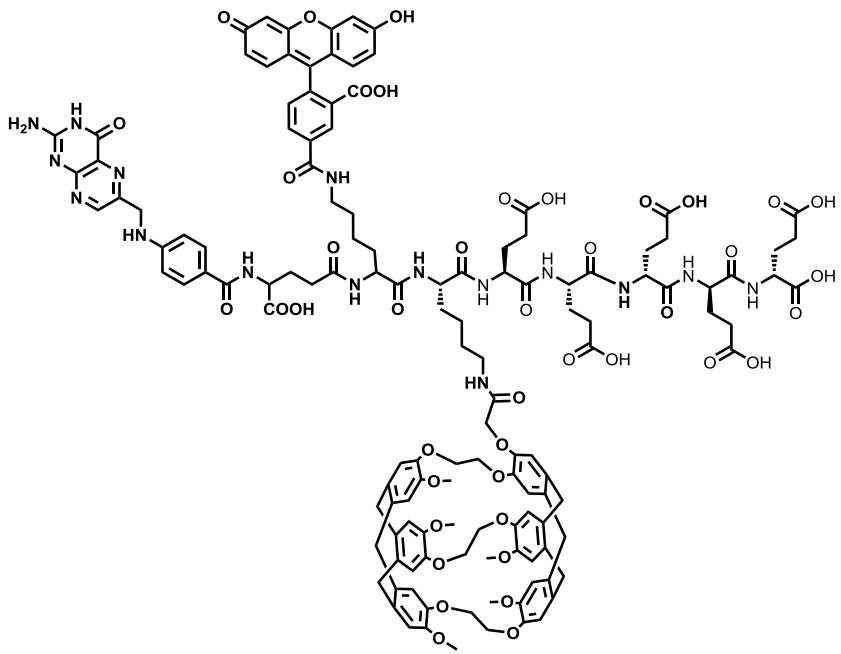

Figure 1. Structure of synthesized biosensor (**V2**). Overall systhesis was carried out by solid phase methods. (Detailed synthesis scheme is described in Supplementary Figure S1) Five Glutamic acids were attached to improve solubility in the neutral buffer. CryA, the binding moiety for Xe, is attached to a lysine residue. Folate, the targeting ligand for FR, was added on the N-terminal of the lysine followed by the 5-carboxyfluorescein-conjugated lysine.

Confocal laser scanning microscope observation. Human cervical cancer cells (HeLa cells) were cultured in folate-free RPMI (Life Technologies) containing 10% fetal bovine serum (Life Technologies) and 1% penicillin streptomycin (termed RPMI/FBS) for two weeks. Then, HeLa cells (50,000 cells) were seeded in a 35-mm round culture dish in RPMI/FBS and incubuted for one day. The old RPMI/FBS was exchanged with fresh RPMI/FBS (1.9 mL) containing 100 μM biosensor **V2** (100 μL) and further incubated for 5 and 24 h at 37°C. The RPMI/FBS was then removed and the fresh RPMI/FBS containing Hoechst 33342 (Thermofisher Scientific) was incubated for 10 min. The HeLa cells were observed by using a Carl Zeiss LSM710 microscope at the Biological Imaging Facility at UC Berkeley.

Flow cytometry measurement. HeLa cells were cultured in folate-free RPMI/FBS for two weeks. Then, HeLa cells were seeded in a 24-well plate (200,000 cells/well) in RPMI/FBS. The old RPMI/FBS was exchanged with fresh RPMI/FBS (400 μL) and incubated with 100 μM biosensor **V2** (100 μL) for 2 h in the dark in 37°C. Then the cells were washed twice with 0.5 mL of PBS, treated with a trypsin-EDTA solution, and suspended in 0.5 mL of PBS. The amount of **V2** was measured by using a flow cytometer (BD LSR II, BD Biosciences). For the negative control sample of the flow cytometry experiment, after exchanging with fresh RPMI/FBS (400 μL), folic acid (Sigma-Aldrich) was dissolved in DMSO at the concentration of 10 mM and diluted to 10 μM with PBS. 10 μM folic acid solution (100 μL) and the HeLa cells were preincubated at 37 °C for 5 h and RPMI was exchanged and then incubated with the biosensor with the same procedure as the positive sample.

NMR / MRI experiment

Cells with V2 preparation Negative control sample : Human cervical cancer cells (HeLa cells) were cultured in folate-free RPMI (Life Technologies) containing 10% fetal bovine serum (Life Technologies) and 1% penicillin streptomycin (RPMI/FBS) for two weeks. Then, folic acid (Sigma-Aldrich) was dissolved in DMSO at a concentration of 10 mM and diluted to 10 μM in PBS. The old RPMI was exchanged with fresh RPMI/FBS (400 μL) and 10 μM folic acid solution (100 μL) and the HeLa cells were incubated at 37 °C for 5 h. The cells were washed twice with 0.5 mL of PBS and incubated with RPMI/FBS (400 μL) and 100 μM biosensor (**V2**) (100 μL) for another 2 h in the dark in 37 °C. Then, the sample was treated with a trypsin-EDTA solution, and suspended in 1 mL of PBS. The cells were pelleted by centrifugation (400 × g for 4 min at 25 °C) and washed three times with ice-cold DPBS containing 1% FBS. The pelleted cells were resuspended in 500 μL NMR media (RPMR/FBS with 0.002% L-81, ∼20 million cells/mL). A small sample was taken for cell counting and viability analysis with Trypan Blue 0.5% (Biochrom AG) using a TC20 Automated Cell Counter (Bio-Rad). All cells used in further experiments has >95% viability as assessed by Trypan Blue analysis.

Positive sample : Human cervical cancer cells (HeLa cells) were cultured in folate-free RPMI (Life Technologies) containing 10% fetal bovine serum (Life Technologies) and 1% penicillin streptomycin (RPMI/FBS) for two weeks. Cells were washed and incubated with RPMI/FBS (400 μL) and 100 μM biosensor (**V2**) (100 μL) for 2 h in dark in 37 °C. The sample was then treated with a trypsin-EDTA solution, and suspended in 1 mL of PBS. The cells were pelleted by centrifugation (400 × g for 4 min at 25 °C) and washed three times with ice-cold DPBS containing 1% FBS. The pelleted cells were resuspended in 500 μL NMR media (RPMR/FBS with 0.002% L-81, ∼20 million cells/mL). A small sample was taken for cell counting and viability analysis with Trypan Blue 0.5% (Biochrom AG) using a TC20 Automated Cell Counter (Bio-Rad). All cells used in further experiments has >95% viability as assessed by Trypan Blue analysis.

Hyperpolarized ^{129}Xe NMR/MRI. A gas mixture (2% ^{129}Xe natural abundance, 10% N_2, 88% He) was hyperpolarized via SEOP (spin-exchange optical pumping) using a homebuilt polarizer. The polarized gas was routed directly to a 5 mm NMR sample tube. Hyperpolarized ^{129}Xe was dissolved into the sample solution via bubbling through a capillary running down to the bottom of the NMR tube at a rate of 0.2 SLM for 20 s. Total gas pressure was maintained at 2.38 atm. The bubbling period was followed by a 4 s wait period to allow the solution to settle. The dSNOB pulses (3) with 500 Hz bandwidth were used for saturation with the same pulse sequence which was used previously, except the saturation time was 8 seconds (4). All ^{129}Xe NMR data were acquired on a 400 MHz (9.4 T) Varian VNMRS console. The spectra were acquired with a 30.5 kHz spectral width in 1 s. ^{129}Xe NMR was carried out with two prepared cell samples. The saturation profile of each sample was measured by integrating the recorded Xe@water signal as a function of the RF pulse frequency. Contrasts with different saturation times were measured with saturation on and off resonaces (5,700 Hz and 33,700 Hz) four times for 3, 6, 9, 12 seconds.

For ^{129}Xe hyper-CEST saturation MRI, we used a modified fast spin echo imaging sequence that included bubbling and waiting times as well as a saturation pulse prior to excitation (34). The

total gas pressure was maintained at 2.38 atm and flow rate was 0.2 SLM. The solution was typically bubbled for 20 s followed by a 4 s wait. dSNOB pulse was 6.5 μs, a train of 4 echoes was used with an echo time of 10 ms and the overall repetition time (TR) was 22.5 s. The signals were acquired with a 12.02 kHz spectral width and 2.66 ms acquisition time. All images were acquired in the axial orientation, and averaged 16 times, with a field of view of 20 mm by 20 mm. The Xe images had a k-space matrix of dimensions 32 readout by 32 phase encode points. The ^{129}Xe contrast map was obtained by subtracting the k-space of off-resonance from the on-resonance saturation images voxel-by-voxel using custom MATLAB scripts, after apodization of the signal using a 10 Hz exponential function and Fourier transformation. The difference image was then normalized by dividing it by the off-saturation image. The ^{129}Xe contrast maps were confined to the regions of interest defined by the proton image. Because of signal inhomogeneity stemmed from inhomogeneous cell mixtures, the final ^{129}Xe contrast maps were averaged in the confined region.

5.4 Results and discussion

We successfully synthesized two biosensors, **V1** and **V2**. Because we designed bulky structures with different solubilities, we synthesized **V1** first. After confirming its synthesized structure, we carried out the synthesis of the fluorescein-containing **V2** biosensor, which was needed for affinity tracking and the NMR/MRI experiment. The fluorescein in **V2** can be used for determining the affinity on the cancer cells before applying in NMR/MRI systems. The **V2** biosensor was observed to bind to the HeLa cells by using fluorescence spectroscopy, confocal laser scanning microscopy (CLSM) and flow cytometry (Figure 2). We observed fluorecence signals along the surface of the Hela cells after 5 h incubations, probably indicating that the folate in **V2** biosensor binds to folate receptor as expected. The HeLa cells from the 24 h incubation time showed **V2** biosensors were located in the cytosol (Figure 2a). Based on the CLSM observation, we prepared flow cytometry and NMR/MRI samples in the same condition for comparision. In the flow cytometry experiment, the HeLa cells were incubated in advance with an excess amount of folic acid (negative control sample) to saturate folate receptor before the adding the **V2** biosensor (Figure 2b). The cellular internalization in the negative control was minimal, and a similar level as the un-treated samples, indicating that the main internalization mechanism of the **V2** biosensor is receptor-ligand interactions (Figure 2b).

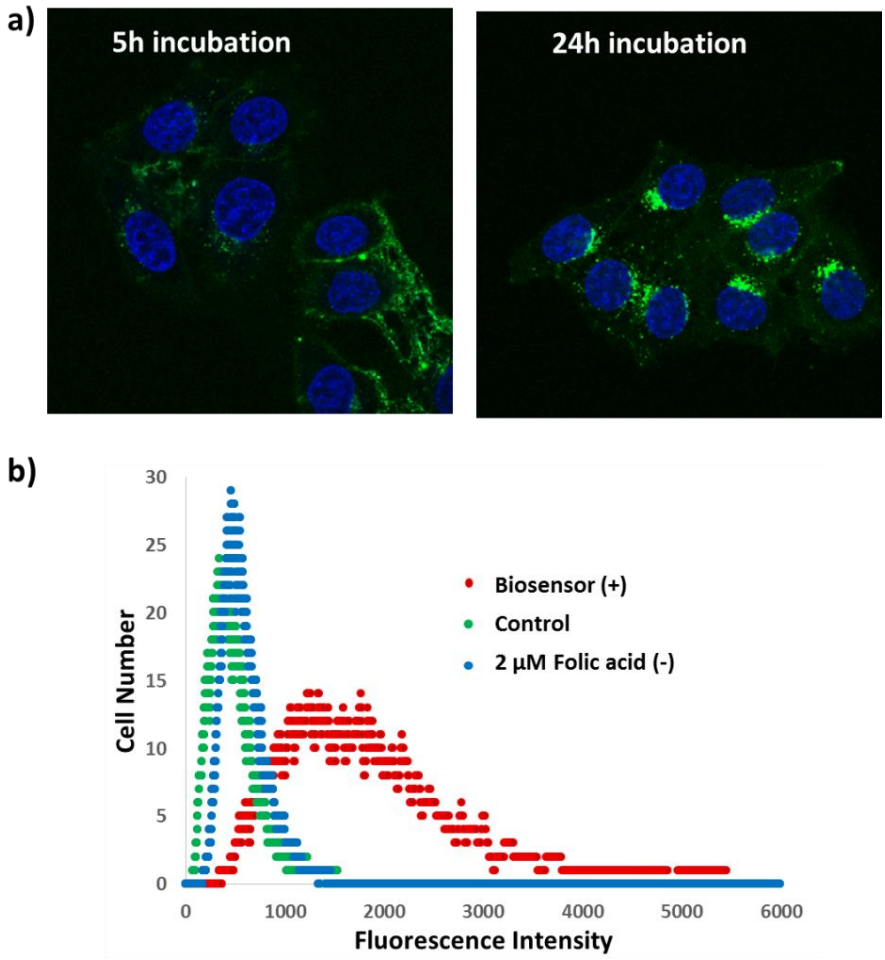

Figure 2. Cell binding analysis of the biosensor. a) Cultured HeLa cells in folate-free media were incubated with 20 µM of fluorescently labeled biosensor for 5 h and 24 h at 37 ℃, respectively. **V2** biosensor and nucleus are shown in green and blue, respectively. b) Flow cytometry analysis showing that the biosensor **V2** was specifically bound on the cell surface. HeLa cells in folate-free media were incubated with 20 µM fluorescently-labeled biosensors for 2 h at 37 ℃, followed by washing out unbound sensor. The negative control cell sample was prepared by pre-incubating with 2 µM of folic acid for 5 h at 37 ℃ followed by the addition of the biosensors using the same procedure as for the positive samples.

We obtained the Hyper-CEST ^{129}Xe z-spectra using two samples prepared in the same conditions as for flow cytometry (Figure 3a), and the results showed a high contrast in the Hyper-CEST experiment (Figure 3b). A small contrast signal from the negative control sample might be from natural metabolism such as homocysteine, which was also shown in the flow cytometry experiement. To increasae the contrast between positive and negative control experiments, we performed a saturation on-off experiment with different saturation times. The resulting data showed an increased contrast with a longer saturation time, which confirmed the binding of biosensors (Figure 3c). We collected ^{129}Xe Hyper-CEST contrast MRI images with different saturation time points using live HeLa cells. Numerical averaging over the whole phantum area was done and color-mapped. The contrast map using longer saturation times

shows a higher contrast. There was a low contrast signal from the negative control sample with a long saturation time (12 sec), which is well explained by flow cytometry result, small contrast signals from z-pectra and saturation on-off data (Figure 3d).

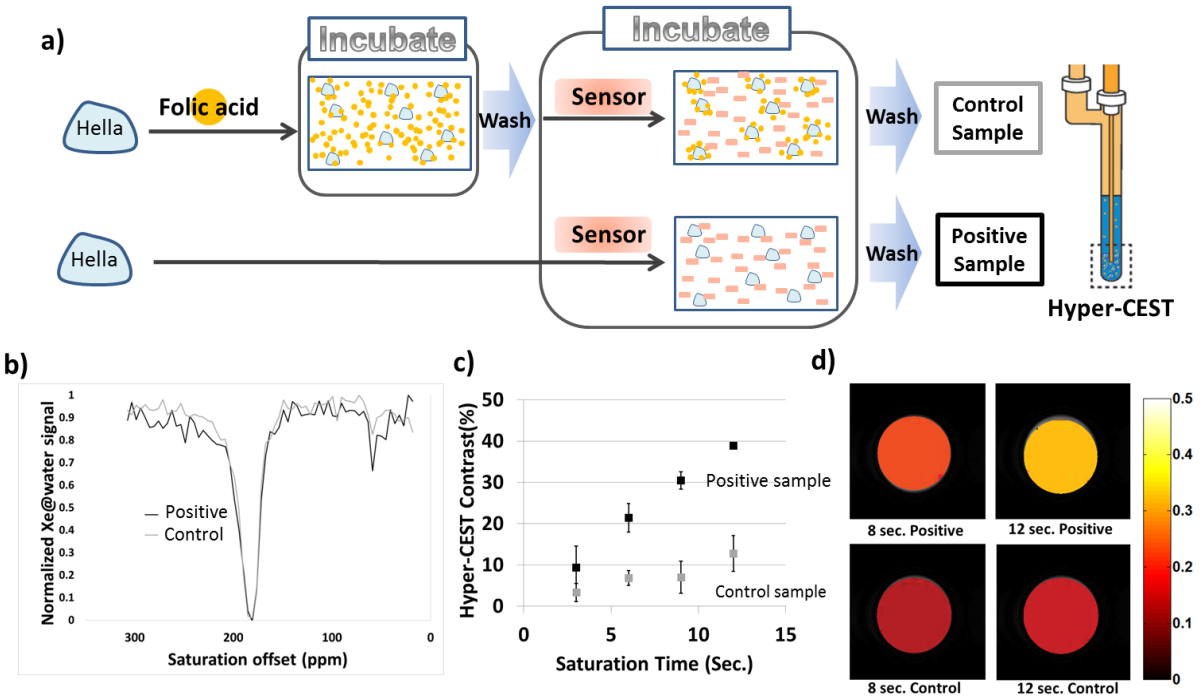

Figure 3. NMR / MRI experiments with cell solution samples. a) 100 million HeLa cells in folate-free media were incubated with 2 µM folic acid for 5 h at 37 ℃, then washed to remove unbound folic acid. Next, 20 µM concentration of the biosensor **V2** was added and incubated for additional 2h at 37 ℃ to prepare for the control sample. Positive control was prepared with the same procedure except preincubation with folic acid. b) Zspectra were obtained by flowing hyperpolarized Xenon gas into the solution containing the cells. c) The difference in the hyper-CEST contrast resulting from different time points are presented. These NMR data show that the biosensor was binding to the HeLa surface. Longer saturation time produces more contrast and its contrast responses are used to image biosensor in HeLa cells. d) Saturation contrast voxel was averaged because of inhomogeneous signal stemmed from the cells (the original contrast signal is presented in Supplementary figure 2).

5.5 Conclusion

Here, we designed, synthesized, and characterized a new folate receptor-targeting ^{129}Xe hyper-CEST sensor. Its binding with folate receptors, which are overexpressed in Hela cells, was demonstrated by using flow cytometry and CLSM. A HeLa cell incubation experiment with biosensor for ^{129}Xe NMR showed a good z-spectrum contrast when cells were precultured with a high concentration of folic acid. The relatively small signal from the negative control supports the idea biosensors are competing excess folic acid. The contrast generated with this biosensor was enough to provide ^{129}Xe hyper-CEST MRI with changes in a phantom. This study demonstrates a folate receptor targeted Xe NMR/MRI biosensor for a potential early-time

cancer detection. Considering that folate receptors are highly overexpressed on lung tumor cells, and hyperpolarized ^{129}Xe MRI for lung is under developement as a powerful cancer diagnostic tool (35-37), this ^{129}Xe MRI - biosensor study might be a promising step in developing a hyperpolarized ^{129}Xe biosensor for lung cancer.

5.6 Supporting information

General information. All amino acids and HCTU (1H-Benzotriazolium 1-[bis(dimethylamino)methylene] -5chloro-,hexafluorophosphate (1-),3-oxide) were purchased from either NovaBioChem or Chem-Impex International, Inc. Fmoc-Glu(O^{t}Bu)-Wang resin (100-200 mesh) was purchased from NovoBioChem. Fmoc-Lys (5-FAM)-OH and Fmoc-Lys(Mtt)-OH were purchased from AnaSpec. All other chemicals were purchased from Sigma-Aldrich and used as received without further purification. Double-distilled water (dd-H_2O) used for buffers and reactions was deionized using a Barnstead NANOpure purification system (ThermoFisher, Waltham, MA). Semi-preparative purifications were performed on an Agilent 1100 Series HPLC Systems (Agilent Technologies, USA) with an in-line diode array detector (DAD) and in-line fluorescence detector (FLD) equiped with a Phenomenex Gemini (250x10 mm) 5 µm C-18 column. CH_3CN-H_2O (0.1% TFA) was used as eluent with a flow of 3 mL/min.

Construction of Biosensor (V1, V2)

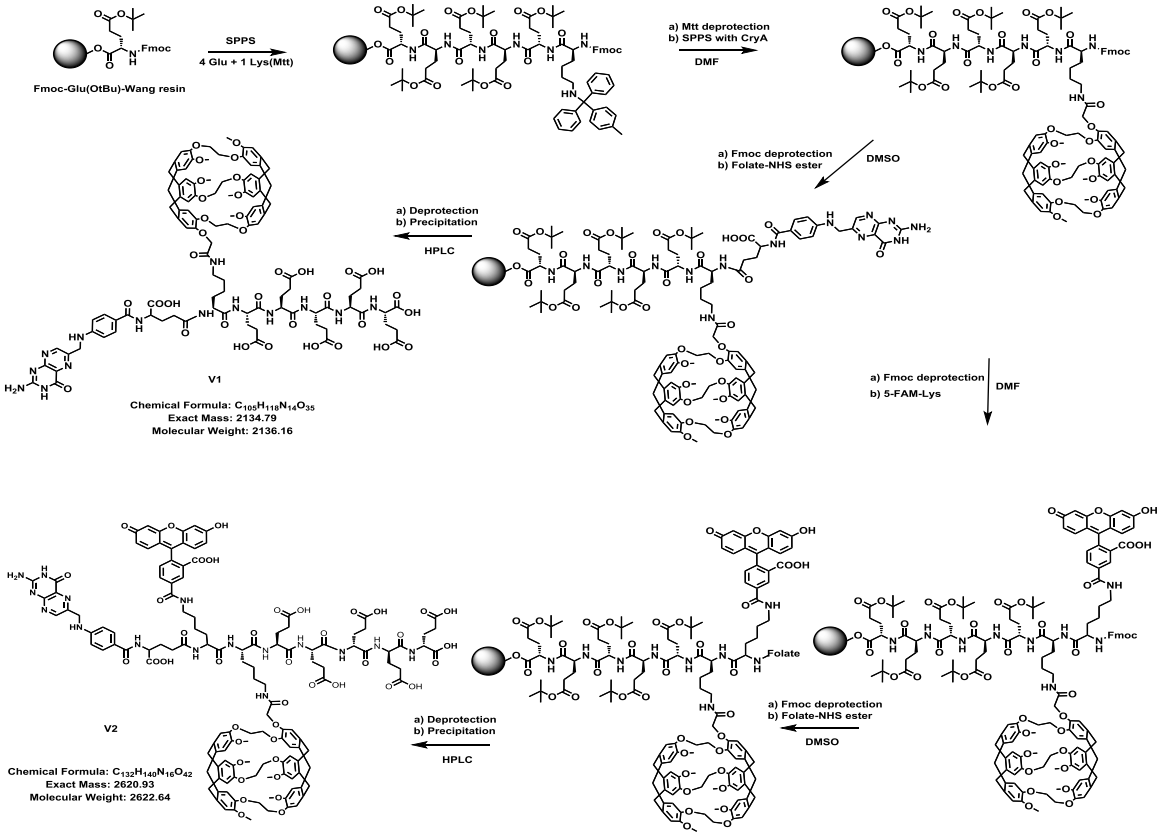

Figure S1. Schematic diagram for the **V1** and **V2** synthesis. Standard solid phase synthesis was used.

The biosensor candidates were synthesized employing standard Fmoc solid-phase peptide synthesis using Fmoc-Glu(O^tBu)-Wang resin (0.57 mmol/g), 5 equiv of amino acid, 5 equiv. HCTU, and 10 equiv. DIPEA (N,N-Diisopropylethylamine) in DMF until full conversion was observed by Kaiser test (38). The deprotection of Fmoc protecting groups was carried out by mixing and filtering with 20% (v/v) piperidine in DMF two times for 15 min. CryA cage (2 equiv) (supplied by Kang Zhao, Tianjin University in China) was coupled by HCTU (2 equiv) and DIPEA (4 equiv) for 24 h. 4-methyltrityl functional group was selectively removed by mixing and filtering with 3% TFA in DCM two times for 10 min. The full deprotection of lysine residue was checked by Kaiser test. Folate-NHS ester was synthesized according to the previous literature (39), 100 mg of fresh folic acid (0.23 mmol), 25 mg of N-hydroxyl succinimide (0.23 mmol) and 31 mg of DCC (0.15 mmol) were dissolved in DMF. The solution was mixed at room temperature overnight. For precipitating, mixed solvent (30 % acetone and 70% Et_2O, v/v) was mixed with the reacted solution and the resulting orange solid was obtained by filtration and washed with mixed solvent twice. Dried-solid, folate-NHS ester, was used for next step. For attaching folate-NHS ester, solvent was exchanged with DMSO and 5 equiv. was mixed with resin substrate at room temperature overnight. Kaiser test was used to check the primary amine's coupling to folate. Fully synthesized peptide was released from the resin by treatment with trifluoroacetic acid : water : triisopropylsilane (95:2.5:2.5) for 3 h. The TFA solution was concentrated by nitrogen flow and precipitated with Et_2O twice giving an off-white powder, which was purified on semi-prep HPLC and freeze dried giving a white solid. **V1**, ESI-MS calculated for $C_{105}H_{118}N_{14}O_{35}$ $[M+H]^+$ 2134.79 found 2132.77. **V2**, MALDI-TOF calculated for $C_{132}H_{140}N_{16}O_{42}$ $[M+H]^+$ 2621.93 found 2621.91.

Analyzing the biosensor by ^{129}Xe MRI. Purchased gas mixture (2% ^{129}Xe, 10% N_2, 88% He) was hyperpolarized via spin-exchange optical pumping (40). After polarization, the gas was routed directly to each sample in 5 mm NMR tube. ^{129}Xe was dissolved into the sample solution via bubbling through a capillary running down to the NMR tube at a rate of 0.2 SLM for 20 seconds. The total gas pressure was maintained at 2.38 atm. The bubbling period was followed by a 4 s wait period to allow the solution to settle down for obtaining higer ^{129}Xe in solution signal. Xenon images were acquired using a modified fast spin echo imaging sequence that included bubbling and waiting times as well as a saturation pulse prior to excitation. For saturation pulse, dSNOP purses with 500 Hz bandwidth was used with the same pulse sequence which was previously set up except saturation time is 1, 4, 8, 12 seconds (41). Temperature was maintained at 20±0.1 °C. All ^{129}Xe NMR data were acquired on a 110.595 MHz (9.4 T) Varian VNMRS console. dSNOB purse was 6.5 μs, The train of 4 echoes was used with an echo time of 10 ms and overall repetition time (TR) was 22.5 sec. Signals were acquired with a 12.02 kHz spectral width and 2.66 ms acquisition time. All images were acquired in the axial orientation an average of 16 times with a field of view of 20 mm by 20 mm. Xenon images had a k-space matrix of dimensions 32 readout by 32 phase encode points. ^{129}Xenon contrast map was obtained by subtracting the k-space of off-resonance from the on-resonance saturation images voxel-by-voxel using custom MATLAB scripts that apodized the signal using a 10 Hz exponential function. Afterwards, the subtracted image was normalized by dividing it by the off-saturation image (Figure S2). The intensity of final ^{129}Xenon contrast maps were reversed and then confined to regions of interest defined by the proton image (Figure S3).

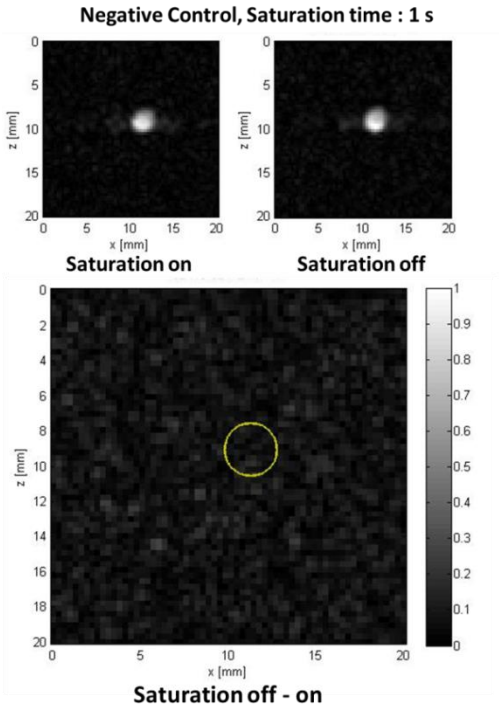
Negative Control, Saturation time : 1 s
Saturation on
Saturation off
Saturation off - on
z [mm]
x [mm]

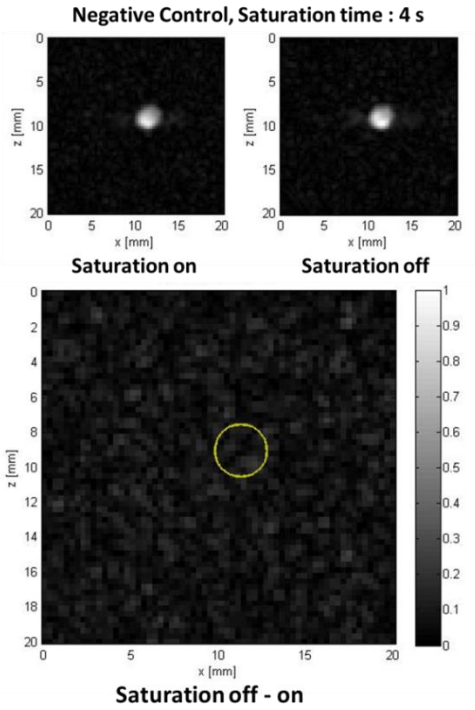
Negative Control, Saturation time : 4 s
Saturation on
Saturation off
Saturation off - on
z [mm]
x [mm]

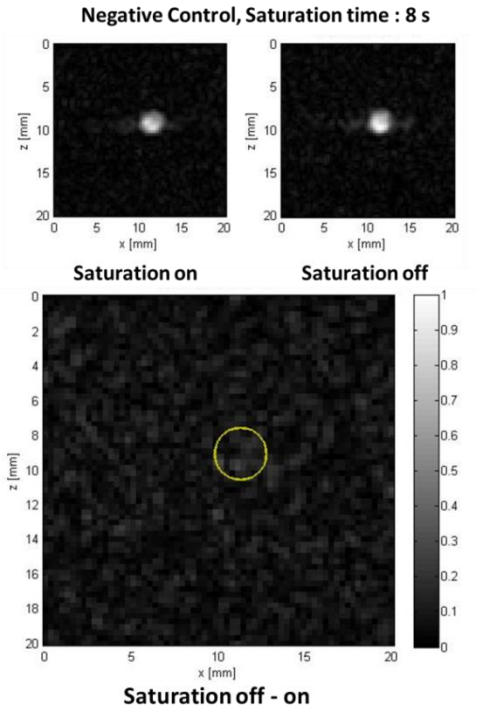
Negative Control, Saturation time : 8 s
Saturation on
Saturation off
Saturation off - on
z [mm]
x [mm]

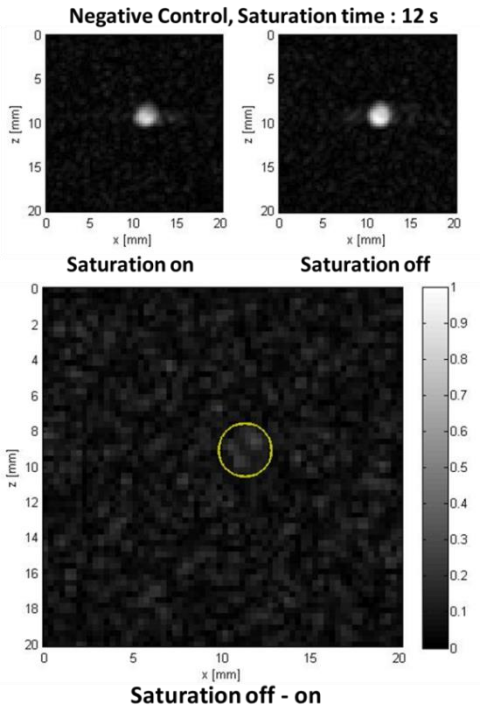
Negative Control, Saturation time : 12 s
Saturation on
Saturation off
Saturation off - on
z [mm]
x [mm]

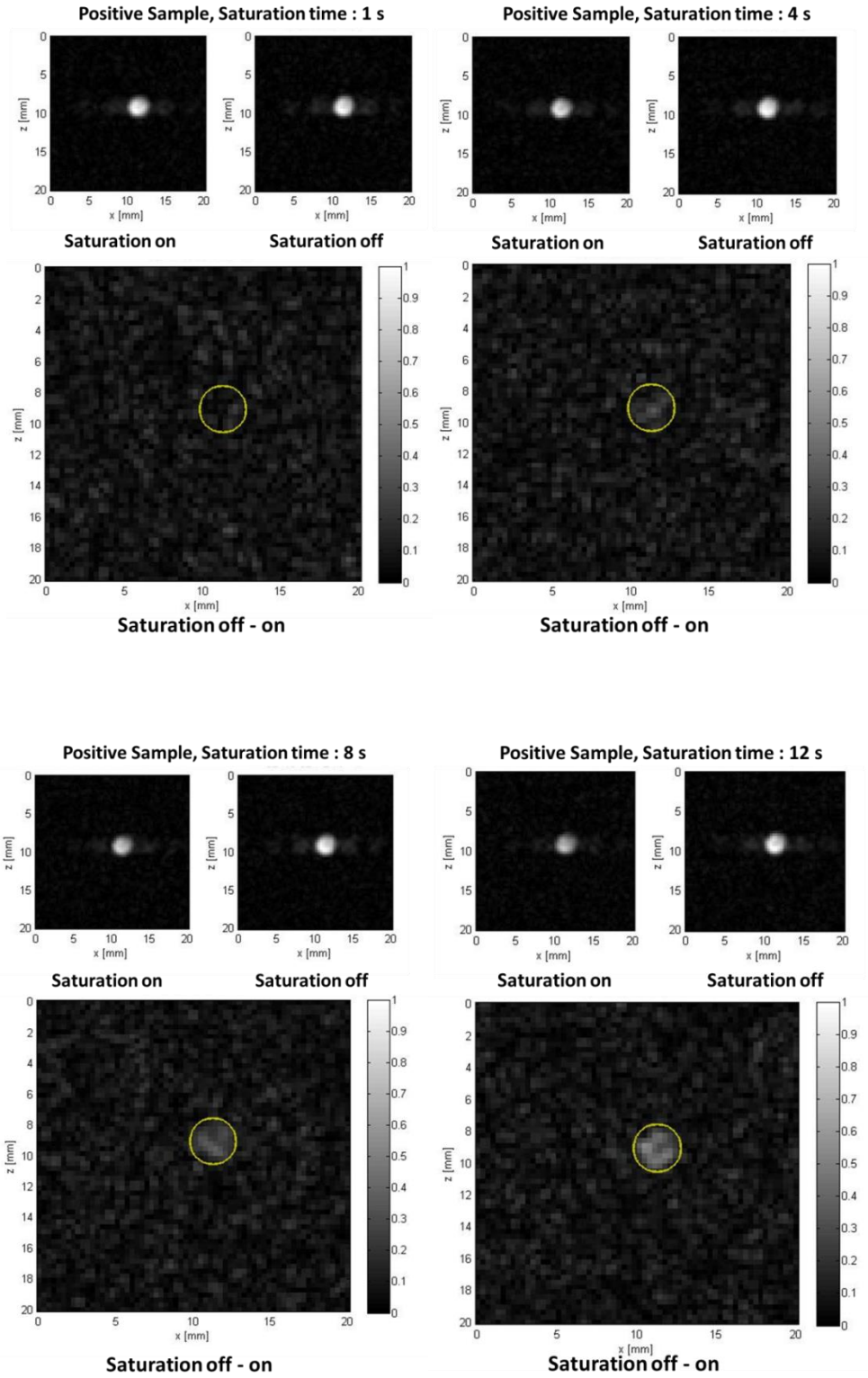

Figure S2. Hyperpolarized ^{129}Xe MRI image. Saturation on and off, subtracted image voxel by voxel. Contrast image (saturation off – on) in the different sample and saturation time. The yellow circle is the expected position for the subtracted signal from 5 mm phantom. (Real signal is slightly smaller than 5 mm in diameter because the external diameter of tube is 5mm) Inhomogeneous cell mixtures are responsible for the inhomogeneous signals.

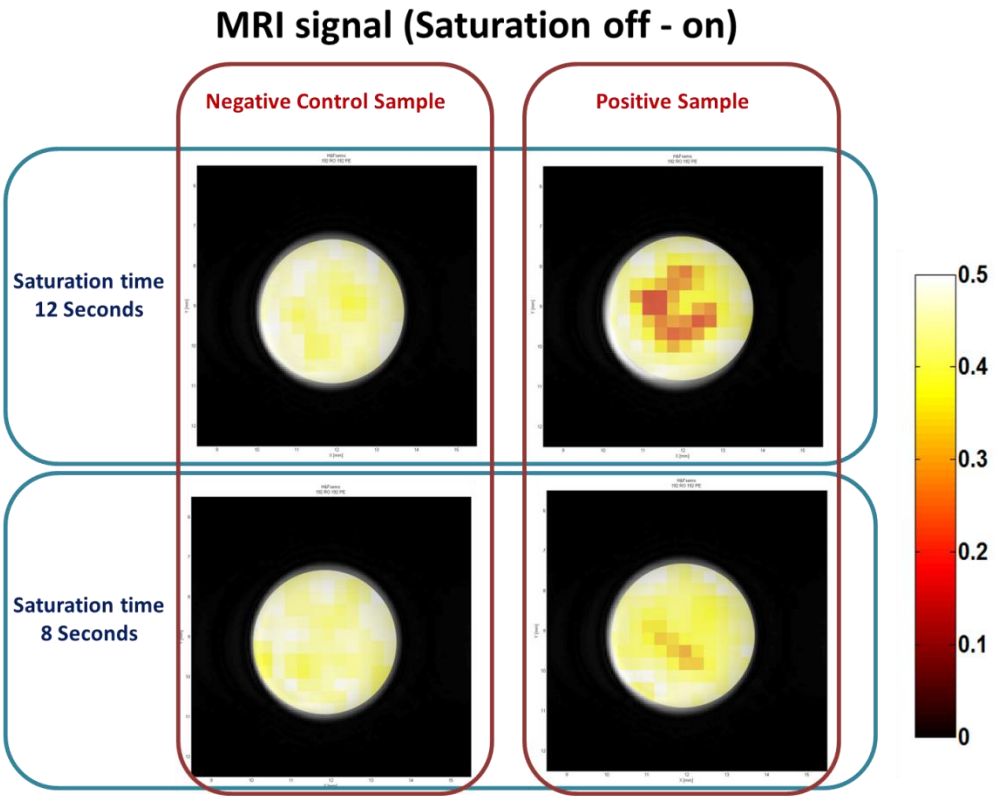

Figure S3. Color mapped contrast image (saturation off – on, reversed intensity) in the different sample and saturation time. Inhomogeneous cell mixtures are responsible for the inhomogeneous signals.

Chapter 6

Hyperpolarized ^{129}Xe NMR Biosensor Targeting the Estrogen Receptor

6.1 Abstract

An estradiol-based biosensor was developed for ^{129}Xe Hyper-CEST detection of the Estrogen Receptor (ER), one of the most important biomarkers in breast cancer. The binding was probed by a chemical shift change and line broadening upon the biosensor binding to the purified ER. The biosensor's specificity for the ER was further validated using ER-positive cancer cells, demonstrating that this novel biosensor can be used to detect breast cancer cells in ^{129}Xe NMR/MRI. The methodology could also be applied to detect endocrine disruptors in environmental samples.

6.2 Introduction

The estrogen and progesterone receptors are essential biomarkers in hormonal cancer diagnostics, as about two thirds of all breast cancers are estrogen receptor (ER) positive. An inapporopriate elevation of ERα expression has direct implications for the digagnosis and the treatment strategy of cancer—for example, in evaluating the whether hormonal therapy would be beneficial (1). Currently, the most common method for determining ER overexpression is by immunohistochemistry of a fixed tissue (2). Noninvasive methods such as positron emission tomography (PET) (3) and single-photon emission computed tomography (SPECT) (4) can offer important highly sensitive complementary *in vivo* analysis, and several ER-targeting imaging probes labeled with radionuclides such as ^{18}F (3, 5, 6), ^{99}Tc/Re (7), and others (8, 9) have been developed (10). Magnetic resonance imaging (MRI) is another powerful imaging modality, normally used with paramagnetic contrast agents which do not expose the patients to radiation. Two ER-targeting gadolinium ligands, developed based on 17-β-estradiol (EPTA-Gd) and tamoxifen (TPTA-Gd), were found to be highly selective contrast agents that allowed the localization of the estrogen receptor by MRI (11, 12). These two targeted paramagnetic contrast agents both exhibit micromolar binding affinity for ER and act as estrogen agonists in breast cancer cells (13). Unfortunately, TPTA-Gd was found to accumulate nonspecifically in muscle tissues, leaving EPTA-Gd as the most promising probe (14).

Hyperpolarized ^{129}Xe NMR spectroscopy has been established as a powerful alternative method for molecular imaging (15, 16). ^{129}Xe is a non-toxic noble gas and its wide-ranging chemical shift is sensitive to its local environment. In addition, Xe is not naturally found in organisms, which reduces the background in complex biological samples. A key challenge for the advance of ^{129}Xe

NMR/MRI as a molecular imaging technique is the development of biosensors which can localize on the target. This challenge has previously been addressed by developing sensor for selective metal ions (17), protein or small molecule-based probes targeting proteins such as streptavidin (18), the αvβ3 integrin receptor (19), matrix metalloproteinase-7 (20), human carbonic anhydrase (21), the major histocompatibility complex (22), and transferrin receptors (23, 24). Our lab has also recently developed a new biosensor with single chain antibody variable fragments (scFv) attached to a minor coat protein of a filamentous phage, allowing for selectively targeting the epidermal growth factor receptor (EGFR) (25).

Here we have combined the advantages of ^{129}Xe NMR with a targeted biosensor to develop a detection method for the most important biomarker in breast cancer, the estrogen receptor. We demonstrate that our biosensor comprised of an estradiol targeting group and a xenon hosting cryptophane cage selectively detects the ER in complex biological samples. This is shown both through experiments with the ligand binding domain of the estrogen receptor and hyper-CEST experiments with ER positive cancer cells (MCF-7).

6.3 Experiemtal section

The biosensor was synthesized with a cryptophane A cage mono acid and an ER targeting ligand, together with a hydrophilic penta-peptide to increase the water solubility of the compound (Figure 1). Ethinyl estradiol (EE2) was used as the targeting ligand, as it has a high affinity for the estrogen receptor (26), and can be readily modified through the terminal alkyne in a Huisgen coupling without affecting the agonist activity (27). The ligand binding domain of the estrogen receptor (ER) was expressed recombinantly as a fusion protein of an intein- and a chitin-binding domain. This allowed for a facile intein-mediated purification through immobilization of the fusion protein through the chitin-binding tag, removal of impurities and release of the pure estrogen receptor from the chitin beads with DTT. The ER has four cysteine residues, and to avoid undesired cross couplings, three of them (C381, C417 and C530) were mutated into serine, as these mutations do not change the conformation of the protein (28).

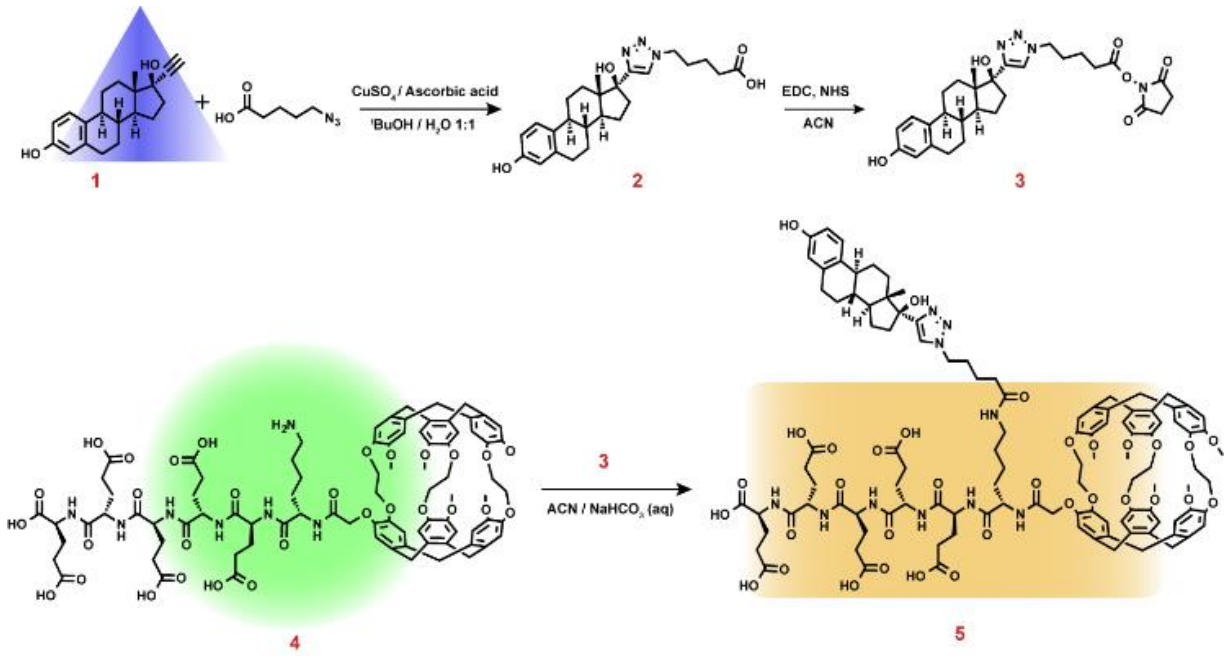

Figure 1. Biosensor synthesis. EE2 bearing an alkyne moiety is functionalized with a carboxylic acid-containing azide via click chemistry. The carboxylic acid is then activated to an NHS ester and reacted with the amine moiety on the E_5K-cryptophane cage to give the CryA-EE2 sensor.

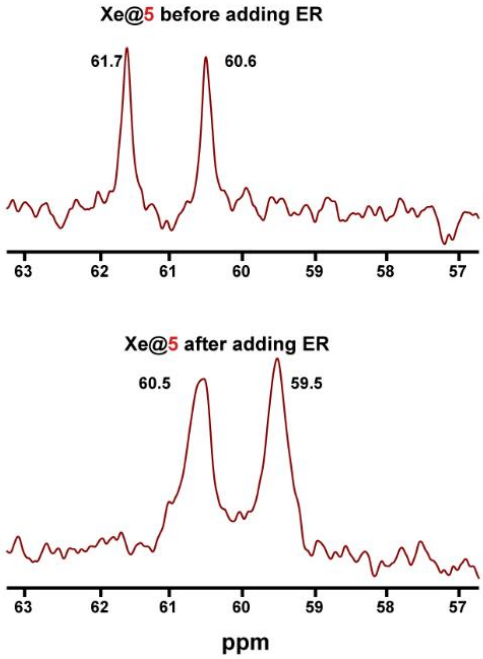

Figure 2. ^{129}Xe signal dependence on its chemical environment. Upon binding of the EE2 conjugate ligand to the ER protein, the signal of ^{129}Xe inside the cage shifts towards lower ppm values (~1.2 ppm shift). The two peaks observed are due to the diastereomers resulting from the chirality of the CryA cage. The increased peak width upon binding to the ER is additional evidence of a ligand-receptor interaction (from 30 Hz and 32Hz to 52 Hz; 67 Hz).

The CryA cage can encapsulate ^{129}Xe in solution via host-guest interactions. Clear changes in the chemical shifts of CryA biosensors have been observed when going from the "free" to the "immobilized" state in a variety of systems, such as enzymes (29), proteins (18), receptors in cells (23), and metal ions (17, 30, 31). This distinction between bound vs. unbound states is possible because the ^{129}Xe chemical shift range is wide (approximately 250 ppm (16)), and the ^{129}Xe@CryA peak is very sensitive to changes in its chemical environment. The shift is proposed to arise from configuration changes in the CryA structure after the biosensor binds to the target.

NMR experiments were performed with a flow of hyperpolarized Xenon (0.2 SLM, 35 psi) through a 5 mm phantom containing the samples. The two ^{129}Xe@EE2-CryA peaks observed in Figure 1 are due to the fact that the CryA cage is chiral and thus the biosensor has two diastereoisomers. The chemical shift of the ^{129}Xe@EE2-CryA peak was almost identical with either CryA cage only or the biosensor, as expected. When incubated with the ligand-binding domain of the estrogen receptor, a shift of more than 1.2 ppm was observed. Furthermore, while previous data indicate line broadening of the ^{129}Xe@CryA peaks upon the binding of the ligand and receptor, the new data show a two fold increase in linewidth upon binding. This verifies the binding interaction and the high resolution of signal upon binding. The specificity of the biosensor was assessed through the same experiment with a biosensor without the targeting group, resulting in only a very small shift of the peak with no binding and demonstrating the key role of the targeting group.

We further tested the biosensor in the presence of cells with hyperpolarized ^{129}Xe chemical exchange saturation transfer (CEST) NMR. We focused on ER-positive MCF-7 cancer cells, using ER-negative cells, MDA-MB-231, as controls. The cells were prepared as described in (32), and after incubation with the biosensor, the samples were transferred to the NMR probe and the Xe signal was measured after controlled addition of xenon gas. The combined Z-spectrum (Figure 3) shows an accumulation of the sensor in MCF 7 cells, but not in the ER-negative control cells.

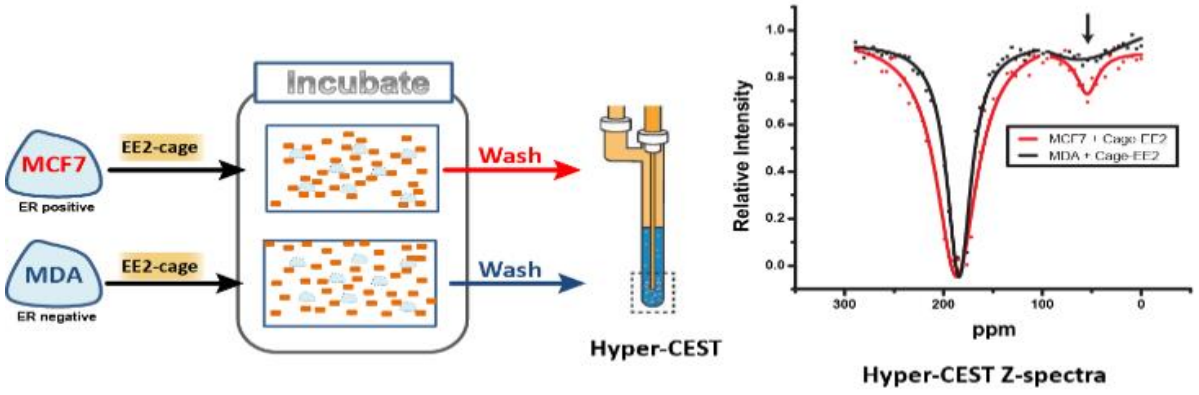

Figure 3. Z-spectra of EE2-cage biosensor interacting with breast cancer cells that overexpress (MCF7, red dots) or do not express (MDA-MB-231, black dots) the estrogen receptor. A sample of 20 million cells was fixed and incubated with 100 µM targeted EE2-cage biosensor at 4°C for 15 h. After removal of unbound sensor through multiple PBS washes, Z-spectra were obtained by flowing hyperpolarized Xe gas into the solution containing the cells. The signals obtained were then fitted with Lorentzian functions. This experiment shows that the binding only occurs in ER positive cancer cells.

To demonstrate the specificity of the biosensor to the ER, we incubated the MCF-7 cells with the biosensor with and without the targeting group. Hyper-CEST Z-spectra showed a clear response in the case of the targeted biosensor. In addition, when excess EE2 is used to outcompete the sensor the targeted receptor, the readout signal was minimal (Figure 4).

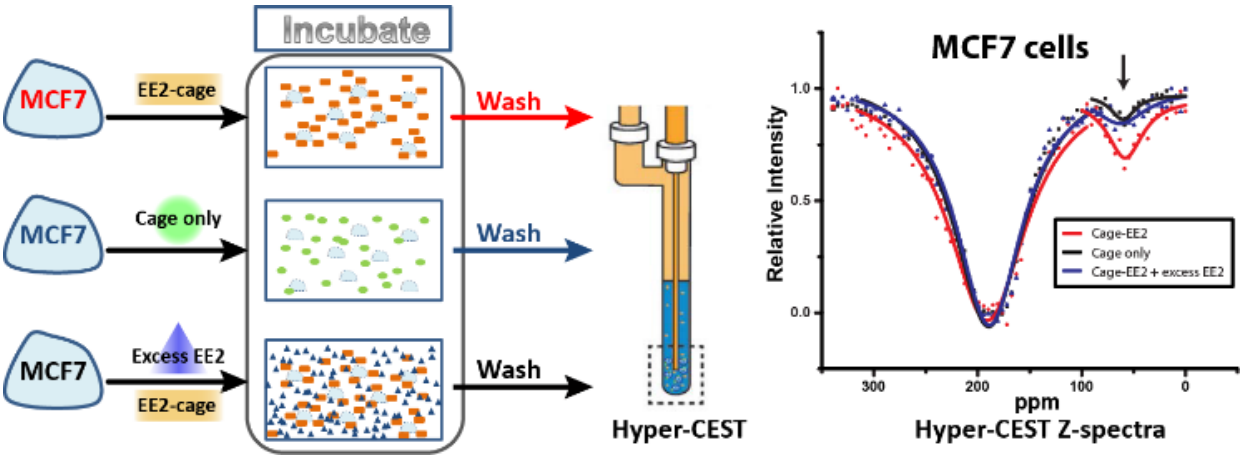

Figure 4. Hyper-CEST Z-spectra of MCF7 cells incubated with ^{129}Xe-cage species. The peak at 60 ppm is attributed to the resonance saturation of the ^{129}Xe inside the CryA cage. The broad peak at 190 ppm corresponds to ^{129}Xe in solution. For this experiment, 50 million MCF7 cells were fixed and incubated with either 100 µM targeted EE2-cage biosensor (red dots), 100 µM untargeted CryA cage (black dots) or 100 µM EE2-cage in the presence of 100x excess EE2 (blue dots) at 4°C for 15 h. After the removal of unbound agents through PBS washes, Z-spectra were obtained by flowing hyperpolarized xenon gas into the solution containing the cells. The signals obtained were then fitted with Lorentzian functions. These results indicate that the binding observed is specific to the EE2-ER interaction, as it does not occur in the case of the untargeted cage.

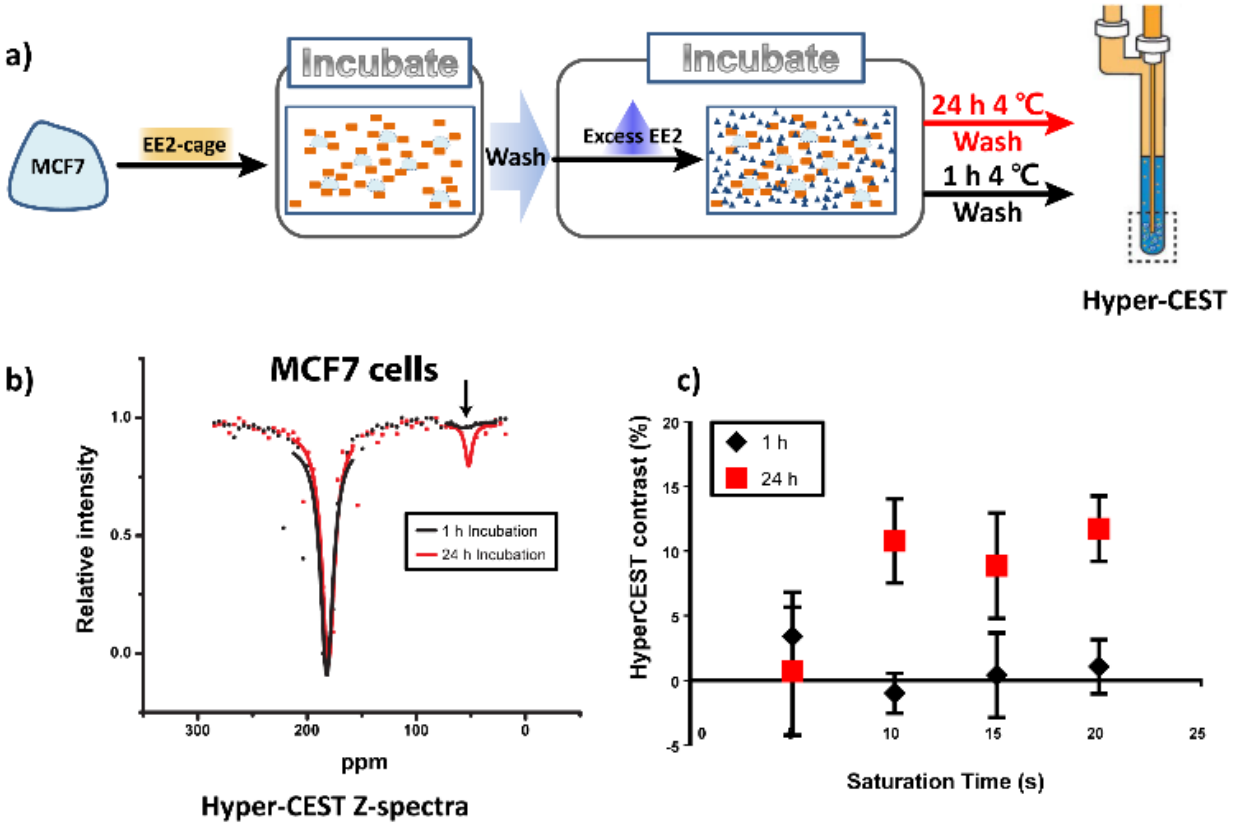

Figure 5. Hyper-CEST detection of the displacement of bound EE2-cage by excess free EE2. a) MCF7 cells (40 million) were fixed and incubated with EE2-cage for 15 h at 4 ℃, then washed to remove unbound agent. The cells containing EE2-cage bound to estrogen receptors were then incubated with excess EE2 (100x) at 4 ℃ for 1 h or 24h. The supernatant was then probed using Hyper-CEST for the presence of EE2-cage released from the cells. The Z-spectra of the supernatant at different time points are presented in b). The difference in the hyper-CEST contrast when using different saturation times is plotted in c).

Another possible application of the protocol described herein is the detection of endocrine receptors in environmental samples. EE2 has been identified as one of the endocrine disruptors with the potential to disrupt the reproductive process of aquatic animals even at low concentrations (32). Previous efforts to detect EE2 have used methods such liquid chromatography coupled with mass spectrometry (LC-MS) (33), and gas chromatography coupled with mass spectrometry (GC–MS) (34). However, these methods are not suitable for real-time detection and samples are normally decomposed after analysis. Given that ^{129}Xe-Hyper-CEST has a low detection limit (pM), we envision the use of this biosensor to facilitate EE2 detection with Hyper-CEST. In these proof-of-principle experiments, a complex between EE2-cage and ER was formed by incubating ER-positive cells with the biosensor. Upon the incubation with free EE2, the released EE2-cage was measured using Hyper-CEST. Initial results (Figure 5) are encouraging, and further optimization of the experimental setup could lead to lower detection limits, making the NMR method viable for analyzing environmental samples containing endocrine disruptors such as EE2.

6.4 Conclusion

This study shows that hyperpolarized Xe NMR can be used to detect a targeted biosensor binding specifically to the estrogen receptor. Future work will focus on the detection of this interaction in live cells overexpressing the ER on their cell surface, as well as on the detection of EE2-like endocrine disruptors in environmental samples.

6.5 Supporting information

General information. All amino acids and HCTU (1H-Benzotriazolium 1-[bis(dimethylamino)methylene]-5chloro-,hexafluorophosphate (1-),3-oxide) were purchased from either NovaBioChem or Chem-Impex International, Inc.. Fmoc-Glu(OtBu)-Wang resin (100-200 mesh) was purchased from NovoBioChem. All other chemicals were purchased from Sigma-Aldrich and used as received without further purification. Double-distilled water (dd-H_2O) used for buffers and reactions was deionized using a Barnstead NANOpure purification system (ThermoFisher, Waltham, MA). ^{1}H- and ^{13}C-NMR spectra were recorded on a Bruker Avance 400 spectrometer (1H at 400 MHz, 13C at 101 MHz). The chemical shifts are referenced to the residual solvent signal. Electrospray ionization mass spectrometry (ESI-MS) of proteins was performed using an Agilent 1260 series liquid chromatograph outfitted with an Agilent 6224 Time-of-Flight (TOF) LC-MS system (Santa Clara, CA). Semi-preparative purifications were performed on an Agilent 1100 Series HPLC Systems (Agilent Technologies, USA) with an in-line diode array detector (DAD) and in-line fluorescence detector (FLD) equiped with a Phenomenex Gemini (250x10 mm) 5 µm C-18 column. CH_3CN-H_2O (0.1% TFA) was used as eluent with a flow of 3 mL/min.

Construction of Estrogen Receptor Plasmids

General Procedure for Expression and Purification of the Estrogen Receptor. Estrogen receptor (ER) plasmids were transformed into T7 Express *lysY/I^{q}* Competent *E. coli* (High Efficiency) (C3013) cells via heat shock at 42 °C for 30 seconds and plated on LB Agar Plates containing ampicillin (100 µg/mL). Single colonies were isolated and grown overnight in Luria Broth (LB) medium (5 ml) with ampicillin (100 µg/mL final concentration). The culture was grown in 1000 mL LB containing ampicillin (100 µg/ml final concentration) at 37 °C at shaking of 250 rpm until an optical density (OD) of 0.5 was observed at 600 nm. Isopropyl-ß-D-thiogalactopyranoside (0.45 µM) was added and the cultures were grown for an additional 16 hours at 15 °C. The cells were then spun down for 15 min at 5,000 rpm at 4 °C and stored at -20 °C. The ER was purified with the same protocol as described earlier (35). Briefly, the cells were thawed on ice and re-suspended in 15 mL of Lysis Buffer (20 mM Tris, pH 8.5, 2 M urea, 0.5 M NaCl, 1 mM EDTA, 10 µM of 17-β-estradiol, 0.01% NaN_3) and lysed by sonication for 20 min (2 s on and 4 s off) with a blunt ended tip. Debris was removed by centrifugation at 13,000 rpm for 45 min to give a transparent solution. The estrogen receptor was purified utilizing a 25 mL fritted column loaded with 5 mL of Chitin Resin (New England Biolabs, neb.com). Lysate was incubated with the resin for 30 min. The resulting resin-bound protein was washed with 10-20 column volumes of Wash Buffer (20 mM Tris, pH 8.5, 0.5 M urea, 0.5 M NaCl, 1 mM EDTA

(ethylenediaminetetraacetic acid), 10 µM of 17-β-estradiol, 0.01% NaN_3). A 15 mL solution containing 50 mM dithiothreitol (DTT) in Wash Buffer was flowed over the resin bound protein using suction. The column bed was allowed to stand in this solution at room temperature for 2 days. Protein was eluted from the column with addition of 20 mL of Wash Buffer. Purified protein was then concentrated, using Amicon Ultra 15 mL 10,000 MWCO (Millipore) centrifugal ultrafiltration membranes at 4 °C to remove residual DTT. The purity of the protein was confirmed by SDS-PAGE gel and mass spectrometry.

Construction of Biosensor

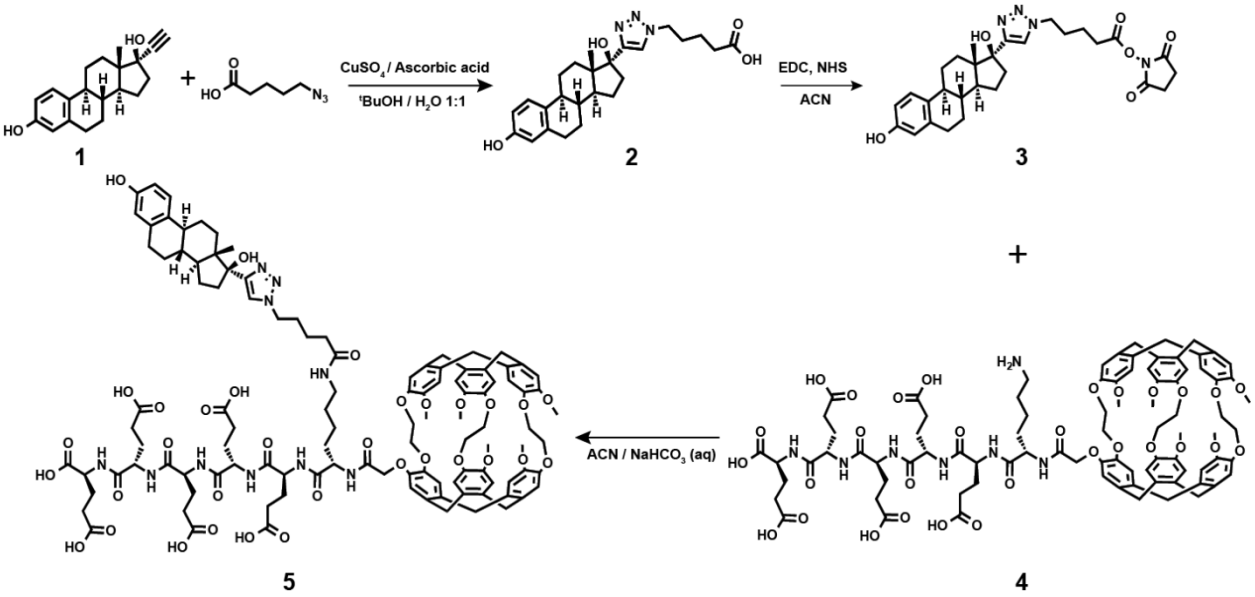

Synthesis of 2

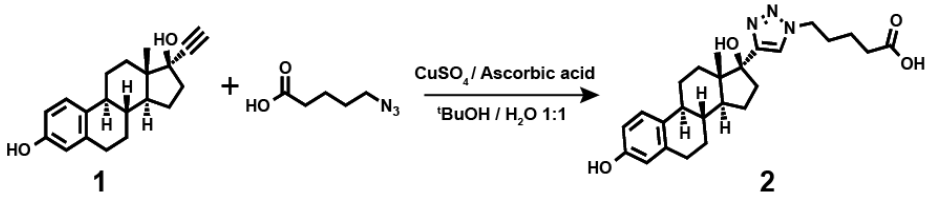

In a 15 mL plastic container equiped with a magnetic stirrer, to 5-azidopentanoic acid (130 mg; 908.14 µmol) and EE2 (225 mg; 760 µmol) was added tBuOH:H_2O 1:1 (1400 µL). 1 M Ascorbic acid (76 µLl; 76 µmol) and 0.3 M $CuSO_4$ (25.3 µL; 7.6 µmol) were added giving a total volume of 1501 µL and 0.51 M concentration of EE2. The milky solution was left stirring at room temperature overnight. Water (4 mL) was added the next day and white precipitate was

observed. After centrifugation and removal of the filtrate, more water (4mL) was added to wash and the white solid was lyophilized. Yield: 320 mg (96%)

^{1}H NMR (400 MHz, d_6-DMSO) δ 11.9 (bs, 1H), 8.98 (bs, 1H), 7.84 (s, 1H), 6.95 (d, *J* = 8.5 Hz, 1H), 6.46 (dd, *J* = 8.4, 2.4 Hz, 1H), 6.41 (d, *J* = 2.3 Hz, 1H), 5.08 (s, 1H), 4.33 (t, *J* = 6.9 Hz, 2H), 2.69 (m, 2H), 2.35 (m, 1H), 2.25 (t, *J* = 7.0 Hz, 2H), 2.08 (d, *J* = 10.6 Hz, 1H), 1.92 (t, *J* = 12.6 Hz, 1H), 1.82 (m, 5H), 1.63 (m, 1H), 1.45 (m, 4H), 1.31 (m, 1H), 1.21 (m, 2H), 0.92 (s, 3H), 0.58 (t, *J* = 11.1 Hz, 1H). ^{13}C NMR (101 MHz, d_6-DMSO) δ 174.04, 154.86, 154.03, 137.16, 130.46, 126.00, 122.56, 114.87, 112.64, 81.07, 48.82, 47.53, 46.69, 43.16, 37.21, 32.67, 29.28, 27.20, 26.08, 23.57, 21.53, 14.39. HRMS: Calculated for $C_{25}H_{34}O_4N_3$: 440.2544. Found: 440.2554 (2.31 ppm)

Synthesis of 3

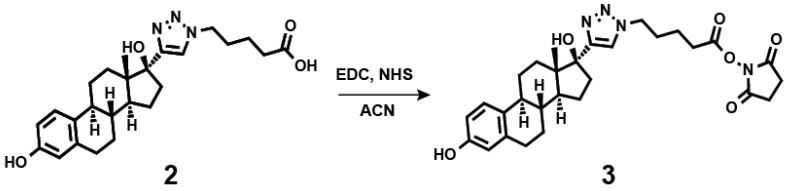

The carboxylic acid **2** (14.30 mg; 32.57 µmol), EDC (1-ethyl-3-(3-dimethylaminopropyl)carbodiimide) (18.0 mg; 93.90 µmol), N-hydroxysuccinimide (12.0 mg; 104.27 µmol) were dissolved in acetonitrile. DIPEA (10 µL; 92.6 µmol) was added and the solution was left stirring for one hour. Purification on reversed phase HPLC and freeze drying gave a white solid (12 mg, 67 %). HRMS Calculated for $C_{29}H_{37}O_6N_4$: 537.2708. Found: 537.2697 (1.98 ppm)

Synthesis of 4

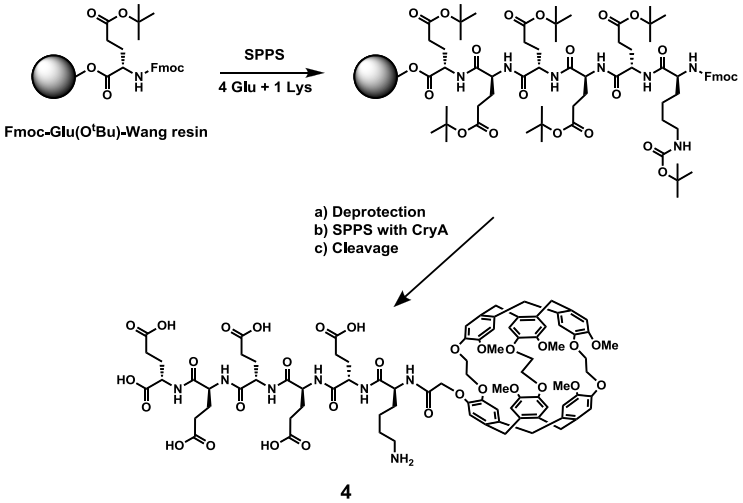

The peptide was synthesized employing standard Fmoc solid-phase peptide synthesis using Fmoc-Glu(OtBu)-Wang resin (0.57 mmol/g), 5 equiv of amino acid, 5 equiv HCTU, and 10 equiv DIPEA (N,N-Diisopropylethylamine) in DMF until full conversion was observed by Kaiser test. The deprotection of Fmoc protecting groups was carried out with 20% (v/v) piperidine in DMF

for 15 minutes. CryA cage (2 equiv) (supplied by Kang Zhao, Tianjin University in China) was coupled by HCTU (2 equiv) and DIPEA (4 equiv) for 24 hours. The peptide was released from the resin by treatment with trifluoroacetic acid : water : triisopropylsilane (95:2.5:2.5) for 3 h. The TFA solution was concentrated by nitrogen flow and precipitated with Et_2O twice giving an off-white powder. Purified on semi-prep HPLC and freezedried giving a white solid. ESI-MS calculated for $C_{86}H_{102}N_7O_{30}$ $[M+H]^+$ 1712.6666 found 1712.6717.

Synthesis of CryA-EE2 5

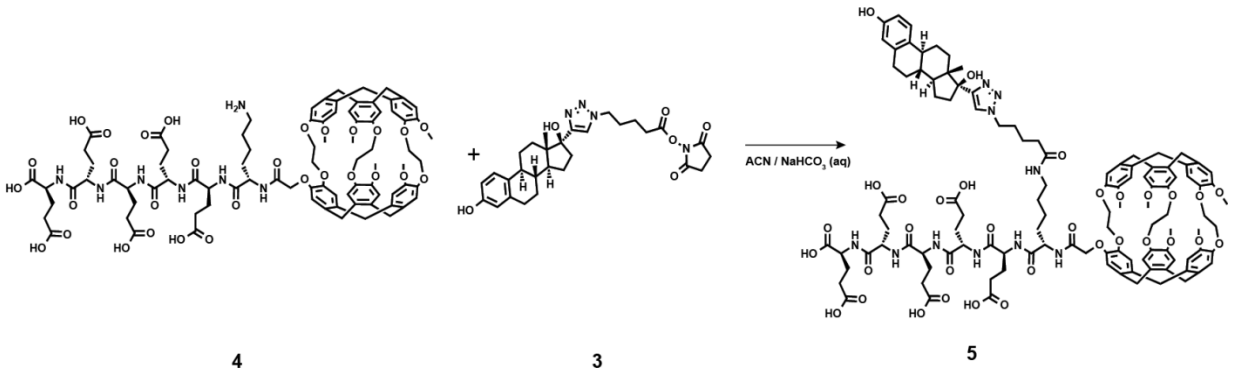

4 3 5

CryA linker **4** (8.5 mg; 4.97 µmol) was transfered to a 2 mL HPLC glass vial. A small magnetic stirrer was added and EE2-NHS ester **2** (10 mg; 16.86 µmol), dissolved in acetonitrile (200 µL), was added giving a clear solution. 500 mM $NaHCO_3$ (28 µL; 14 µmol) was added and the solution was left stirring at room temperature for 1 hour. The sample was purified on semi-prep and freezedried giving a white solid (4.5 mg, 41%). HRMS : Calculated for $[M+2H]^{2+}$: $C_{111}H_{134}N_{10}O_{33}$: 1067.4552. Found: 1067.4591 (3.66 ppm)

Analyzing the biosensor by ^{129}Xe NMR. Purchased gas mixture (2% ^{129}Xe, 10% N_2, 88% He) was hyperpolarized via spin-exchange optical pumping (36). After polarization, the gas was routed directly to a 5 mm NMR tube. ^{129}Xe was dissolved into the sample solution via bubbling through a capillary running down to the NMR tube at a rate of 0.2 SLM for 10 seconds. Total gas pressure was maintained at 2.4 atm. The bubbling period was followed by a 2 s wait period to allow the solution to settle down for obtaining higer ^{129}Xe in solution signal and 0.8 sec wait period followed by 2 sec exchange time was used for detecting ^{129}Xe in gas mixture signal. All ^{129}Xe NMR data were acquired on a 110.595 MHz (9.4 T) Varian VNMRS console. Spectra were acquired with 50 kHz spectral width in 0.5 second. Temperature was maintained at 20±0.1 °C. All ^{129}Xe chemical shifts in solution were evaluated by referring to the ^{129}Xe in water signal, which was calibrated at 192 ppm (37). For Hyper-CEST profiles we used the same procedure as in the previous study (38) except the number of arrays (with same saturation frequency array increment : 500Hz). In brief, after 10 sec bubbling time, a saturation hard pulse of 23 dB power was irradiated with different saturation times (Fig. 3, 4 : 5 sec, Fig. 5b: 15 sec, Fig, 5c: averaged from 3 different acqusitions from each 5, 10, 15, 20 sec saturation time) and spectra were acquired in a same way of single spectrum acquisition. MATLAB software (The MathWorks Inc) was used for data processing. FIDs were zero-filled to 16384 points, the baseline was corrected, apodizided with 11 Hz exponential, and Fourier transformed. Each Xe@H_2O area in the

spectrum was integrated and the contrast of each spectrum was compared between the maximum and minimum area in each data series. Each profile was fitted with a Lorentz profile using Origin 8.0 (OriginLab Software Inc).

^{129}Xe-NMR of breast cancer cells. All cell culture reagents were obtained from Gibco/Invitrogen Corp. (Carlsbad, CA) unless otherwise noted. Cell culture was conducted using standard techniques, in culture-treated flasks (Corning, Tewksbury, MA). MCF7 and MDA-MB-231 cells were grown in Dulbecco's Modified Eagle Medium (DMEM) supplemented with 10% (v/v) fetal bovine serum (FBS, Omega Scientific, Tarzana, CA) and 1% (v/v) penicillin/streptomycin (P/S), in a 5% CO_2 atmosphere at 37 ˚C. Cells were washed once with PBS and trypsinized with 1x trypsin for 5 minutes at 37 ˚C. The detached cells were spun down and resuspended in 10 mL, counted and repelleted. The cells were then resuspended at 10^7 cells/mL and incubated in 0.25% paraformaldehyde/PBS for 1 h in the dark, at room temperature. The cells were washed once with PBS, then resuspended at 10^7 cells/mL in 70% MeOH/PBS and incubated for 1 h in the dark, on ice. Next, a 0.05% TritonX-100/ PBS solution was used to permeabilize the cells (10^7 cells/mL, 10 min, dark, room temperature). The cells were blocked with 1:2 normal goat serum (NGS):PBS for 2 h at 37 ˚C (3 x 10^7 cells/mL). Compounds were diluted with 1:2 NGS:PBS to a final concentration of 10 µM (from 1 mM stock solutions) and the cells were incubated at 3 x 10^7 cells/mL for 14 h in the dark at 4 ˚C. In the case of the competition experiment with free EE2, a 100 mM stock in DMSO was added to reach a final concentration of 1 mM. Upon incubation, the cells were spun down, the supernatant removed and the cells were washed 3 x 10 mL Dulbecco's Phosphate Buffer Saline (DPBS) with 1% FBS, then resuspended in ~500 µL 1% FBS in DPBS for NMR analysis.

Chapter 7

Targeted Molecular Imaging of Cancer Cells using MS2-Based ^{129}Xe NMR

(Reprinted with permission from Bioconjugate Chemistry, 27, 1796-1801 (2016) "Targeted Molecular Imaging of Cancer Cells using MS2-Based ^{129}Xe NMR" by **Keunhong Jeong**, Chawita Netirojjanakul, Henrik K Munch, Jinny Sun, Joel A Finbloom, David E Wemmer, Alexander Pines, Matthew B Francis. Copyright 2016 American Chemical Society.)

7.1 Abstract

We have synthesized a targeted, selective, and highly sensitive ^{129}Xe NMR nanoscale biosensor using a spherical MS2 viral capsid, Cryptophane A molecules, and DNA aptamers. The biosensors showed strong binding specificity for the targeted lymphoma cells (Ramos line). Hyperpolarized ^{129}Xe NMR signal contrast and hyper-CEST ^{129}Xe MRI image contrast indicated its promise as highly sensitive hyperpolarized ^{129}Xe NMR nanoscale biosensor for future applications in cancer detection *in vivo*.

7.2 Introduction

Magnetic Resonance Imaging (MRI) is a highly useful medical imaging tool, affording high-resolution images with minimal invasiveness. This well-established technique generally detects the protons of water and lipids in the body, which provides flexible and detailed anatomical imaging due to the high abundance of these molecules. However, the imaging of specific, non-abundant molecules of interest, such as cancer biomarkers, is significantly limited by the low signal-to-noise ratio that can be achieved against the background of ubiquitous water molecules. In these cases other nuclei can be imaged, but the low polarization under normal conditions limits both detection levels and dynamic range. To overcome these problems, various techniques have been developed to enhance signal intensity and sensitivity, and these are often combined with molecular sensors to generate localized contrast with high chemical specificity. In particular, hyperpolarization by spin exchange optical pumping and dynamic nuclear polarization (DNP) have been highlighted as methods to increase polarization, and hence imaging sensitivity, which is particularly important for nuclei other than protons (1, 2).

^{129}Xe is an ideal reporter for NMR because it is inert, hyperpolarizable, biocompatible, and provides no natural background signal in living systems (3, 4). The use of hyperpolarized ^{129}Xe as an imaging agent has been demonstrated in the magnetic resonance imaging of lung tissue (5, 6), brains (7, 8), and kidneys (9). For molecular imaging, Cryptophane A (CryA) based xenon sensors have been developed with chemical exchange saturation transfer (CEST) to increase the detection sensitivity by 1,000-fold relative to the direct observation of the caged xenon (3, 10, 11). Molecular sensors carrying large numbers of CryA moieties coupled to targeting groups

provide a further increase in sensitivity, and have been applied to the detection of cancer cells. Hyper-CEST NMR imaging with these multivalent CryA sensors may thus provide powerful tools for the detection of molecular targets - especially those on cancer cells for which early stage detection is highly critical for patient survival (12).

Previous studies in our groups have found that bacteriophage MS2 has a long circulation half life *in vivo* (13), and is a promising water soluble scaffold for encapsulating hydrophobic CryA entities. Key to its success is the presence of thirty-two 2 nm pores in the 27 nm protein shell, which provide rapid access of small reagents and Xe into the internal volume. This allows over 100 CryA molecules to be housed inside the sphere in a manner that avoids loss of water solubility that would otherwise be expected if these were attached externally (14). Our previous studies with a MS2-CryA construct were limited to untargeted carriers that could not engage specific cells (15). More recently, filamentous phage with genetically encoded single chain antibody (scFv) groups were used to distinguish between different cell types based on their surface markers. In that study, the CryA groups were installed on the external surfaces of the carriers, accompanied by over 1000 molecules of polyethylene glycol (PEG) to maintain solubility and prevent aggregation.

The need for solubilizing PEG coatings limits the potential for the orthogonal attachment of targeting moieties. An optimized carrier would combine aspects of both designs, integrating the dense sphere of CryA molecules housed inside MS2, with large numbers of external targeting groups through a modular coupling strategy. Here we report the generation and evaluation of such a system, providing both a high payload of internal CryA groups and external targeting aptamers for the highly sensitive detection of lymphoma cells.

7.3 Results and discussion

The MS2 protein monomers used in this study were engineered with the N87C mutation, which created a series of 180 sulfhydryl groups facing the interior surface of each capsid following assembly (16). To enable the use of oxidative coupling strategies for the introduction of targeting moieties on the external surfaces (16, 17), *p*-aminophenylalanine (*p*AF) residues were also incorporated into position 19 of each monomer (resulting in 180 per assembled capsid) using the Schultz amber suppression technique (16-18). The interior of the N87C-T19*p*AF capsids was first modified with CryA-maleimide (CryA-Mal) (Figure 1B). To increase the solubility of the conjugate during the conjugation step, five glutamic acids were incorporated into the CryA-Mal linker, which was prepared with solid phase peptide synthesis (SPPS) (Figure 1B and Supporting Information Figure S1). ESI-TOF-MS analysis of the MS2 coat protein after coupling and disassembly revealed that about 60% of the monomers had been modified, corresponding to an average of 110 CryA molecules per intact capsid (Figure 1B). In a separate set of capsids, the cysteine residues were labeled with Oregon Green maleimide to allow their detection in flow cytometry experiments. Virtually complete labeling of the 180 cysteine residues was achieved in this case (Supporting Information Figure S2).

We chose DNA aptamers as targeting agents due to evolvable specificity and affinity for tumor cell biomarkers (19). The exterior of MS2 was modified with the TD05.1 aptamer, which targets membrane-bound mIgM markers expressed on lymphoma cells (20, 21). The DNA aptamers were modified with aminophenol groups at the 5'-termini, allowing them to be conjugated to the aniline side chains of the *p*AF residues via oxidative coupling in the presence of sodium periodate (16, 20, 22). SDS-PAGE analysis indicated that approximately 30% of the 180 monomers were derivatized with oligonucleotides, which resulted in significant gel shifts (Figure 1C). Additionally, the addition of the CryA groups to the MS2 monomers resulted in the appearance of slower migrating bands that corresponded to both the unmodified and the DNA-conjugated proteins (Figure 1C).

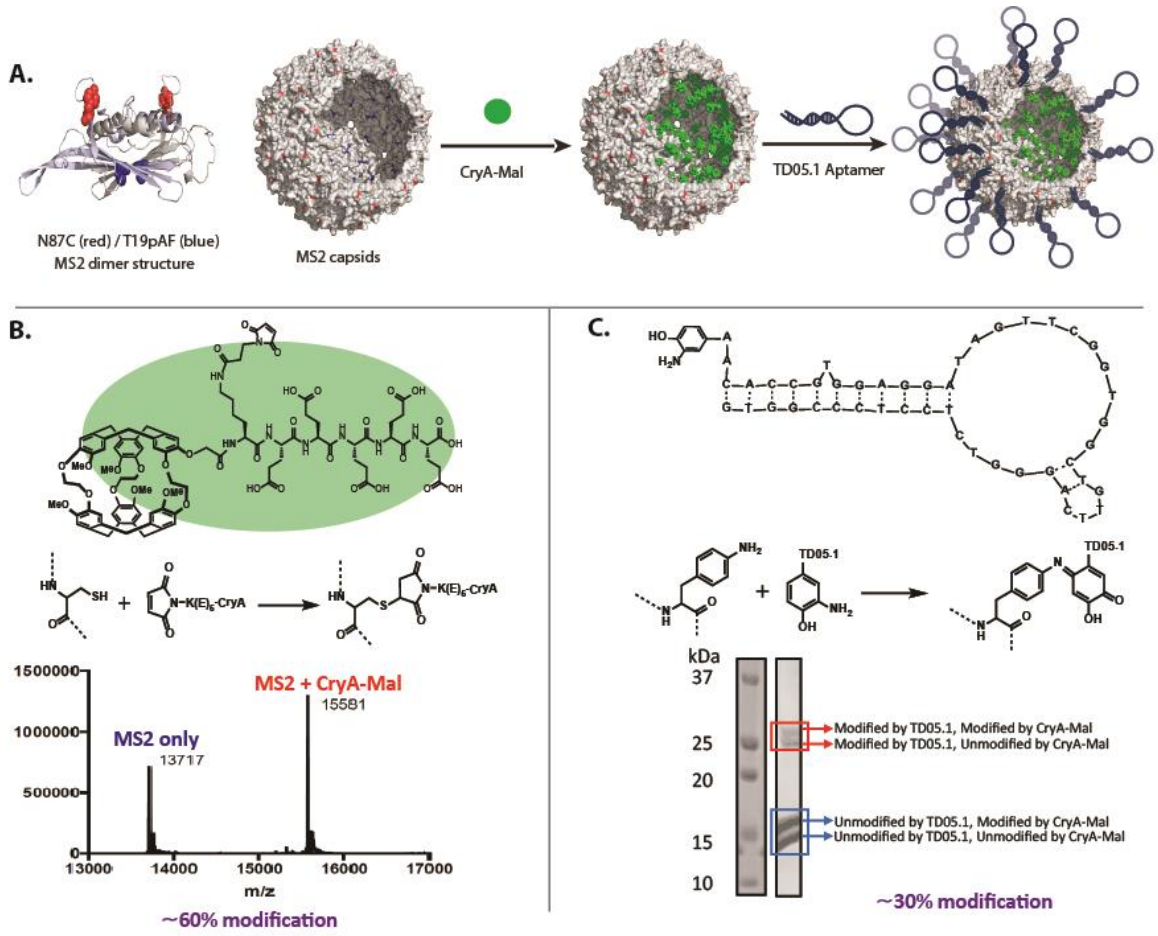

Figure 4. Scheme of ^{129}Xe-biosensor synthesis and identification. (A) The MS2 viral capsid (PDB ID : 2MS2 (23))was modified with CryA-Mal at a series of ~110 N87C positions on the interior surface of the capsid. This was followed by the attachment of 54 aminophenol-TD05.1 aptamers to T19pAF residues on the exterior surface. (B) Interior thiol-maleimide reactions on N87C positions with the CryA-Linker shown (20 equiv CryA, pH 7.2 phosphate buffer, rt, 6 h) resulted in the modification of 60% of the available cysteines, as determined using ESI-TOF MS. (C) Exterior oxidative coupling reactions on T19pAF residues with TD05.1 DNA-aminophenol molecules (10 equiv aminophenol-TD05.1 aptamer, 25 equiv. NaIO4, pH 6.5 phosphate buffer, rt, 5 min) led to the modification of 30% of the capsid proteins, as determined using SDS-PAGE and densitometry analysis after Coomassie staining.

To verify the ability of the doubly-modified MS2 capsids to target cancer cells, the fluorescent versions of the capsids (Supporting Information Figure S2) were exposed to Ramos Burkitt's lymphoma cells, which are positive for the mIgM marker. Following 1 h of exposure on ice, flow cytometry analysis indicated strong binding of the TD05.1-labeled capsids to the targeted cells (Figure 2). As a negative control, the TD05.1-labeled capsids were also exposed to Jurkat cells, which are a T-cell leukemia line that lacks the mIgM groups. In this case, only a minor increase in fluorescence was observed upon flow cytometry analysis (Figure 2). Taken together, these experiments indicate that the capsid-bound aptamer interaction remains specific for the mIgM group.

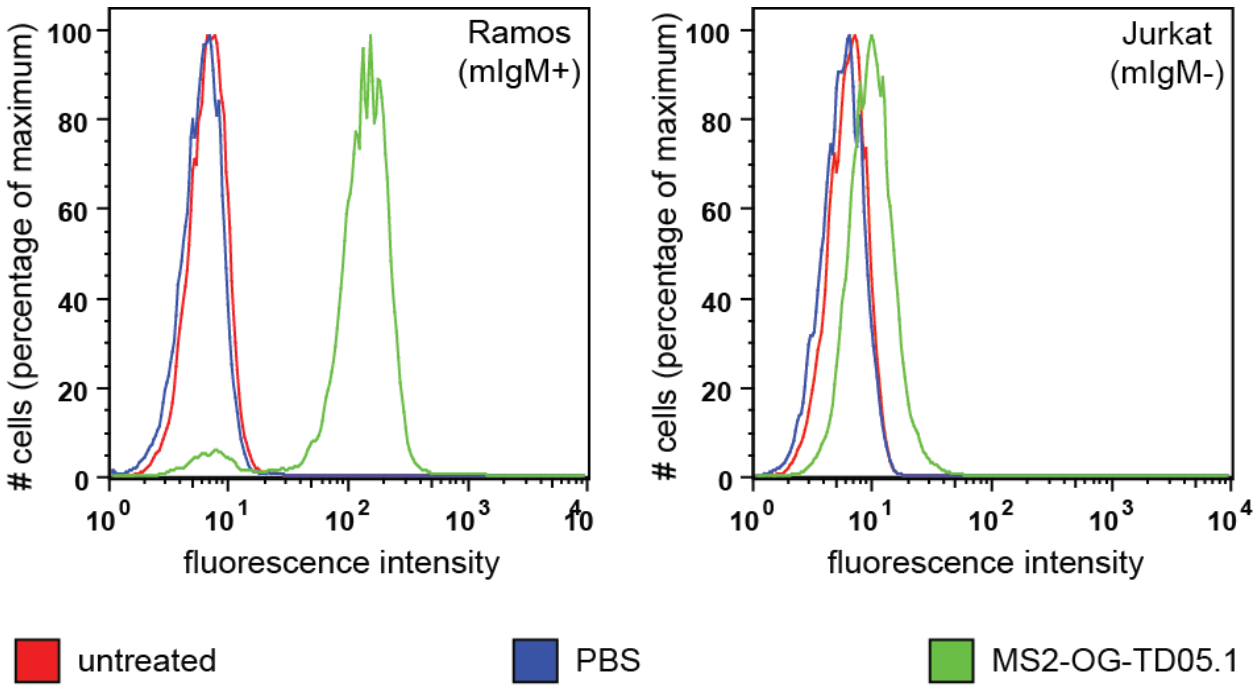

Figure 5. Binding specificity analysis of MS2-TD05.1 conjugates. The MS2 viral capsids were fluorescently labeled with Oregon Green maleimide dyes at the interior N87C positions, followed by modification with aminophenol-TD05.1 aptamers at the T19*p*AF sites on the exterior. The MS2-OG-TD05.1 constructs were then incubated with Ramos (mIgM+) and Jurkat (mIgM–) cells on ice for 1 h. Flow cytometry analysis indicated that the MS2-OG-TD05.1 agents bound to the Ramos target cells but not the Jurkat cells.

The ability of the capsids to report the presence of the targeted biomarker using ^{129}Xe Hyper-CEST NMR was next demonstrated using the same aptamer sequence. MS2-CryA-TD05.1 conjugates were incubated with a sample of $2x10^7$ Ramos or Jurkat cells in 0.5 mL of a binding buffer that contained 4.5 g/L glucose, 5 mM $MgCl_2$, 1% BSA, and 0.1 mg/mL yeast tRNA (see Experimental part for details) for 1 h on ice. Unbound MS2 was then removed using two washes with binding buffer, and cells were transferred to RPMI media containing 0.2% L-81 to suppress

foaming. Hyperpolarized ^{129}Xe gas was flowed through a tube from the polarizer to the solution of cells. Hyper-CEST detection was employed by applying a selective-bandwidth saturation pulse (dSNOB) and monitoring the degree of saturation transfer. A broad Xe@CryA peak was identified at 57 ppm (which is consistent with previous observations) (14) in the Ramos cell sample (Figure 3A). In contrast, this peak was entirely absent in the Jurkat sample. This indicated that the targeted capsids were capable of distinguishing between the cell populations, as was observed in the flow cytometry experiments.

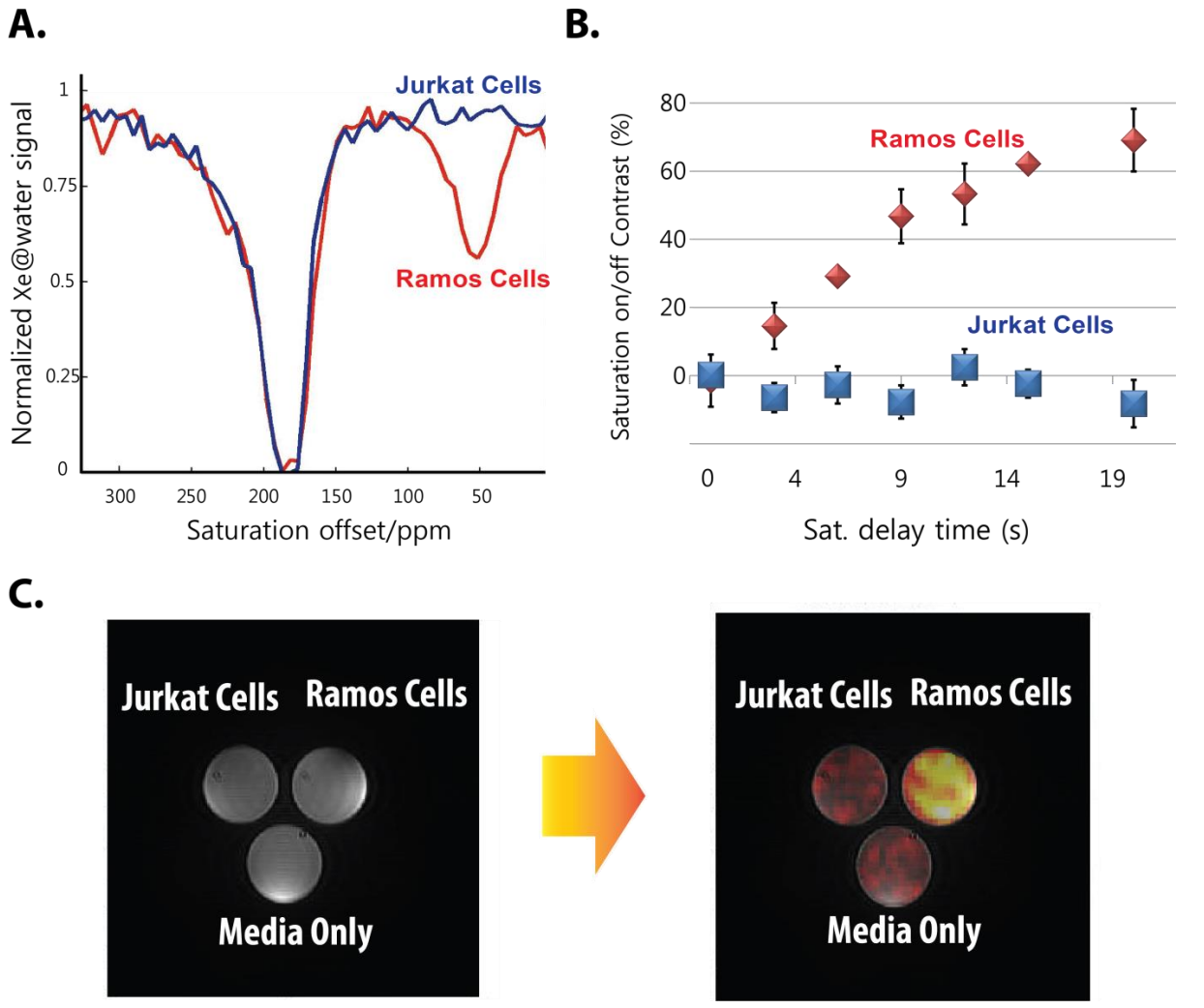

Figure 6. NMR / MRI experiments with cell suspension samples. The MS2-CryA-TD05.1 agents (167 nM in capsids) were incubated with 2x10^7 Ramos or Jurkat cells for 1 h on ice. Following this, the cells were washed three times to remove unbound biosensors. The cells were resuspended in 500 µL of media for NMR/MRI analysis. (A) Hyper-CEST spectra corresponding to Ramos and Jurkat cell samples. The data indicate that MS2 biosensors only remain bound in the Ramos samples. (B) The on vs. off saturation contrast values were measured for different saturation times using the two cell samples. (plots with contrast ± standard deviation for four replicates) (C) Hyper-CEST

saturation MRI contrast images clearly distinguished the receptor-positive cell sample (left: proton image, right: Hyper-CEST ^{129}Xe image overlapped onto the proton image).

A contrast diagram was produced by comparing the off-resonance and on-resonance saturation signals for each cell solution as a function of saturation time (Figure 3B). The result again confirmed the presence of biosensors only in the Ramos cell population. Increasing saturation time was found to enhance the contrast and thus provide higher detection sensitivity, ultimately reaching a contrast difference of 69 ± 9% with a 20 s saturation duration.

To explore the potential of the capsid carriers as targeted MR imaging agents, a ^{129}Xe hyper-CEST saturation MRI contrast map (24) was obtained by comparing the off-resonance and on-resonance images for a sample comprising three tubes: media only, media with Jurkat cells, and media with Ramos cells (Figure 3C). The two cell-containing samples were exposed to the MS2-CryA-TD05.1 agents as described above. An 8 s saturation time was used in this experiment. As expected there was no contrast in the media and Jurkat tubes. However, strong contrast was generated for the Ramos cell sample. This result demonstrates that the capsid-based nanocarriers can indeed report biologically relevant levels of a specific biomarker in an MR image.

7.4 Conclusion

The *In vivo* use of xenon MRI has been widely studied (32, 33). The saturation time that can be applied is largely determined by the ^{129}Xe relaxation time (T1), which is about 20 s in lung tissue and 4-13 s in dissolved oxygenated blood (34, 35). Furthermore, Mugler et al. (36) observed that the transit time of dissolved ^{129}Xe from lung to brain in humans by blood flow is 5 s. A recent study with modified MS2 showed that more than 8% of MS2 was distributed in the rat lung at 24 hours after dosage and more than 20 % of MS2 remained in blood (13). Together, these findings suggest that hyperpolarized xenon transfer in the lung will provide sufficient signal for detection of specific cancer cells targeted with the MS2-CryA conjugates in MRI images.

Here we describe the synthesis of a high sensitivity MS2-based ^{129}Xe NMR nanoscale sensor that selectively recognizes cancer cells. The biosensor prepared was designed to target a lymphoma cell line; however, the attachment of other aptamers, peptides or antibodies to the exterior of MS2 is straightforward due to the flexibility of the oxidative coupling strategy. This suggests broad applicability of this construct as *in vivo* explorations commence. We have also demonstrated the advantage of the internal CryA functionalization strategy for increasing agent sensitivity, in conjunction with ^{129}Xe Hyper-CEST. Importantly, along with recent extensive ^{129}Xe sensitive biomaterial developments (25-28), this work provides a strong basis for the continued development of targeted cancer cell imaging agents not only from bacteriophage MS2 but also from other bioengineered protein-based nanomaterials for future application in NMR and MRI.

7.5 Materials and methods

MS2 Capsid – TD05.1 Binding Assays. Flow cytometry was used to determine binding ability of all of the MS2-aptamer constructs. For all samples, 100 µL of $2x10^6$ cells/mL of Ramos or Jurkat cells were used, suspended in binding buffer (4.5 g/L glucose, 5 mM $MgCl_2$, 0.1 mg/mL yeast tRNA (Sigma) and 1 mg/mL BSA (Fisher) in Dulbecco's PBS with calcium chloride and magnesium chloride (Invitrogen)). To these cells were added 10 µL of 6 µM MS2-OG-TD05.1 construct solutions (MS2-OG monomer concentration, Supporting Information Figure S2). The samples were then incubated on ice for 1 h. The resulting cells were washed twice with 500 µL of binding buffer and resuspended in 200 µL of binding buffer. The cells were analyzed by flow cytometry (FACSCalibur flow cytometer, BD Biosciences) to determine the amount of Oregon Green fluorescence. For each sample, 10,000 cells were counted.

Analyzing Biosensor by ^{129}Xe NMR. A gas mixture (2% ^{129}Xe natural abundance, 10% N_2, 88% He) was hyperpolarized via spin-exchange optical pumping using a homebuilt polarizer. After polarization, the gas was routed directly to a 5 mm NMR tube. ^{129}Xe was dissolved into the sample solution via bubbling through a capillary running down to the bottom of the NMR tube at a rate of 0.4 SLM for 10 s. Total gas pressure was maintained at 2.38 atm. The bubbling period was followed by a 4 s wait period to allow the solution to settle. All ^{129}Xe NMR data were acquired on a 400 MHz (9.4 T) Varian VNMRS console. Spectra were acquired with 30.5 kHz spectral width in 1 s. ^{129}Xe NMR was carried out with 40 million cells mL^{-1} concentration of Ramos cells and Jurkat cells, respectively. After rinsing out unbound biosensors, the saturation profile of each sample was measured by recording the Xe@water signal as a function of the RF pulse frequency train. 20 million cells in 500 µL media buffer of Ramos cells and Jurkat cells were prepared for the NMR experiment. Ramos and Jurkat cells were spun down and resuspended in 4 mL of binding buffer to a final cell density of $5x10^6$ cells/mL. The cell solution was mixed with 400 µL of 30 µM MS2-CryA-TD05.1 construct solutions and incubated on ice for 1 h with constant shaking. The cells were then washed twice with 10 mL binding buffer and washed once with 10 mL NMR media (RPMI 1640 supplemented with 1 % P/S, 1% L-Gln, and 0.02% L-81). The cells were then resuspended in 500 µL NMR media for the NMR experiment. dSNOB pulses (15, 29) with 500 Hz bandwidth was used with the same pulse sequence which was previously used (15, 30), except the saturation time was 8 s. (Figure 3-A) Contrasts with different saturation time were measured with saturation on and off pulses (6,300 Hz and 35,900 Hz) four times with 0, 3, 6, 9, 12, 15, 20 seconds, respectively (Figure 3-B) For ^{129}Xe Hyper-CEST saturation MRI, we used a custom phantom comprised of three 5 mm NMR tubes packed into a triangular configuration. This custom phantom could fit inside of a 10 mm NMR probe. Each tube had an individual gas capillary. Xenon images were acquired using a modified fast spin echo imaging sequence that included bubbling and waiting times as well as a saturation pulse prior to excitation as previously used (15). Total gas pressure was maintained at 2.44 atm and the flow rate was 0.4 SLM. The solution was typically bubbled for 10 s followed by a 6 s wait. The dSNOB pulse was 6.5 µs, a train of 4 echoes was used with an echo time of 10 ms, and the overall repetition time (TR) was 22.5 s. Signals were acquired with a 12.02 kHz spectral width and 2.66 ms acquisition time. All images were acquired in the axial orientation using 16 averages. The field of view was 20 mm by 20 mm. Xenon images had a k-space matrix

of dimensions 32 readout by 32 phase encode points. A ^{129}Xenon contrast map (Supporting Information Figure S3-c) was obtained using custom MATLAB scripts that apodized the signal using a 10 Hz exponential function. The k-space of off-resonance (Supporting Information Figure S3-b) was subtracted from the on-resonance (Supporting Information Figure S3-a) saturation images voxel-by-voxel. The subtracted image was then normalized by dividing it by the off-saturation image (Supporting Information Figure S3-c). The regions of interest defined by the proton image (Supporting Information Figure S3-d) was used to make the final ^{129}Xe contrast map (Supporting Information Figure S3-e). Significant ^{129}Xe contrast was only obtained in the Ramos cell solution.

The proton image was obtained using a fast spin echo imaging sequence (TR= 1.5 s, TE= 16.7 ms, 4 echoes per excitation) after 2 ms excitation. The k-space matrix dimension was 192 points in both readout and phase encode dimensions. The field of view was 20 mm by 20 mm. Signals were acquired with a 20.16 kHz spectral width and 9.52 ms acquisition time. All proton images were acquired using 4 averages.

7.6 Supporting information

General experimental procedures and materials

Unless otherwise noted, all chemicals and solvents were of analytical grade and used as received from commercial sources (Sigma Aldrich, USA). Water (dd-H_2O) used in biological procedures or as the reaction solvent was deionized using a NANOpure purification system (Barnstead, USA). All oligonucleotides were obtained from Integrated DNA Technologies (Coralville, IA). All cell culture reagents were obtained from Gibco/Invitrogen Corp. (Carlsbad, CA) unless otherwise noted. Cell culture was conducted using standard techniques. Jurkat and Ramos cells were grown in T-25 culture flasks (Corning) in RPMI Medium 1640 supplemented with 10% (v/v) fetal bovine serum (FBS, Omega Scientific) and 1% penicillin/streptomycin (P/S, Sigma). U266 cells were grown in T-25 culture flasks (Corning) in RPMI Medium 1640 supplemented with 15% (v/v) fetal bovine serum (FBS, Omega Scientific) and 1% penicillin/streptomycin (P/S, Sigma). Absorbance data were collected with Thermo Scientific Nanodrop 2000 spectrophotometer. ESI high resolution mass spectra were obtained in the QB3 Mass Spectrometry Facility using an LTQ orbitrap XL hybrid Mass spectrometer.

Synthesis of CryA Linker

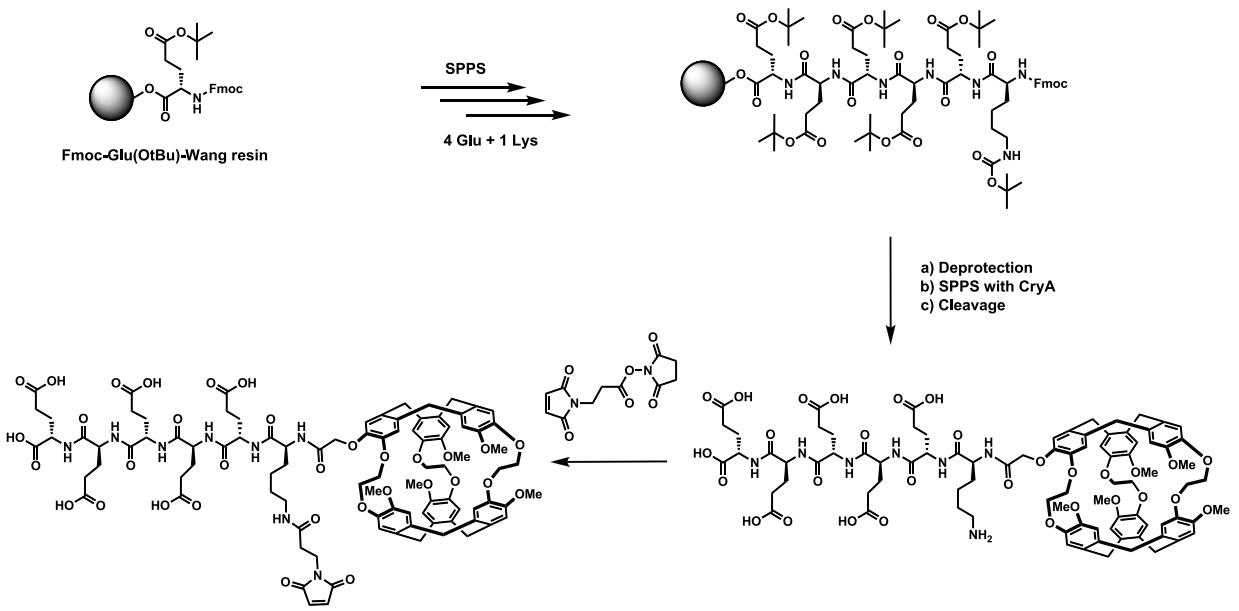

Figure S1. Scheme and structures for the synthesis of the CryA-maleimide Linker

Starting with Fmoc glutamic acid Wang resin (0.57 mmol/g, 100 mg, 57 µmol), standard Fmoc solid phase peptide synthesis was performed with the appropriate amino acid (5 equiv.), HCTU (*N*,*N*,*N'*,*N'*-tetramethyl-*O*-(6-chloro-1*H*-benzotriazol-1-yl) uronium hexafluorophosphate) (5 equiv.) and DIPEA (*N*,*N*-diisopropylethylamine) (10 equiv) in DMF (dimethylformamide) until full conversion was obtained, as observed by a Kaiser test (31). Deprotection of the Fmoc protecting groups was achieved with 20% piperidine in DMF for 15 min. After attaching 4 glutamic acids and one lysine to the resin, a 2-fold excess of cryptophane cage carboxylic acid (CryA, supplied by Kang Zhao, Tianjin University in China) was attached to the primary amine of the lysine group using the same coupling equivalents for 24 h. The product was cleaved using a mixture of trifluoroacetic acid : water : triisopropylsilane (95:2.5:2.5) for 3 h and precipitated with diethyl ether two times. The resulting material was purified by RP-HPLC using a C18 column with monitoring at 280 nm. The fractions containing the desired product were collected and lyophilized to yield ~2 mg. ESI-HRMS calculated for $C_{86}H_{102}N_7O_{30}$ $[M+H]^+$ 1712.6666 found 1712.6717. The maleimide-NHS ester (2,5-dioxopyrrolidin-1-yl 3-(2,5-dioxo-2,5-dihydro-1*H*-pyrrol-1-yl) propanoate) was synthesized as previously described (32). The CryA linker was dissolved in water (1 equiv.) and the pH was adjusted with sodium hydroxide. The maleimide-NHS ester was dissolved in DMF (10 equiv.). The solutions were mixed together 1:1 for 1 h and the resulting CryA-Mal linker was purified by RP-HPLC using a C18 column. MALDI-TOF calculated for $C_{93}H_{106}N_8O_{33}Na$ $[M+Na]^+$ 1885.6 found 1883.3.

Synthesis of pAF-N87C-MS2 Oregon Green

The *p*AF-N87C MS2 capsids were expressed and purified as previously reported (33). The plasmid containing the amber stop codon mutation in the MS2 coat protein was co-tranformed into DH10B cells with the pDULE plasmid containing the *p*AF aminoacyl tRNA synthetase and tRNA. The expression and purification were carried out following the published protocol.

Commercially available Oregon-Green-Maleimide (100 equiv.) was dissolved in DMF, and incubated with *p*AF-N87C-MS2 for 1 h. The reaction was validated by LC-MS (MS2 monomer's *m/z* is 13778, modified *m/z* is 15642). A commercially available TD05.1-5'-NH_2 aptamer was modified with aminophenol by reaction with aminophenol-NHS ester(34) and was purified using NAP-5, 10, and 25 columns (GE Healthcare). Reaction of aminophenol-TD05.1 with MS2 was performed according to the established procedure with sodium periodate as an oxidant. The degree of modification was confirmed by gel electrophoresis.

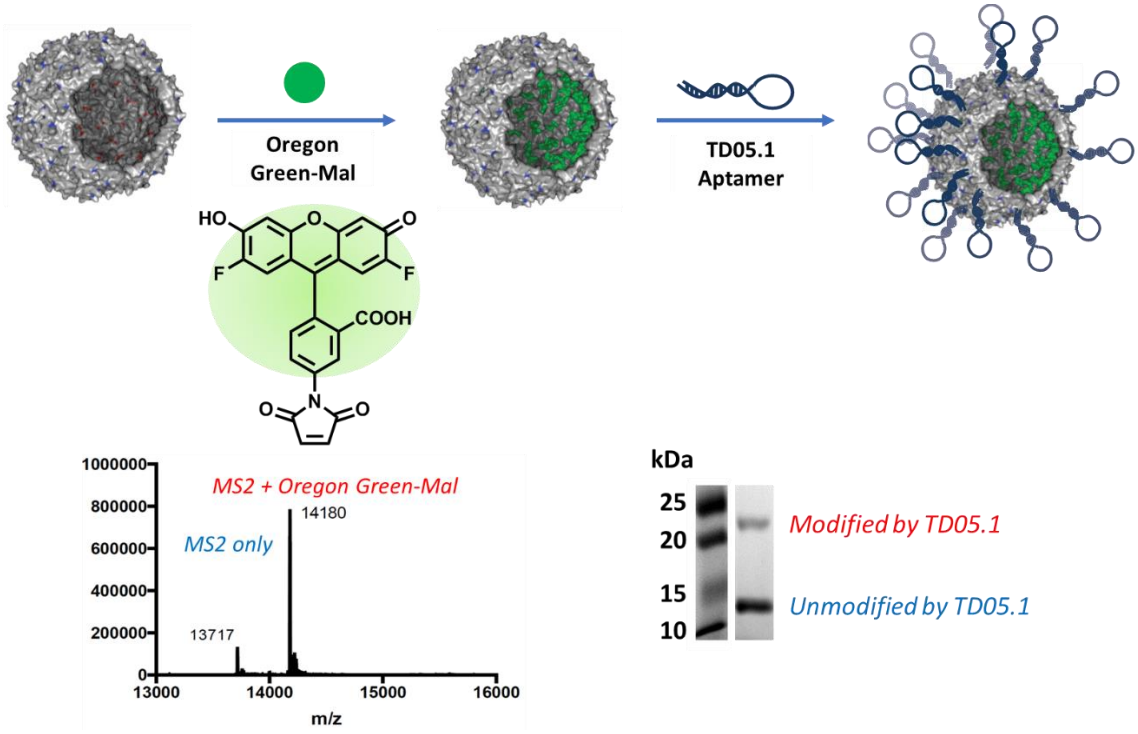

Figure S2. Schemes and structures for the synthesis of the pAF-N87C-MS2 Oregon Green

Analyzed ^{129}Xe NMR/MRI map

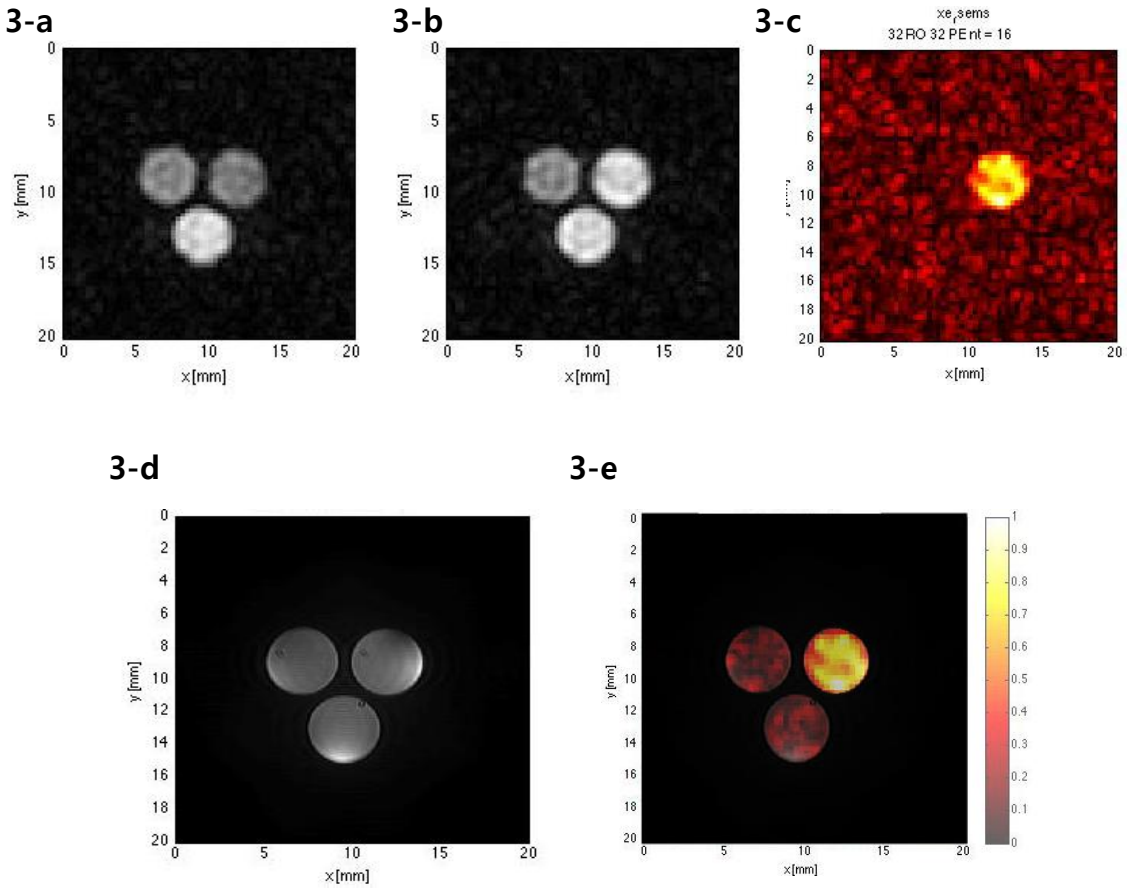

Figure S3. The three phantoms are 5-mm NMR tubes. Jurkat cells are on the left top tube in buffer (40 million cells / mL), and Ramos cells are on the right top tube in buffer (40 million cells / mL). The lower tube is the media control. The individual images are described in the main text.

Raw SDS-PAGE Gel Images

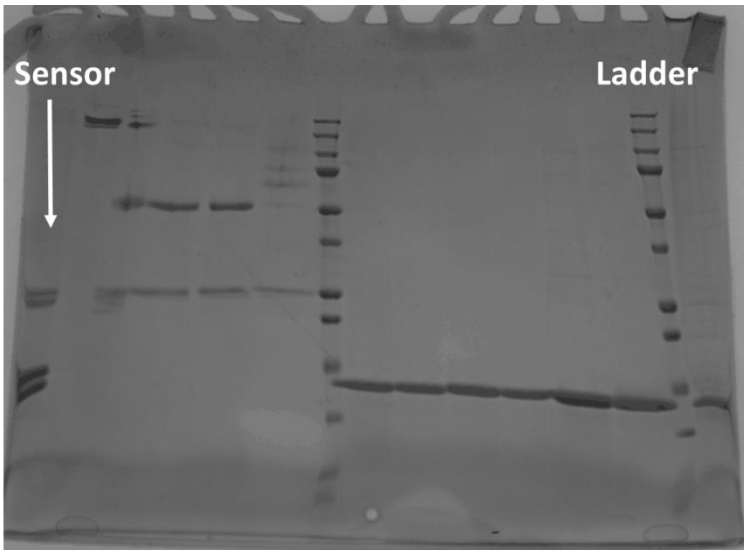

Figure S4. Raw SDS-PAGE gel image for Figure 1.

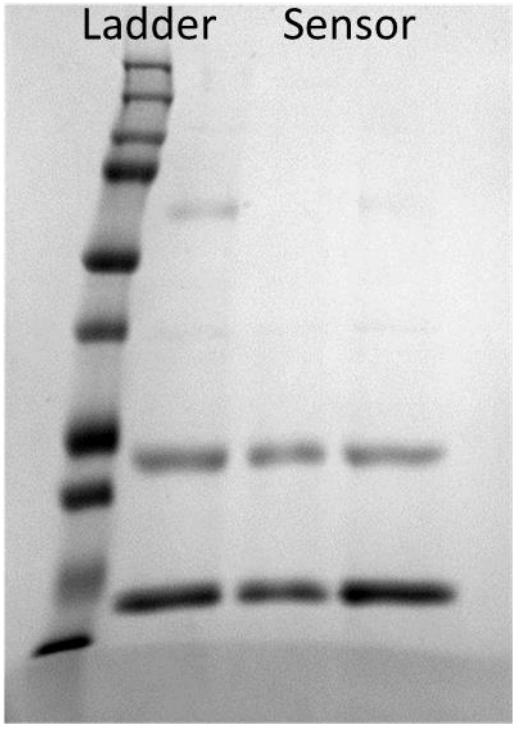

Figure S5. Raw SDS-PAGE gel image for Figure S2.

Biblography

Chapter1

1. Raftery, D. Annual Reports on NMR Spectroscopy 57 (Elsevier Academic Press Inc., 2006).

2. Walker, T. & Happer, W. Spin-exchange optical pumping of noble-gas nuclei. Rev. Mod. Phys. 69, 629–642 (1997).

3. Witte, C. & Schroeder, L. NMR of hyperpolarised probes. NMR Biomed. 26, 788–802 (2013).

4. Bouchiat, M., Carver, T. & Varnum, C. Nuclear polarization in He3 gas induced by optical pumping and dipolar exchange. Phys. Rev. Lett. 5, 373–375 (1960).

5. Reimer, J. A. Nuclear hyperpolarization in solids and the prospects for nuclear spintronics. Solid State NMR 37, 3–12 (2010).

6. Hayes, S. E., Mui, S. & Ramaswamy, K. Optically pumped nuclear magnetic resonance of semiconductors. J. Chem. Phys. 128, 052203 (2008).

7. Duckett, S. B. & Mewis, R. E. in Hyperpolarization Methods in NMR Spectroscopy Vol. 338 (ed. Kuhn, L. T.) 75–103 (Springer-Verlag, 2013).

8. Bowers, C. & Weitekamp, D. Transformation of symmetrization order to nuclear-spin magnetization by chemical reaction and nuclear magnetic resonance. Phys. Rev. Lett. 57, 2645–2648 (1986).

9. Natterer, J. & Bargon, J. Parahydrogen induced polarization. Prog. Nucl. Magn. Reson. Spectrosc. 31, 293–315 (1997).

10. Ni, Q. Z. et al. High frequency dynamic nuclear polarization. Acc. Chem. Res. 46, 1933–1941 (2013).

11. Griesinger, C. et al. Dynamic nuclear polarization at high magnetic fields in liquids. Prog. Nucl. Magn. Reson. Spectrosc. 64, 4–28 (2012).

12. Ardenkjaer-Larsen, J. et al. Increase in signal-to-noise ratio of410,000 times in liquid-state NMR. Proc. Natl Acad. Sci. USA 100, 10158–10163 (2003).

13. Gajan, D. et al. Hybrid polarizing solids for pure hyperpolarized liquids through dissolution dynamic nuclear polarization. Proc. Natl Acad. Sci. USA 111, 14693–14697 (2014).

14. Goez, M. An introduction to chemically induced dynamic nuclear polarization. Concept. Magn. Reson. 7, 69–86 (2005).

15. Tateishi, K. et al. Room temperature hyperpolarization of nuclear spins in bulk. Proc. Natl Acad. Sci. USA 111, 7527–7530 (2014).

16. King, J. P., Coles, P. J. & Reimer, J. A. Optical polarization of 13C nuclei in diamond through nitrogen vacancy centers. Phys. Rev. B 81, 073201 (2010).

17. Fischer, R., Jarmola, A., Kehayias, P. & Budker, D. Optical polarization of nuclear ensembles in diamond. Phys. Rev. B 87, 125207 (2013).

18. Wang, H. et al. Sensitive magnetic control of ensemble nuclear spin hyperpolarization in diamond. Nat. Commun. 4, 1940 (2013).

19. Fischer, R. et al. Bulk nuclear polarization enhanced at room-temperature by optical pumping. Phys. Rev. Lett. 111, 057601 (2013).

20. Doherty, M. W. et al. The nitrogen-vacancy colour centre in diamond. Phys. Rep. 528, 1–45 (2013).

21. A´ lvarez, G. A. et al. Local and bulk 13C hyperpolarization in nitrogen-vacancycentred diamonds at variable fields and orientations. Nat. Commun. 6, 8456 (2015).

22. Abrams, D., Trusheim, M. E., Englund, D. R., Shattuck, M. D. & Meriles, C. A. Dynamic nuclear spin polarization of liquids and gases in contact with nanostructured diamond. Nano Lett. 14, 2471–2478 (2014).

23. Reynhardt, E. & High, G. Dynamic nuclear polarization of diamond. I. Solid state and thermal mixing effects. J. Chem. Phys. 109, 4090–4099 (1998).

24. Abragam, A. Principles of Nuclear Magnetism (Oxford Univ. Press, 1961).

25. Pines, A., Gibby, M. G. & Waugh, J. Proton-enhanced NMR of dilute spins in solids. J. Chem. Phys 59, 569–590 (1973).

26. Slichter, C. P. Principles of Magnetic Resonance 3rd edn (Springer, 1996).

27. Gaede, H. et al. High-field cross-polarization NMR from laser-polarized xenon to surface nuclei. Appl. Magn. Reson. 8, 373–384 (1995).

28. Navon, G. et al. Enhancement of solution NMR and MRI with laser-polarized xenon. Science 271, 1848–1851 (1996).

29. Acosta, V. M. et al. Diamonds with a high density of nitrogen-vacancy centers for magnetometry applications. Phys. Rev. B 80, 115202 (2009).

30. Slichter, C. P., Principles of Magnetic Resonance. New York: Springer, 3rd ed., (1996)

31. Reynhardt E., and High, G., "Dynamic nuclear polarization of diamond. I. Solid state and thermal mixing effects," J. Chem. Phys., vol. 109, pp. 4090–4099, (1998)

32. Abragam, A., Principles of Nuclear Magnetism. Oxford: Oxford University Press, (1961)

33. Vanhouten, J., Wenckebach, W. T., and Poulis, N. J. "A study of the thermal contact between the nuclear zeeman system and the electron dipole-dipole interaction system," Physica B and C, vol. 92, no. 2, pp. 210–220, (1977)

34. King, J. P., Coles, P. J. and Reimer J. A., "Optical polarization of 13C nuclei in diamond through nitrogen vacancy centers," Phys. Rev. B., vol. 81, 073201, (2010)

35. Hovav, Y., Feintuch, A., and Vega, S. "Theoretical aspects of dynamic nuclear polarization in the solid state – spin temperature and thermal mixing," Phys. Chem. Chem. Phys., vol. 15, no. 1, pp. 188–203, (2013)

36. Acosta, V. M., Bauch, E., Ledbetter, M. P., Waxman, A., Bouchard, L. -S., and Budker, D. "Temperature Dependence of the Nitrogen-Vacancy Magnetic Resonance in Diamond," Phys. Rev. Lett., vol. 104, 070801, (2010)

Chapter 2

1. Abragam, A. & Goldman, M. Principles of dynamic nuclear polarisation. Reports Prog. Phys. 41, 395–467 (1978).

2. Ni, Q. Z. et al. High frequency dynamic nuclear polarization. Acc. Chem. Res. 46, 1933–41 (2013).

3. Becerra, L., Gerfen, G., Temkin, R., Singel, D. & Griffin, R. Dynamic nuclear polarization with a cyclotron resonance maser at 5 T. Phys. Rev. Lett. 71, 3561–3564 (1993).

4. Gumann, P. et al. Inductive measurement of optically hyperpolarized phosphorous donor nuclei in an isotopically enriched silicon-28 crystal. Phys. Rev. Lett. 113, 267604 (2014).

5. Maly, T. et al. Dynamic nuclear polarization at high magnetic fields. J. Chem. Phys. 128, 052211 (2008).

6. Thurber, K. R., Yau, W.-M. & Tycko, R. Low-temperature dynamic nuclear polarization at 9.4 T with a 30 mW microwave source. J. Magn. Reson. 204, 303–13 (2010).

7. Doherty, M. W. et al. The nitrogen-vacancy colour centre in diamond. Phys. Rep. 528, 1–45 (2013).

8. Álvarez, G. A. et al. Local and bulk ^{13}C hyperpolarization in nitrogen-vacancy-centred diamonds at variable fields and orientations. Nat. Commun. 6, 8456 (2015).

9. Fischer, R. et al. Bulk nuclear polarization enhanced at room temperature by optical pumping. Phys. Rev. Lett. 111, 057601 (2013).

10. Jacques, V. et al. Dynamic polarization of single nuclear spins by optical pumping of nitrogen-vacancy color centers in diamond at room temperature. Phys. Rev. Lett. 102, 057403 (2009).

11. Wang, H.-J. et al. Sensitive magnetic control of ensemble nuclear spin hyperpolarization in diamond. Nat. Commun. 4, 1940 (2013).

12. King, J. P. et al. Room-temperature in situ nuclear spin hyperpolarization from optically pumped nitrogen vacancy centres in diamond. Nat. Commun. 6, 8965 (2015).

13. Rej, E., Gaebel, T., Boele, T., Waddington, D. E. J. & Reilly, D. J. Hyperpolarized nanodiamond with long spin-relaxation times. Nat. Commun. 6, 8459 (2015).

14. Scheuer, J. et al. Optically induced dynamic nuclear spin polarisation in diamond. New J. Phys. 18, 013040 (2016).

15. Dutta, P., Martinez, G. V & Gillies, R. J. Nanodiamond as a New Hyperpolarizing Agent and Its ^{13}C MRS. J. Phys. Chem. Lett. 5, 597–600 (2014).

16. Abrams, D., Trusheim, M. E., Englund, D. R., Shattuck, M. D. & Meriles, C. A. Dynamic nuclear spin polarization of liquids and gases in contact with nanostructured diamond. Nano Lett. 14, 2471–8 (2014).

17. Felton, S. et al. Hyperfine interaction in the ground state of the negatively charged nitrogen vacancy center in diamond. Phys. Rev. B 79, 075203 (2009).

18. Smeltzer, B., Childress, L. & Gali, A. 13 C hyperfine interactions in the nitrogen-vacancy centre in diamond. New J. Phys. 13, 025021 (2011).

19. Parker, A. J., Wang, H.-J., Li, Y., Pines, A. & King, J. P. Decoherence-protected transitions of nitrogen vacancy centers in 99% 13C-enriched diamond. 21 (2015). at <http://arxiv.org/abs/1506.05484>

20. Gali, A. Identification of individual C 13 isotopes of nitrogen-vacancy center in diamond by combining the polarization studies of nuclear spins and first-principles calculations. Phys. Rev. B 80, 241204 (2009).

21. Lefmann, K. et al. NMR spectra of pure C 13 diamond. Phys. Rev. B 50, 15623–15627 (1994).

Chapter 3

1. Rondin, L. et al. Magnetometry with nitrogen-vacancy defects in diamond. Rep. Prog. Phys. 77, 056503 (2014).

2. Dutta, P., Martinez, G. V & Gillies, R. J. Nanodiamond as a New Hyperpolarizing Agent and Its ^{13}C MRS. J. Phys. Chem. Lett. 5, 597–600 (2014).

3. Rej, E., Gaebel, T., Boele, T., Waddington, D. E. J. & Reilly, D. J. Hyperpolarized nanodiamond with long spin-relaxation times. Nat. Commun. 6, 8459 (2015).

4. Doherty, M. W. et al. The nitrogen-vacancy colour centre in diamond. Phys. Rep. 528, 1–45 (2013).

5. Álvarez, G. A. et al. Local and bulk ^{13}C hyperpolarization in nitrogen-vacancy-centred diamonds at variable fields and orientations. Nat. Commun. 6, 8456 (2015).

6. Fischer, R. et al. Bulk nuclear polarization enhanced at room temperature by optical pumping. Phys. Rev. Lett. 111, 057601 (2013).

7. King, J. P. et al. Room-temperature in situ nuclear spin hyperpolarization from optically pumped nitrogen vacancy centres in diamond. Nat. Commun. 6, 8965 (2015).

8. Wang, H.-J. et al. Sensitive magnetic control of ensemble nuclear spin hyperpolarization in diamond. Nat. Commun. 4, 1940 (2013).

9. Abrams, D., Trusheim, M. E., Englund, D. R., Shattuck, M. D. & Meriles, C. A. Dynamic nuclear spin polarization of liquids and gases in contact with nanostructured diamond. Nano Lett. 14, 2471–8 (2014).

10. Chen, Q., Schwarz, I., Jelezko, F., Retzker, A. & Plenio, M. B. Optical hyperpolarization of ^{13}C nuclear spins in nanodiamond ensembles. Phys. Rev. B 92, 184420 (2015).

11. Scott, E., Drake, M. & Reimer, J. A. The phenomenology of optically pumped ^{13}C NMR in diamond at 7.05T: Room temperature polarization, orientation dependence, and the effect of defect concentration on polarization dynamics. J. Magn. Reson. 264, 154–62 (2016).

12. Parker, A. J., Wang, H.-J., Li, Y., Pines, A. & King, J. P. Decoherence-protected transitions of nitrogen vacancy centers in 99% 13C-enriched diamond. 21 (2015). at <http://arxiv.org/abs/1506.05484>

13. CP Slichter; Principles of Magnetic Resonance. (3rd. ed.) Springer, Berlin (1990)

Chapter 4

1. D. T. Quang, J. S. Kim, Chem. Rev. 2010, 110, 6280–6301.

2. Y. W. Choi, G. J. Park, Y. J. Na, H. Y. Jo, S. A. Lee, G. R. You, C. Kim, Sens. Actuators B 2014, 194, 343–352.

3. E. Nieboer, D. H. Richardson, Environ. Pollut. Ser. B 1980, 1, 3–26.

4. L. Cui, J. Wu, H. Ju, Biosens. Bioelectron. 2015, 63, 276–286.

5. A.-M. Oros, N. J. Shah, Phys. Med. Biol. 2004, 49, R105.

6. a) M. L. Mazzanti, R. P. Walvick, X. Zhou, Y. Sun, N. Shah, J. Mansour, J. Gereige, M. S. Albert, PLoS One 2011, 6, e21607; b) R. Xu, J. Ohya, L. Luo, Segmentation of Brain MRI, INTECH Open Access Publisher, 2012. c) R. T. Branca, T. He, L. Zhang, C. S. Floyd, M. Freeman, C. White, A. Burant, Proc. Natl. Acad. Sci. USA 2014, 111, 18001–18006.

7. a) A. Schlundt, W. Kilian, M. Beyermann, J. Sticht, S. Gìnther, S. Hçpner, K. Falk, O. Roetzschke, L. Mitschang, C. Freund, Angew. Chem. Int. Ed. 2009, 48, 4142–4145; Angew. Chem. 2009, 121, 4206–4209; b) T. J. Lowery, S. Garcia, L. Chavez, E. J. Ruiz, T. Wu, T. Brotin, J. P. Dutasta, D. S. King, P. G. Schultz, A. Pines, ChemBioChem 2006, 7, 65–73; c) M. M. Spence, E. J. Ruiz, S. M. Rubin, T. J. Lowery, N. Winssinger, P. G. Schultz, D. E. Wemmer, A. Pines, J. Am. Chem. Soc. 2004, 126, 15287–15294.

8. Q. Wei, G. K. Seward, P. A. Hill, B. Patton, I. E. Dimitrov, N. N. Kuzma, I. J. Dmochowski, J. Am. Chem. Soc. 2006, 128, 13274–13283.

9. V. Roy, T. Brotin, J. P. Dutasta, M. H. Charles, T. Delair, F. Mallet, G. Huber, H. Desvaux, Y. Boulard, P. Berthault, ChemPhysChem 2007, 8, 2082 – 2085.

10. L. Schrçder, T. J. Lowery, C. Hilty, D. E. Wemmer, A. Pines, Science 2006, 314, 446–449.

11. L. Schrçder, Physica Medica 2013, 29, 3–16.

12. J. Zhang, W. Jiang, Q. Luo, X. Zhang, Q. Guo, M. Liu, X. Zhou, Talanta 2014, 122, 101–105.

13. N. Kotera, N. Tassali, E. L¦once, C. Boutin, P. Berthault, T. Brotin, J. P. Dutasta, L. Delacour, T. Traor¦, D. A. Buisson, Angew. Chem. Int. Ed. 2012, 51, 4100–4103; Angew. Chem. 2012, 124, 4176–4179.

14. N. Tassali, N. Kotera, C. L. Boutin, E. L¦once, Y. Boulard, B. Rousseau, E. Dubost, F. d. r. Taran, T. Brotin, J.-P. Dutasta, Anal. Chem. 2014, 86, 1783 – 1788.

15. a) H. Maumela, R. D. Hancock, L. Carlton, J. H. Reibenspies, K. P. Wainwright, J. Am. Chem. Soc. 1995, 117, 6698–6707; b) E. L. Que, D. W. Domaille, C. J. Chang, Chem. Rev. 2008, 108, 1517–1549; c) N. Viola-Villegas, R. P. Doyle, Coord. Chem. Rev. 2009, 253, 1906–1925.

16. a) A. Heppeler, J. P. Andr¦, I. Buschmann, X. Wang, J. C. Reubi, M. Hennig, T. A. Kaden, H. R. Maecke, Chem. Eur. J. 2008, 14, 3026–3034; b) F. Benetollo, G. Bombieri, L. Calabi, S. Aime, M. Botta, Inorg. Chem. 2003, 42, 148–157.

17. K. K. Palaniappan, R. M. Ramirez, V. S. Bajaj, D. E. Wemmer, A. Pines, M. B. Francis, Angew. Chem. Int. Ed. 2013, 52, 4849–4853; Angew. Chem. 2013, 125, 4949

18. C. Witte, L. Schrçder, NMR Biomed. 2013, 26, 788–802.

19. S. Aime, M. Botta, M. Fasano, M. P. M. Marques, C. F. Geraldes, D. Pubanz, A. E. Merbach, Inorg. Chem. 1997, 36, 2059–2068.

20. a) D. N. Sears, C. J. Jameson, J. Chem. Phys. 2003, 119, 12231–12244; b) E. J. Ruiz, D. N. Sears, A. Pines, C. J. Jameson, J. Am. Chem. Soc. 2006, 128, 16980–16988.

21. I. Ruset, S. Ketel, F. Hersman, Phys. Rev. Lett. 2006, 96, 053002.

22. P. Nikolaou, A. M. Coffey, L. L. Walkup, B. M. Gust, N. Whiting, H. Newton, S. Barcus, I. Muradyan, M. Dabaghyan, G. D. Moroz, M. S. Rosen, S. Patz, M. J. Barlow, E. Y. Chekmenev, B. M. Goodson, Proc. Natl. Acad. Sci. USA 2013, 110, 14150–14155.

23. B. Driehuys, J. Pollaro, G. P. Cofer, Magn. Reson. Med. 2008, 60, 14–20.

Chapter 5

1. Lee, H., Sun, E., Ham, D. & Weissleder, R. Chip-NMR biosensor for detection and molecular analysis of cells. Nat. Med. 14, 869–74 (2008).

2. Wei, Q. et al. Designing ^{129}Xe NMR biosensors for matrix metalloproteinase detection. J. Am. Chem. Soc. 128, 13274–13283 (2006).

3. Schröder, L., Lowery, T. J., Hilty, C., Wemmer, D. E. & Pines, A. Molecular imaging using a targeted magnetic resonance hyperpolarized biosensor. Science 314, 446–9 (2006).

4. Mynar, J. L., Lowery, T. J., Wemmer, D. E., Pines, A. & Fréchet, J. M. J. Xenon biosensor amplification via dendrimer-cage supramolecular constructs. J. Am. Chem. Soc. 128, 6334–5 (2006).

5. Ghazani, A. a et al. Comparison of select cancer biomarkers in human circulating and bulk tumor cells using magnetic nanoparticles and a miniaturized micro-NMR system. Nanomedicine 9, 1009–17 (2013).

6. Kunth, M., Döpfert, J., Witte, C., Rossella, F. & Schröder, L. Optimized use of reversible binding for fast and selective NMR localization of caged xenon. Angew. Chemie - Int. Ed. 51, 8217–8220 (2012).

7. Lee, Y. J., Park, K.-D., Huang, S.-J., Liu, S.-B. & Lee, H.-J. Characterization of nanoporous structures of polyphenylene oxide derived carbon membranes by means of ^{129}Xe NMR. J. Nanosci. Nanotechnol. 7, 3932–7 (2007).

8. Schröder, L. Xenon for NMR biosensing--inert but alert. Phys. Med. 29, 3–16 (2013).

9. Driehuys, B. et al. Imaging alveolar-capillary gas transfer using hyperpolarized ^{129}Xe MRI. Proc. Natl. Acad. Sci. U. S. A. 103, 18278–83 (2006).

10. Cleveland, Z. I. et al. Hyperpolarized ^{129}Xe MR imaging of alveolar gas uptake in humans. PLoS One 5, e12192 (2010).

11. Xu, X. et al. Hyperpolarized ^{129}Xe gas lung MRI-SNR and T2 * comparisons at 1.5 T and 3 T. Magn. Reson. Med. 68, 1900–1904 (2012).

12. Mazzanti, M. L. et al. Distribution of hyperpolarized xenon in the brain following sensory stimulation: preliminary MRI findings. PLoS One 6, e21607 (2011).

13. Swanson, S. D. et al. Brain MRI with laser-polarized ^{129}Xe. Magn. Reson. Med. 38, 695–698 (1997).

14. Swanson, S. D., Rosen, M. S., Coulter, K. P., Welsh, R. C. & Chupp, T. E. Distribution and dynamics of laser-polarized ^{129}Xe magnetization in vivo. Magn. Reson. Med. 42, 1137–1145 (1999).

15. Spence, M. M. et al. Functionalized xenon as a biosensor. Proc. Natl. Acad. Sci. U. S. A. 98, 10654–7 (2001).

16. Spence, M. M. et al. Development of a functionalized xenon biosensor. J. Am. Chem. Soc. 126, 15287–94 (2004).

17. Lowery, T. J. et al. Optimization of xenon biosensors for detection of protein interactions. Chembiochem 7, 65–73 (2006).

18. Roy, V. et al. A cryptophane biosensor for the detection of specific nucleotide targets through xenon NMR spectroscopy. Chemphyschem 8, 2082–5 (2007).

19. Chambers, J. M. et al. Cryptophane xenon-^{129} nuclear magnetic resonance biosensors targeting human carbonic anhydrase. J. Am. Chem. Soc. 131, 563–9 (2009).

20. Schlundt, A. et al. A xenon-129 biosensor for monitoring MHC-peptide interactions. Angew. Chem. Int. Ed. Engl. 48, 4142–5 (2009).

21. Seward, G. K., Bai, Y., Khan, N. S. & Dmochowski, I. J. Cell-compatible, integrin-targeted cryptophane-^{129}Xe NMR biosensors. Chem. Sci. 2, 1103 (2011).

22. Boutin, C. et al. Cell uptake of a biosensor detected by hyperpolarized ^{129}Xe NMR: The transferrin case. Bioorganic Med. Chem. 19, 4135–4143 (2011).

23. Schröder, L. et al. Temperature Response of ^{129}Xe Depolarization Transfer and Its Application for Ultrasensitive NMR Detection. Phys. Rev. Lett. 100, 257603 (2008).

24. Taratula, O. & Dmochowski, I. J. Functionalized ^{129}Xe contrast agents for magnetic resonance imaging. Curr. Opin. Chem. Biol. 14, 97–104 (2010).

25. Rose, H. M. et al. Development of an antibody-based, modular biosensor for ^{129}Xe NMR molecular imaging of cells at nanomolar concentrations. Proc. Natl. Acad. Sci. U. S. A. 20–23 (2014).

26. Hou, J. et al. Synthesis of novel folate conjugated fluorescent nanoparticles for tumor imaging. J. Biomed. Mater. Res. A 99, 684–9 (2011).

27. Dong, H. et al. Target-cell-specific delivery, imaging, and detection of intracellular microRNA with a multifunctional SnO2 nanoprobe. Angew. Chem. Int. Ed. Engl. 51, 4607–12 (2012).

28. Asati, A., Kaittanis, C., Santra, S. & Perez, J. M. pH-tunable oxidase-like activity of cerium oxide nanoparticles achieving sensitive fluorigenic detection of cancer biomarkers at neutral pH. Anal. Chem. 83, 2547–53 (2011).

29. Liu, J.-M., Chen, J.-T. & Yan, X.-P. Near infrared fluorescent trypsin stabilized gold nanoclusters as surface plasmon enhanced energy transfer biosensor and in vivo cancer imaging bioprobe. Anal. Chem. 85, 3238–45 (2013).

30. Wang, S. & Low, P. S. Folate-mediated targeting of antineoplastic drugs, imaging agents, and nucleic acids to cancer cells. J. Control. Release 53, 39–48 (1998).

31. Assaraf, Y. G., Leamon, C. P. & Reddy, J. A. The folate receptor as a rational therapeutic target for personalized cancer treatment. Drug Resist. Updat. 17, 89–95 (2014).

32. Masters, J. R. HeLa cells 50 years on: the good, the bad and the ugly. Nat. Rev. Cancer 2, 315–9 (2002).

33. Wang, H. et al. Self-assembled nanospheres as a novel delivery system for taxol: a molecular hydrogel with nanosphere morphology. Chem. Commun. 47, 4439–41 (2011).

34. Shapiro, M. G. et al. Genetically encoded reporters for hyperpolarized xenon magnetic resonance imaging. Nat. Chem. 6, 629–634 (2014).

35. Kruger, S. J. et al. Functional imaging of the lungs with gas agents. J. Magn. Reson. Imaging 43, 295–315 (2016).

36. Liszewski, M. C. et al. Magnetic resonance imaging of pediatric lung parenchyma, airways, vasculature, ventilation, and perfusion: state of the art. Radiol. Clin. North Am. 51, 555–82 (2013).

37. Mugler, J. P. & Altes, T. A. Hyperpolarized ^{129}Xe MRI of the human lung. J. Magn. Reson. Imaging 37, 313–31 (2013).

38. Kaiser, E., Colescott, R. L., Bossinger, C. D. & Cook, P. I. Color test for detection of free terminal amino groups in the solid-phase synthesis of peptides. Anal. Biochem. 34, 595–598 (1970).

39. Wang, H. et al. Self-assembled nanospheres as a novel delivery system for taxol: a molecular hydrogel with nanosphere morphology. Chem. Commun. 47, 4439–41 (2011).

40. Jeong, K. et al. Investigation of DOTA-Metal Chelation Effects on the Chemical Shift of (129) Xe. ChemPhysChem 16, 3573–7 (2015).

41. Shapiro, M. G. et al. Genetically encoded reporters for hyperpolarized xenon magnetic resonance imaging. Nat. Chem. 6, 629–634 (2014).

Chapter 6

1. FOWLER, A. M. Increases in estrogen receptor- concentration in breast cancer cells promote serine 118/104/106-independent AF-1 transactivation and growth in the absence of estrogen. FASEB J. 18, 81–93 (2004).

2. Peterson, L. M. et al. Quantitative imaging of estrogen receptor expression in breast cancer with PET and 18F-fluoroestradiol. J Nucl Med 49, 367–374 (2008).

3. Dixit, M., Shi, J., Wei, L., Afari, G. & Bhattacharyya, S. Synthesis of Clinical-Grade [(18)F]-Fluoroestradiol as a Surrogate PET Biomarker for the Evaluation of Estrogen Receptor-Targeting Therapeutic Drug. Int. J. Mol. Imaging 2013, 278607 (2013).

4. Rijks, L. J. et al. Imaging of estrogen receptors in primary and metastatic breast cancer patients with iodine-123-labeled Z-MIVE. J. Clin. Oncol. 15, 2536–45 (1997).

5. Kiesewetter, D. O. et al. Preparation of four fluorine- 18-labeled estrogens and their selective uptakes in target tissues of immature rats. J. Nucl. Med. 25, 1212–1221 (1984).

6. Zhou, D. et al. Optimization of the preparation of fluorine-18-labeled steroid receptor ligands 16alpha-[18F]fluoroestradiol (FES), [18F]fluoro furanyl norprogesterone (FFNP), and 16beta-[18F]fluoro-5alpha-dihydrotestosterone (FDHT) as radiopharmaceuticals. J. Label. Compd. Radiopharm. 57, 371–377 (2014).

7. Ramesh, C. et al. Linkage effects on binding affinity and activation of GPR30 and estrogen receptors ERalpha/beta with tridentate pyridin-2-yl hydrazine tricarbonyl-Re/(99m)Tc(I) chelates. J. Am. Chem. Soc. 128, 14476–7 (2006).

8. Jackson, A., Davis, J., Pither, R. J., Rodger, A. & Hannon, M. J. Estrogen-Derived Steroidal Metal Complexes: Agents for Cellular Delivery of Metal Centers to Estrogen Receptor-Positive Cells. Inorg. Chem. 40, 3964–3973 (2001).

9. Kelloff, G. J. et al. The progress and promise of molecular imaging probes in oncologic drug development. Clin. Cancer Res. 11, 7967–7985 (2005).

10. Oliveira, M. C., Neto, C., Ribeiro, M. G. & Thiemann, T. Steroid receptor ligands for breast cancer targeting: an insight into their potential role as PET imaging agents. Curr.Med.Chem. 20, 222–245 (2013).

11. Gunanathan, C. et al. Water-soluble contrast agents targeted at the estrogen receptor for molecular magnetic resonance imaging. Bioconjug. Chem. 18, 1361–1365 (2007).

12. Li, M. J. et al. Structure of estradiol metal chelate and estrogen receptor complex: the basis for designing a new class of selective estrogen receptor modulators. J. Med. Chem. 54, 3575–3580 (2011).

13. Pais, A., Biton, I. E., Margalit, R. & Degani, H. Characterization of estrogen-receptor-targeted contrast agents in solution, breast cancer cells, and tumors in vivo. Magn. Reson. Med. 70, 193–206 (2013).

14. Pais, A. et al. In vivo magnetic resonance imaging of the estrogen receptor in an orthotopic model of human breast cancer. Cancer Res. 71, 7387–97 (2011).

15. Taratula, O. & Dmochowski, I. J. Functionalized ^{129}Xe contrast agents for magnetic resonance imaging. Curr. Opin. Chem. Biol. 14, 97–104 (2010).

16. Palaniappan, K. K., Francis, M. B., Pines, A. & Wemmer, D. E. Molecular Sensing Using Hyperpolarized Xenon NMR Spectroscopy. Isr. J. Chem. 54, 104–112 (2014).

17. Jeong, K. et al. Investigation of DOTA-Metal Chelation Effects on the Chemical Shift of ^{129} Xe. ChemPhysChem 16, 3573–7 (2015).

18. Spence, M. M. et al. Development of a functionalized xenon biosensor. J. Am. Chem. Soc. 126, 15287–94 (2004).

19. Seward, G. K., Bai, Y., Khan, N. S. & Dmochowski, I. J. Cell-compatible, integrin-targeted cryptophane-^{129}Xe NMR biosensors. Chem. Sci. 2, 1103 (2011).

20. Wei, Q. et al. Designing ^{129}Xe NMR biosensors for matrix metalloproteinase detection. J. Am. Chem. Soc. 128, 13274–13283 (2006).

21. Chambers, J. et al. Cryptophane Xenon^{129} Nuclear Magnetic Resonance Biosensors Targeting Human Carbonic Anhydrase. J. Am. Chem. Soc. 131, 563–569 (2008).

22. Schlundt, A. et al. A xenon^{129} biosensor for monitoring MHC-peptide interactions. Angew. Chem. Int. Ed. Engl. 48, 4142–5 (2009).

23. Boutin, C. et al. Cell uptake of a biosensor detected by hyperpolarized ^{129}Xe NMR: The transferrin case. Bioorganic Med. Chem. 19, 4135–4143 (2011).

24. Rose, H. M. et al. Development of an antibody-based, modular biosensor for ^{129}Xe NMR molecular imaging of cells at nanomolar concentrations. Proc. Natl. Acad. Sci. U. S. A. 20–23 (2014).

25. Palaniappan, K. K. et al. Molecular imaging of cancer cells using a bacteriophage-based ^{129}Xe NMR biosensor. Angew. Chemie - Int. Ed. 52, 4849–4853 (2013).

26. Blair, R. M. The Estrogen Receptor Relative Binding Affinities of 188 Natural and Xenochemicals: Structural Diversity of Ligands. Toxicol. Sci. 54, 138–153 (2000).

27. Gryder, B. E. et al. Histone deacetylase inhibitors equipped with estrogen receptor modulation activity. J. Med. Chem. 56, 5782–96 (2013).

28. Leduc, A.-M. et al. Helix-stabilized cyclic peptides as selective inhibitors of steroid receptor-coactivator interactions. Proc. Natl. Acad. Sci. U. S. A. 100, 11273–8 (2003).

29. Liebold, C., List, F., Kalbitzer, H. R., Sterner, R. & Brunner, E. The interaction of ammonia and xenon with the imidazole glycerol phosphate synthase from Thermotoga maritima as detected by NMR spectroscopy. Protein Sci. 19, 1774–82 (2010).

30. Zhang, J. et al. Rational design of hyperpolarized xenon NMR molecular sensor for the selective and sensitive determination of zinc ions. Talanta 122, 101–5 (2014).

31. Tassali, N. et al. Smart detection of toxic metal ions, Pb^{2+} and Cd^{2+}, using a ^{129}Xe NMR-based sensor. Anal. Chem. 86, 1783–8 (2014).

32. Cao, S., Hudnall, S. D., Kohen, F. & Lu, L. J. Measurement of estrogen receptors in intact cells by flow cytometry. Cytometry 41, 109–14 (2000).

33. Segner, H. et al. Identification of endocrine-disrupting effects in aquatic vertebrates and invertebrates: report from the European IDEA project. Ecotoxicol. Environ. Saf. 54, 302–314 (2003).

34. Petrović, M., Hernando, M. D., Díaz-Cruz, M. S. & Barceló, D. Liquid chromatography–tandem mass spectrometry for the analysis of pharmaceutical residues in environmental samples: a review. J. Chromatogr. A 1067, 1–14 (2005).

35. Mottaleb, M. A. et al. Gas chromatography-mass spectrometry screening methods for select UV filters, synthetic musks, alkylphenols, an antimicrobial agent, and an insect repellent in fish. J. Chromatogr. A 1216, 815–23 (2009).

36. Hooker, J. M., Esser-Kahn, A. P. & Francis, M. B. Modification of aniline containing proteins using an oxidative coupling strategy. J. Am. Chem. Soc. 128, 15558–9 (2006).

37. Schröder, L. Xenon for NMR biosensing--inert but alert. Phys. Med. 29, 3–16 (2013).

38. Jeong, K. et al. Investigation of DOTA-Metal Chelation Effects on the Chemical Shift of ^{129}Xe. ChemPhysChem. 16, 3573-3577 (2015).

39. Palaniappan, K. K. et al. Molecular imaging of cancer cells using a bacteriophage-based ^{129}Xe NMR biosensor. Angew. Chemie - Int. Ed. 52, 4849–4853 (2013).

Chapter 7

1. Lee, H., Sun, E., Ham, D. & Weissleder, R. Chip-NMR biosensor for detection and molecular analysis of cells. Nat. Med. 14, 869–874 (2008).

2. Lee, Y. J., Park, K.-D., Huang, S.-J., Liu, S.-B. & Lee, H.-J. Characterization of nanoporous structures of polyphenylene oxide derived carbon membranes by means of ^{129}Xe NMR. J. Nanosci. Nanotechnol. 7, 3932–3937 (2007).

3. Schroder, L., Lowery, T. J., Hilty, C., Wemmer, D. E. & Pines, A. Molecular Imaging Using a Targeted Magnetic Resonance Hyperpolarized Biosensor. Science (80). 314, 446–449 (2006).

4. Schröder, L. Xenon for NMR biosensing--inert but alert. Phys. Med. 29, 3–16 (2013).

5. Driehuys, B. et al. Imaging alveolar-capillary gas transfer using hyperpolarized ^{129}Xe MRI. Proc. Natl. Acad. Sci. U. S. A. 103, 18278–83 (2006).

6. Stewart, N. J., Norquay, G., Griffiths, P. D. & Wild, J. M. Feasibility of human lung ventilation imaging using highly polarized naturally abundant xenon and optimized three-dimensional steady-state free precession. Magn. Reson. Med. 74, 346–52 (2015).

7. Mazzanti, M. L. et al. Distribution of hyperpolarized xenon in the brain following sensory stimulation: preliminary MRI findings. PLoS One 6, e21607 (2011).

8. Swanson, S. D. et al. Brain MRI with laser-polarized ^{129}Xe. Magn. Reson. Med. 38, 695–698 (1997).

9. Swanson, S. D., Rosen, M. S., Coulter, K. P., Welsh, R. C. & Chupp, T. E. Distribution and dynamics of laser-polarized ^{129}Xe magnetization in vivo. Magn. Reson. Med. 42, 1137–1145 (1999).

10. Kunth, M., Döpfert, J., Witte, C., Rossella, F. & Schröder, L. Optimized use of reversible binding for fast and selective NMR localization of caged xenon. Angew. Chemie - Int. Ed. 51, 8217–8220 (2012).

11. Schröder, L. et al. Temperature Response of Xe129 Depolarization Transfer and Its Application for Ultrasensitive NMR Detection. Phys. Rev. Lett. 100, 257603 (2008).

12. Taratula, O. & Dmochowski, I. J. Functionalized ^{129}Xe contrast agents for magnetic resonance imaging. Curr. Opin. Chem. Biol. 14, 97–104 (2010).

13. Farkas, M. E. et al. PET Imaging and Biodistribution of Chemically Modified Bacteriophage MS2. Mol. Pharm. 10, 69–76 (2013).

14. Meldrum, T. et al. A xenon-based molecular sensor assembled on an MS2 viral capsid scaffold. J. Am. Chem. Soc. 132, 5936–5937 (2010).

15. Palaniappan, K. K. et al. Molecular Imaging of Cancer Cells Using a Bacteriophage-Based ^{129}Xe NMR Biosensor. Angew. Chem. Int. Ed. Engl. 125, 1–6 (2013).

16. Tong, G. J., Hsiao, S. C., Carrico, Z. M. & Francis, M. B. Viral capsid DNA aptamer conjugates as multivalent cell-targeting vehicles. J. Am. Chem. Soc. 131, 11174–8 (2009).

17. Wang, L. & Schultz, P. G. Expanding the genetic code. Angew. Chem. Int. Ed. Engl. 44, 34–66 (2004).

18. Mehl, R. a. et al. Generation of a bacterium with a 21 amino acid genetic code. J. Am. Chem. Soc. 125, 935–939 (2003).

19. Francis, M. B. & Carrico, I. S. New frontiers in protein bioconjugation. Curr. Opin. Chem. Biol. 14, 771–773 (2010).

20. Netirojjanakul, C. et al. Synthetically modified Fc domains as building blocks for immunotherapy applications. Chem. Sci. 4, 266–272 (2013).

21. Mallikaratchy, P. et al. Aptamer directly evolved from live cells recognizes membrane bound immunoglobin heavy mu chain in Burkitt's lymphoma cells. Mol. Cell. Proteomics 6, 2230–2238 (2007).

22. Stephanopoulos, N., Tong, G. J., Hsiao, S. C. & Francis, M. B. Dual-surface modified virus capsids for targeted delivery of photodynamic agents to cancer cells. ACS Nano 4, 6014–6020 (2010).

23. Valegård, K., Liljas, L., Fridborg, K. & Unge, T. The three-dimensional structure of the bacterial virus MS2. Nature 345, 36–41 (1990).

24. Schnurr, M., Witte, C. & Schröder, L. Functionalized ^{129}Xe as a potential biosensor for membrane fluidity. Phys Chem Chem Phys 15 , 14178–14181 (2013).

25. Bai, Y., Wang, Y., Goulian, M., Driks, A. & Dmochowski, I. J. Bacterial spore detection and analysis using hyperpolarized ^{129}Xe chemical exchange saturation transfer (Hyper-CEST) NMR. Chem. Sci. 5, 3197 (2014).

26. Riggle, B. A., Wang, Y., and Dmochowski, I. J. A "Smart" ^{129}Xe NMR Biosensor for pH-Dependent Cell Labeling. J. Am. Chem. Soc. 137, 5542–8 (2015).

27. Finbloom, J. A., Slack, C. C., Bruns, C. J., Jeong, K., Wemmer, D. E., Pines, A., and Francis, M. B. Rotaxane-mediated suppression and activation of cucurbit[6]uril for molecular detection by ^{129}Xe hyper-CEST NMR. Chem. Commun. 52, 3119–22 (2016).

28. Wang, Y. & Dmochowski, I. J. Cucurbit[6]uril is an ultrasensitive ^{129}Xe NMR contrast agent. Chem. Commun. (Camb). 51, 8982–5 (2015).

29. Kupce, E., Boyd, J. & Campbell, I. D. Short Selective Pulses for Biochemical Applications. J. Magn. Reson. Ser. B 106, 300–303 (1995).

30. Shapiro, M. G. et al. Genetically encoded reporters for hyperpolarized xenon magnetic resonance imaging. Nat. Chem. 6, 629–634 (2014).

31. Kaiser, E., Colescott, R. L., Bossinger, C. D. & Cook, P. I. Color test for detection of free terminal amino groups in the solid-phase synthesis of peptides. Anal. Biochem. 34, 595–598 (1970).

32. Niellsen, O. & Buchardt, O. Facile synthesis of reagents containing a terminal Maleimido ligand linked to an active ester. Synthesis (Stuttg). 819–821

33. Farkas, M. E. et al. PET Imaging and Biodistribution of Chemically Modified Bacteriophage MS2. Mol. Pharm. 10, 69–76 (2013).

34. Netirojjanakul, C. et al. Synthetically modified Fc domains as building blocks for immunotherapy applications. Chem. Sci. 4, 266–272 (2013).